Lancaster University
Physics Department

PATET
OMNIBUS
VERITAS

Non-Hermitian Topological States in Photonic Systems

Simon Malzard

This thesis is submitted in partial fulfilment of the requirements for the degree of
Doctor of Philosophy
September 2018

Declaration

Except where stated otherwise, this thesis is a result of the author's original work and has not been submitted in substantially the same form for the award of a higher degree elsewhere. Other sources of information have been used, they have been acknowledged. This thesis documents work carried out between October 2014 and September 2018 at Lancaster University, UK, under the supervision of Prof. H. Schomerus and Dr. E. McCann funded by the **E**ngineering and **P**hysical **S**ciences **R**esearch **C**ouncil (EPSRC) of the United Kindgom.

Simon Malzard

September 2018

Abstract

In this thesis I explore non-Hermitian topological photonics with the aim of describing new phenomena which question our understanding of how far the current classification of topological states extends. This work invigorates the search for topological states in photonic systems with the hope of describing new mechanisms for controlling and increasing the number of physical systems in which robust light transport can be achieved. In coupled resonator optical waveguides, I demonstrate the formation of topological defect states in one dimensional systems and topological edge states in two dimensional systems, which only occur for a system with open boundaries. Since a non-Hermitian system displaying topological defect states with a trivial Hermitian limit has not been seen before, these results are both novel and paradigm breaking.

Topological mode selection is another mechanism unique to controlling topological states in non-Hermitian photonic system. I consider a non-linear extension to this notion for a complex wave equation describing lasing elements with saturable gain. I show that beyond the categorisation of topological stationary-states, which continue from the underlying linear system, new power-oscillating topological states form. These power-oscillations have not yet been seen in experiments but ongoing collaborations aim to see these solutions in the near future.

Acknowledgements

I would like to express my gratitude to Prof. H. Schomerus for providing many hours of stimulating discussion and mentorship, without which the successful conclusion of this thesis would not be possible. He directly inspired me to pursue a PhD in this area by making topological photonics an exciting topic.

I would also like to pay a special thanks to Dr Charles Poli for his mentorship and discussions which have helped develop my research and programming skills. I appreciate both the support and insightful discussion from the other members of the group, especially Dr Emiliano Cancellieri, Dr Marjan Famili, Ryan Hunt and Jake Arkinstall.

Finally, I would like to acknowledge Lancaster University Physics department for the provision of a Studentship.

Contents

1 Introduction **1**

1.1 Motivation 2

1.2 Thesis Structure 5

1.3 Topological States and Symmetries 6

1.3.1 Hermitian Symmetries 9

1.3.2 Example: SSH Model 13

1.4 Consequences of non-Hermicity 18

1.4.1 Two-level model and avoided crossings 18

1.4.2 Exceptional Points and $\mathcal{PT}$-symmetry 20

1.4.3 Time evolution, geometric phases and interchange of eigenstates 23

2 Coupled resonators optical waveguides **25**

2.1 Coupled Resonators 27

2.1.1 Defect states and wave matching 34

2.1.2 Phase Diagram 39

2.1.3 Finite-size effects 41
2.1.4 Testing robustness 44
2.2 Conclusion 48
3 Bulk and Edge Fermi Arcs in Coupled Resonator Arrays 51
3.1 2D array 53
3.1.1 Bulk Arcs 54
3.1.2 Interfaces and extending the wave matching 57
3.1.3 Phase diagram and edge states 61
3.1.4 Breaking $\mathcal{PT}$-symmetry 63
3.2 Conclusion 65
4 Nonlinear mode competition in topological laser arrays 67
4.1 Nonlinear topological laser arrays 70
4.1.1 Modelling laser arrays with saturable gain 70
4.1.2 Symmetries and solutions 73
4.2 Stability analysis: Theory 76
4.2.1 Stability analysis 80
4.2.2 Topological modes 83
4.3 Stability analysis: application 85
4.3.1 Beyond ideal conditions 87
4.3.2 Modified gain distribution 87

4.3.3 Modified mode volume 91

4.3.4 Robustness of operation conditions 93

4.3.5 Coupling disorder 93

4.3.6 Onsite disorder 96

4.3.7 Symmetry-breaking nonlinearities 96

4.4 Conclusions 100

5 Conclusions **103**

Bibliography **105**

List of Figures

1.1 Sketches of typical topological band structures for a gapped insulator, with edge states crossing the Fermi level in the gap (left panel) and energy level diagram of a gapped 1D superconductor with charge-conjugation symmetry. The left set of energy levels demonstrates the symmetric pairing of energy states around $E = 0$, the middle set shows a Majorana zero-mode pinned to the Fermi level whilst the right set shows that single energy states cannot be created without breaking charge-conjugation symmetry (as it is its own antiparticle, perturbing it away from $E = E_F$, it would not appear as a pair of symmetric levels like all other states). 9

1.2 Su-Schrieffer-Heeger model showing the different bulk phases of the chain. Red lattice sites are A sites, blue lattice sites are B sites and the orange lattice site indicates a defect. The unit cells for the bulk phases are given by the grey dimer. The upper panel contains the α phase, where the bulk is topologically trivial, the middle panel contains the β phases, where the bulk is topologically non-trivial. The bottom panel shows both phases brought together by a dimerisation defect, which is connected to either side by single bonds. 14

1.3 (a) Winding numbers for the SSH chain without a defect. Red and blue trajectories encompass the origin and hence are topologically non-trivial, whilst all other trajectories do not and are therefore trivial. Plotted for couplings $t_1 = 0, t_2 = 1.0$ (red), $t_1 = 0.5, t_2 = 1.0$ (blue), $t_1 = 1.0, t_2 = 1.0$ (green), $t_1 = 1.0, t_2 = 0.5$ (black) and $t_1 = 1.0, t_2 = 0.1$ (orange). (b) Numerical spectrum of the SSH chain with a defect for 16 dimers, plotted as a function of t_1, where $t_2 = 1.0$. The red line indicates a zero mode, which is topologically protected and an example of the wavefunction is given by that shown in figure (c) where $t_1 = 0.5, t_2 = 1$. For $t_1 > t_2$, the wavefunction is an extended state. 17

1.4 Sketches of different types of band touching points for two-level systems for no interaction $\alpha = \beta = 0$ (left), Hermitian interactions $\alpha = \beta \neq 0$, $\alpha, \beta \in \mathbb{R}$, resulting in an avoided crossing with gap of size $4\lambda|\alpha|$ (middle) and non-Hermitian interactions where $\alpha = -\beta$, displaying the square root branch points at $\pm\Delta_c$ (right), which join real eigenvalues (orange) to imaginary eigenvalues (purple). 20

2.1 a) Sketches of deformed coupled resonators and tight binding chain schematic with internal backscattering couplings (A and B) and inter-resonator coupling W which couples CW (CCW) modes of one resonator to CCW (CW) modes of adjacent resonators. b) Phase diagram of the bulk dispersion given by equation 2.13, where phase space is separated into regions of real gapped bands, imaginary gapped bands, 2 exceptional points and 4 exceptional points. c) corresponding dispersions of complementary coloured phase from b). d) Sketch of chain where the dotted line indicates where the defect occurs, resulting in the opposite resonator deformation and inversion of the backscattering couplings. 31

2.2 Phase diagram indicating the existence of defect states and their extended state (ES) precursors, bounded by the $\mathcal{PT}$ and $\mathcal{CPT}$-symmetry lines. The Hermitian line $H = H^\dagger$ is included to demonstrate that defect states only exist for open boundary conditions. . . 40

2.3 The central panel shows the trajectory of one of the four eigenvalues associated with the defect states from the upper right quadrant of the complex plane for the interval $1 < B < 4.5$, $A = W = 1$ (the other 3 quadrants are mirror images of the central panel). Panels labelled a)-h) give examples of the corresponding defect states and their precursors for eigenvalues marked by the black squares (following the trajectory anti-clockwise from the bottom) in the central panel. Each mode profile consists of two intensities $|a_n|^2$ of the CW component in the left half of the chain and the CCW component in the right half of the chain and $|b_n|^2$ of the CCW component in the left half of the chain and the CW component in the right half of the chain. Panels a)-h) contain parameters as follows: A=W=1, B= a) 1.5, b) 1.8, c) 1.85, d) 2.0, e) 2.5, f) 2.9, g) 3.2 and h) 3.5. . . 43

2.4 (Left panel) Divergences in the Petermann factor indicate spectral degeneracies in both the extended state phase and the two large broad peeks which indicate the $\mathcal{PT}$ and $\mathcal{CPT}$ phase transitions. (Right panel) Inverse participation ratio which grows large over the defect state phase. Both panels are produce for the same interval as that shown in figure 2.3, where the black markers are labelled in the same order as given in the caption. 44

2.5 Asymmetric chain: a) Example of a defect state for couplings $A = W$, $B = 2W$ in the left half and $A = 0.5W$, $B = 2.5W$ in the right half of the chain. The remaining 3 panels are given by the parameters $A = W$, $B = x$ on the left half of the chain and $A = 0.5W$, $B = 0.5W + x$ on the right half: b) Trajectories of the eigenvalues associated with the defect states and their predecessors. c) Petermann factor of the defect states and predecessors. d) Inverse participation ratio of the defect states and predecessors. 45

2.6 The same as given in figure 2.5, except now the backscattering amplitudes A and B have been perturbed by drawing from the uniform distribution $y \in [-0.1W, 0.1W]$ for three different disorder realisations. Panel a) shows an example of a defect state for one of the disorder realisations for the same parameters give in panel a) of figure 2.5 plus the additional perturbation. 47

3.1 Bulk Fermi arcs in a two dimensional array of evanescently coupled non-hermitian resonators. (a) Each resonator supports a clockwise (CW) and a counter-clockwise (CCW) internal mode that are coupled by asymmetric backscattering amplitudes A and B, as obtained, e.g., from a small non-spherical deformation of open dielectric resonators. The resonators are placed on a square lattice and are coupled evanescently with coupling coefficients W_x and W_y that convert CW waves into CCW waves. This coupling configuration introduces a chiral symmetry into this non-hermitian system.(b-d) Real part $\mathrm{Re}\,\Omega$ of the bulk dispersion for $B = -2.5 + 0.2i$, $W_x = 1.0 + 0.1i$, $W_y = 1.0 + 0.5i$, and the three values $A = 1.5 + 0.1i$ (b), $A = 1.5 + 0.2i$ (c) and $A = 1.5 + 0.3i$ (d). In each case, the dispersion consists of two sheets Ω_+ (yellow surface) and $\Omega_- = -\Omega_+$ (blue surface) that are related by the chiral symmetry. The white lines indicate Fermi arcs and lines with $\mathrm{Re}\,\Omega = 0$, corresponding to intersections of the two sheets. The arcs terminate at exceptional points (EPs), which are the non-hermitian counterparts of Weyl points in topological insulators. In (b), four EPs are connected by two arcs. In (d), the EPs are reconnected by two arcs with a different topology, while a closed Fermi line is also present. Panel (c) shows the reconnection point between these two scenarios, which is mediated by two smaller closed Fermi lines. Bulk dispersions are also shown for $B = -1.5 - 0.2i, A = 1.5 + 0.2i, W_x = 1.0 - 0.5i$ and $W_y = 1.0 + 0.5i$ for panel e) and $B = -2.5 + 0.2i, A = 1.5 + 0.2i, W_x = 1.0 - 0.3i$ and $W_y = 1.0 + 0.3i$ for panel f). Balancing the gain and loss of W_x and W_y creates additional exceptional points for the Fermi-arcs to connect between. 55

3.2 (a) Real and (b) imaginary parts of the bulk dispersion for $A = 1.0$, $B = -1.0$ and $W_x = W_y = 1$, representing the $\mathcal{PT}$-symmetric case (symmetry class BDI) where the band structure displays purely real and imaginary branches, and the exceptional points degenerate into lines. 56

3.3 Edge-state arcs in an array with an interface joining resonator arrays with opposite backscattering. (a) Horizontal slice through the array, where the dotted line indicates the interface between resonators with backscattering amplitudes A and B as in figure 3.1 (blue resonators to the left), and resonators where the values of these backscattering amplitudes are interchanged (green resonators to the right). (b) Density plot of the intensity of a representative edge state in a finite square array of 40×40 resonators, with $A = -B = W_x = W_y$. (c) Quasi-one dimensional band structure in the infinite version of this array, where k_y is a good quantum number. In this representation, the bulk bands form sheets, which here lie in the real and imaginary plane as all parameters are real ($\mathcal{PT}$-symmetric symmetry class BDI, see figure 3.2). The black curves are the edge-state arcs, which connect the different sheets. . 58

3.4 (a) Traces of the edge-state arcs in the real section of their effective parameter space $(\mathcal{A},\mathcal{B})$ [defined in Eq. (3.11)]. The traces are horizontal lines of length $4W_y/W_x$, which are centred at $\mathcal{A} = (A+B)/2W_x$, $\mathcal{B} = (A-B)/2W_x$. The solid and dashed curves denote the termination conditions at the real and imaginary branches of the bulk bands, where the edge states (green region) turn into extended scattering states (red) or into non-normalizable, unphysical states (blue). The three representative traces correspond to the quasi-one-dimensional band structures shown in (b-d), where the edge-state arcs are indicated in green, while their scattering predecessors are given in red and unphysical states in blue. In (b), $A/W_x = 0.55$, $B/W_x = -0.55$, $W_y/W_x = 1.175$, for which the trace crosses both termination lines and the arcs connect the real and imaginary branches of the bulk bands. In (c), $A/W_x = -0.9$, $B/W_x = 0.9$, $W_y/W_x = 1$, for which the trace only reaches the real termination line so that the arcs loop back to the real branches. In (d), $A/W_x = -2.0$, $B/W_x = 2.0$, $W_y/W_x = 1$, for which the trace remains confined in the edge-state region so that the arc are free-standing. 62

3.5 (a) Edge-state arcs for complex backscattering amplitudes $A/W_x = 0.55{+}0.02i$, $B/W_x = -0.55{+}0.02i$ and $W_y = 1.175$ [close to the real values in figure 4.13(b)]. All arcs still terminate on the bulk bands, which now no longer are real or imaginary. (b-d) Propagation factors $|\lambda_l|$, $1/|\lambda_l|$ of potential edge states as determined by equation 3.14. In (b), $A = -B = 0.55/W_x$, $W_y/W_x = 1.175$, corresponding to the real values of figure 4.13 panel (b). In (c,d), the parameters take the complex values given above. For complex parameters the region of scattering states is replaced by regions of physical and unphysical states. Furthermore, the termination points of different arcs now appear at separate values of k_y, as shown in detail in panels (d) and (e) which zoom into the termination region at the formerly purely imaginary and real branches of the bulk dispersion, respectively. 64

4.1 Topological mode selection in laser arrays consisting of single-mode resonators grouped in dimers (enumerated by n). The intra-dimer couplings κ and inter-dimer couplings κ' are chosen to produce interfaces between regions of topologically different band structures. (a) In the Su-Schrieffer-Heeger (SSH) model, the alternating couplings define a phase α ($\kappa > \kappa'$) and a phase β ($\kappa < \kappa'$). The displayed defect state arises from two consecutive weak couplings, forming an interface between the two phases. (b) The defect region can be extended, leading to a variant where the phases α and β function as selective mirrors that confine a defect state with a larger mode volume. In both cases, the resulting defect states have preferential weight on the A sublattice (red) and can be selected by distributed gain and loss. As illustrated in the right panels, in the linear regime the defect state acquires the effective gain G_A from the A sublattice, while the other modes acquire the average gain $\bar{G}$ in the system ($G_A = \bar{G} + 0.1,\ \kappa, \kappa' = 1, 0.7$). We demonstrate that this mode selection mechanism extends to the nonlinear conditions at the working point of a laser, where it stabilises robust zero modes and also enables alternative topological operation regimes with power oscillations. 70

4.2 Topological lasing regimes for the SSH array of figure 4.1(a) pumped on the A sublattice (finite gain g_A at fixed $g_B = 0$, with amplitudes scaled such that $S_A = S_B = 1$) under conditions that preserve the symmetries in the linear case ($\omega_{s,n} = \omega_{AB}$, $\alpha_s = 0$), demonstrating operation in topological states over the whole parameter range. (a) Phase diagram of stable quasistationary operation regimes depending on the gain g_A and background losses $\gamma_A = \gamma_B \equiv \gamma_{AB}$, where lasing requires $g_A > \gamma_{AB}$. Over the whole grey region labelled Z, the system establishes stationary lasing in a topological zero mode. In the orange region, this is replaced by operation in a twisted topological mode T_1 displaying power oscillations. In the pink region an additional twisted state T_2 exists, whose selection then depends on the initial conditions. The remaining panels analyse the lasing characteristics for varying gain g_A along the line $\gamma_{AB} = 0.1$ (blue arrow in the phase diagram). (b) Sublattice-resolved intensities I_A (red) and I_B (blue), including shaded intensity ranges for the power oscillations of T_1 and dashed lines indicating the corresponding ranges for T_2. (c) Amplitude oscillation period T (equalling twice the period of power oscillations for twisted states, see Fig. 4.3). (d) Correlation function $\tilde{C}(t)$ at $t = 0, T/2$, where $\tilde{C}(T/2) = I_{\max}$ reveals the topological nature of the states (see text). As illustrated for the examples in Fig. 4.3, all states inherit the intensity profile of the linear defect mode from Fig. 4.1(a). 73

4.3 Topological wave features of representative lasing states at parameters indicated by blue dots in figure 4.2 ($g_A = 0.2$ for Z, $g_A = 0.5$ for T_1 and T_2). (a) Intensity distributions over the array, shown both as spikes and as disks with area proportional to intensity, substantiating the relation of these stabilised states to the linear defect state from figure 4.1(a). (b,c) Time-dependence of the sublattice-resolved intensities $I_A(t)$ and $I_B(t)$ (red and blue) and of the correlation functions $C(t)$, $\tilde{C}(t)$ (orange and brown). The alternating correlations $\tilde{C}(t + T/2) = C(t)$ verify the twisted nature of the states T_1 and T_2, while $C(t) = \tilde{C}(t) = \text{const}$ verifies that the state Z is a topological zero mode. 77

4.4 Stability excitation spectra of the representative states illustrated in figure 4.3. For the stationary state Z this represents the Bogoliubov spectrum ω, which separates into excitations $\omega_\pm$ that preserve or break the symmetry. This separation further verifies its zero-mode character (see text), while $\operatorname{Im}\omega < 0$ [apart from the U(1) Goldstone mode at $\omega = 0$] affirms that the state is stable. For the periodically oscillating states T_1 and T_2, this represents the Bogoliubov-Floquet stability spectrum λ (top, green) and the spectrum λ' of the half-step propagator (bottom, red). Both spectra are confined by the unit circle in the complex plane, demonstrating that these states are stable. The symmetry-protected excitations pinned to $\lambda' = \pm 1$ further verify the twisted nature of these states. 78

4.5 Topological phase transition between the zero-mode regime Z and the twisted mode T$_1$, at $g_A = 0.291$ along the line $\gamma_{AB} = 0.1$ (see figure 4.2). At the transition two Bogoliubov excitations $\omega_{-,\star} = 2\pi/T$ and $\tilde{\omega}_{-,\star} = -\omega_{-,\star}$ are marginally stable, where T is the period of the emerging twisted mode T$_1$. Along with the U(1) Goldstone mode, they all map onto Floquet-Bogoliubov excitations $\lambda = 1$ for this emerging mode. Away from the transition, these excitations split into two degenerate excitations $\lambda_0 = \lambda_t = 1$ associated with the U(1) and time translation freedoms, and a decaying excitation λ_f related to the amplitude stabilisation of the power oscillations. (Note that at the transition another pair of excitations is almost unstable, which will give rise to the twisted mode T$_2$.) 86

4.6 Role of reduced gain imbalance, obtained under the same conditions as in figures 4.2-4.4, but with finite gain $g_B = 0.1$ on the B sublattice. For $\gamma_{AB} < g_B$ the parameter space now also contains a region (dark orange) supporting additional pairs of symmetry-breaking modes P. As illustrated for the marked example, these modes have substantial weight on the B sublattice, while their independent correlation functions $C(t)$ and $\tilde{C}(t)$ show that they spontaneously break the symmetry. For such modes the Bogoliubov-Floquet spectrum contains many eigenvalues close to the unit circle, indicating their high sensitivity under parameter changes. As shown in the top panels for the cross-section now placed at $\gamma_{AB} = 0.2$, the remaining parameter space supports the same robust topological lasing modes as observed for $g_B = 0$ (twisted modes T$_1$ and T$_2$ and stationary topological modes Z, as illustrated by the marked examples). 88

4.7 Role of increased mode volume, obtained for the laser array with topological mirrors illustrated in figure 4.1(b). Here I consider ideal lasing conditions with variable gain g_A and background loss $\gamma_A = \gamma_B \equiv \gamma_{AB}$, at vanishing gain $g_B = 0$ on the B sublattice. The representation of the data is the same as in figure 4.6. The resulting operation regimes closely resemble those of the SSH laser array under corresponding conditions (see figures 4.2-4.4), with a phase of stationary zero-mode lasing supplemented by phases with one or two twisted modes displaying power oscillations. The intensities of these modes have increased, which reflects their larger mode volume, as illustrated in more detail for the three examples marked Z, T_1 and T_2. 89

4.8 Interplay of mode volume and gain imbalance. Same as figure 4.7, but for finite gain $g_B = 0.1$ on the B sublattice, and the cross-section through parameter space shifted to $\gamma_{AB} = 0.2$. Compared to the corresponding conditions in the SSH laser array (figure 4.6), a larger range of parameters now supports a multitude of additional states. At the representative point marked P, this includes a pair of symmetry-breaking oscillating states, whose power oscillations are modulated. The features of these symmetry-breaking states are not very robust, as indicated by their Bogoliubov-Floquet stability spectra, which display many slowly decaying excitations. These modifications are restricted to the range of parameters that previously displayed the twisted states T_1 and T_2 (now only seen for large enough gain), but does not affect the operation in the zero-mode Z. Along the cross-section $\gamma_{AB} = 0.2$, we enter only briefly enter this modified regime, in a region where there is only one extra, twisted, state, which destabilises the zero mode. 90

4.9 Disorder-driven phase transitions for the SSH laser array as in figures 4.2-4.4, but with fixed $\gamma_{AB} = 0.1$ and variable strength W of coupling disorder. Each panel corresponds to one randomly selected disorder configuration, with perturbed couplings $\kappa_n = \bar{\kappa}(1 + W r_n)$, $\kappa'_n = \bar{\kappa}'(1 + W r'_n)$ obtained from a fixed realisations of uniformly distributed random numbers $r_n, r'_n \in [-1/2, 1/2]$. Zero-mode lasing persists at all disorder strengths. Twisted states remain robust for weak to moderate disorder, while phase transitions to other operating regimes can appear when the disorder is very strong. 94

4.10 Effect of strong onsite disorder in analogy to figure 4.11, for the disorder realisation of figure 4.12(a) at $W = 0.5$. Even though the disorder breaks the symmetry, all states can be traced back to their disorder-free predecessors. The stationary lasing regime originating from the zero mode Z is barely affected. The mode originating from T_1 is pushed into a smaller part of parameter space, so that the instability phase transition now involves the modes originating from Z and T_2. The power-oscillations of the originally twisted states are modulated to clearly display the period T of underlying amplitude oscillations. The mode profiles of all states are only slightly distorted. 95

4.11 Effect of strong coupling disorder for the SSH laser array as in figures. 4.2-4.4, with the disorder configuration of figure 4.9(a) at $W = 0.5$. For this realisation the regime of zero-mode lasing is slightly reduced in favour of the power-oscillating twisted mode T_1, while the twisted state T_2 has been replaced by another twisted mode T_2', which appears in a disorder-strength-dependent phase transition. As gain is further increased, T_1 undergoes a period-doubling bifurcation to a symmetry-breaking pair of states P_1, while T_2' is replaced by an aperiodic pair P_2' (for which the Floquet-Bogoliubov stability spectrum is not defined). All modes display visible distortions of their mode profile, and the symmetry-breaking pairs display noticeable amplitude on the B sublattice. 97

4.12 Robustness against onsite disorder in analogy to figure 4.9, but for randomly selected disorder configurations with perturbed bare frequencies $\omega_{A,n} = \omega_{AB} + Wr_n$, $\omega_{B,n} = \omega_{AB} + Wr_n'$, $r_n, r_n' \in [-1/2, 1/2]$. While this type of disorder breaks the symmetries, the states can typically be tracked to large values of disorder. The mode originating from the zero mode Z persists at all disorder strengths, and at weak to moderate disorder extends into regions of larger gain. This happens at the expense of the originally twisted modes, which in panel the configuration of (c) are replaced by new power-oscillating modes X_1, X_2 when the disorder becomes strong. 98

4.13 Effect of nonlinear symmetry breaking on the modes of the SSH laser array shown in figurs 4.2-4.4, obtained by setting the linewidth-enhancement factor to $\alpha_A = \alpha_B = 0.5$. Most properties of the states are only slightly modified. The twisted correlation function $\tilde{C}(T/2)$ are slightly smaller than $I_{\max}$, while small independent modulations appear in the time-dependence of $C(t)$, $\tilde{C}(t)$. For the state originating from T_2, this results in noticeable modulations of the power oscillations, whose period is doubled. There are also noticeable changes in the stability spectra (green), which can no longer be deconstructed as in the case of exact symmetry. 99

4.14 Effect of staggered nonlinear symmetry breaking on the modes of the SSH laser array shown in figures 4.2-4.4, obtained by setting the linewidth-enhancement factor to $\alpha_A = -\alpha_B = 0.2$ so that the non-hermitian charge-conjugation symmetry is already broken in the linear regime. As in figure 4.13, most properties of the states are only slightly modified. 100

Chapter 1

Introduction

UNESCO designated 2015 as the 'International Year of Light and Light Based Technologies' in recognition of how important controlling light has become in our everyday lives. Physical Review highlighted some of the most important topics to this endeavour [1], which modern society strongly relies on to meet the ever increasing demands of high speed optical communications, data processing, integrated optical circuits and data storage.

Some of the key highlighted topics in the aforementioned celebration of past achievements include photonic crystals which make up optical fibres [2], squeezed light which is noise-free [3], long lived light storage [4], molecular imaging [5], and high-intensity photonic entanglement sources [6].

In this thesis I will bring together two concepts which have been at the forefront of optical innovation for the last two decades and explore the combination in a new light. The first concept is topological states of matter, where states located at the interface between materials (or material and vacuum boundaries) of different topological genus (which I will discuss in more detail in the next section) remain persistent and robust to disorder provided that certain symmetries remain preserved. These states are accompanied by insulating bulk phases. The schematic given in the left panel of figure 1.1 is a typical realisation of conducting edge states plotted on top of gapped bulk bands.

The second concept is non-Hermicity, which can relax the constraint of a fully real spectrum or the conservation of particle number. Non-Hermitian Hamiltonians describe open-systems where energy is dissipated to the environment (referred to as losses), while in the case of systems which lase, this can describe gain-amplification. Relaxing these constraints results in decaying normal modes, described by complex frequencies with finite lifetimes and is often associated with electron-electron or electron-phonon interactions [7, 8], as well as leakage and absorption.

1.1 Motivation

Systems exhibiting non-trivial band topology attract intense attention owing to phenomena such as chiral edge and surface states supported by boundaries between topologically distinct gapped phases. While the initial focus was on electronic or superconducting systems, the excitement quickly extended to other areas of quantum and classical wave phenomena, which often display very different constraints compared to fermionic systems, such as the non conservation of particle number.

Haldane and Raghu observed the universal nature of topological band theory when they realised that topological band structures are a property of waves inside a periodic medium [9]. In direct analogy with chiral edge states flowing along the surface of a quantum Hall bar in the Integer quantum Hall effect (IQHE), they postulated a ‘one-wave waveguide’ where unidirectional photonic modes had complete suppression of quasiparticle backscattering at the surface of the waveguide, including at bends or imperfections [10]. The unwanted feedback and loss of signal generated by backscattering in normal waveguides is mitigated by this design as the transmission along the surface of the waveguide is no longer hindered by fabrication imperfections. The modes of this one-way waveguide, occurring at microwave frequencies within the photonic band gap, have been experimentally verified in two-dimensional arrays of gyromagnetic ferrite rods which break time-reversal symmetry [11] and in honeycomb photonic crystals [12, 13].

Beyond the IQHE, experiments involving square lattices of coupled resonators introduce pseudo-spin internal degrees of freedom through counter propagating internal modes which alleviate the necessity for time-reversal symmetry breaking mechanisms. The pseudo-spins are decoupled by scatters in such a way that leads to an effective magnetic field with opposite signs for each pseudo-spin. The net result is an analogous description to the spin quantum hall effect [14], which by the same mechanism has also been achieved in ring resonators [15].

Effective magnetic fields can also be achieved in systems by harmonically modulating the coupling constants between lattices sites. These temporally driven periodic systems are then governed by floquet theory, where the symmetry of discrete time translations are in analogy with crystal momentum. Since the eigenstates are periodic in time, their phases introduce an effective gauge field which can be engineered into a form which gives rise to chiral edge states [16, 17]. With the expanse of a number of techniques, laser written waveguides provide another degree of freedom involving time dynamics. Instead of time periodically driven systems, modes are driven along helical structures with a propagation direction (z) which display chiral edge states in the (x, y) plane [18].

Whilst all of these examples of topological photonic systems are bosonic in nature, the focus has been on achieving analogous physics to fermionic systems. As mentioned, one major difference between these systems is that photons typically radiate and are therefore not conserved. Such non-conservation is described by non-Hermitian Hamiltonians with gain and loss. In general, non-Hermitian Hamiltonians have played an increasingly interesting role in recent years where several mechanism have been reported to induce topological phenomena. These are based on non-hermitian symmetries such as time-reversal symmetries ($\mathcal{PT}$) or combinations with chiral symmetry ($\mathcal{X}$) or charge-conjugation symmetry ($\mathcal{C} = \mathcal{XT}$).

Another main motivation compared to Hermitian systems is to obtain topological states with distinct life times, as encoded in the imaginary part of the energy spectrum.

In many cases, the models are based on topological hermitian counterparts, such as the well studied Su-Schrieffer-Heeger (SSH) model [19], where dissipation can yield quantised displacements of decay and survival processes [20, 21], while the introduction of gain and loss yields a topological mechanism of zero-mode selection based on a non-Hermitian $\mathcal{C}$ [22–26] or $\mathcal{PT}$ [27] symmetry. In these and other examples [28, 29] derived from topological Hermitian systems, the topologically protected states still obey a bulk-boundary correspondence [30] and their robust properties are directly inherited from the Hermitian limit.

However, this is not always the case. Protected edge and interface states can also arise via exceptional points, even when the Hermitian limit is topologically trivial [31–34]. This mechanism equips a system with robust spatially localised states that display distinct life times. Furthermore, non-Hermitian effects can fundamentally change the properties of edge states of a hermitian origin, which for instance can bifurcate at exceptional points to display additional branches with $\mathcal{PT}$-symmetry [35]. These observations highlight the role that exceptional points and their topological charges play in distinguishing conventional topological states with adopted non-Hermitian properties from genuinely non-Hermitian symmetry-protected states that do not have a Hermitian counterpart [30, 36], and for classifying non-Hermitian topological systems in general [37].

Recently, the question of whether the notions of non-Hermitian topological systems from passive systems could be extended to include non-linear systems with active elements has gained traction. Weak non-linearities arise naturally when one considers systems which are pumped externally and saturate such as lasers or from the intrinsic properties of the system such as for polaritons where photons are strongly coupled to an electric-dipole. Initial experiment in lasing systems have held much promise, where topological lasing has been reported in photonic crystal cavities [38, 39], edge modes in photonic crystals [40] and edge modes in topological insulators [41]. The question then becomes how best to utilise gain and loss.

Distributed gain and loss has been employed to achieve $\mathcal{PT}$-symmetry in lasers [42–45], which exploit a spectral phase transition between conventional modes that then acquire different weights on lossy and amplified regions. One proposed method goes a step further, to selectively enhance topologically protected modes by adding a staggered gain and loss profile to the well known SSH model [22]. Since the zero-mode of the SSH model is only localised to one of the two sublattices, the zero-mode can be amplified with respect to the other modes of the system enhancing the lifetime of the already spectrally isolated mode. Since these models involve only linear gain and loss and with the appearance of experiments built from these model [25, 26, 46], there is a clear need to see if topological mode selection still occurs in models containing non-linear gain and loss.

1.2 Thesis Structure

This thesis introduces two natural extensions of the paradigm of topological states discussed in the previous section. Both of these sets contain surprising new phenomena which are paradigm breaking and have no known analogue in other settings. The first set, which will be discussed in chapters 2 and 3, demonstrate the emergence of topological defect states in complex open wave systems with a topologically trivial hermitian limit. These intriguing results have been shown to have different consequences in one and two dimensions, so I shall therefore discuss the general model of how to realise topological defect states in the context of one dimensional chains of openly coupled resonator waveguides in chapter 2. I will also demonstrate the robustness of theses states to disorder. Extending the basis of this work further, in chapter 3 I will consider a two dimensional array of coupled resonators and describe the formation of bulk arcs from the dispersion relation. Using the formulation of topological defect states in chapter 2 I will also show that complex frequency edge states can form in these arrays, which connect the bulk real frequency bands to the bulk imaginary frequency bands.

In chapter 4, I will discuss the second set of new phenomena encountered in non-Hermitian, non-linear wave systems. I demonstrate that for the well established topological modes of the Su-Schrieffer-Heeger model, topological mode selection persists and acquires a new twist when applied to non-linear wave equations with loss and saturable gain. I analyse the topological modes which display saturation after an onset of lasing. These modes include a set of time-dependent and symmetry connected solutions which have no analogue in the linear system. By exploiting the underlying symmetries of this model I will describe how both the linear solutions and these new power-oscillating solutions are stable and topologically protected by examining the excitation spectrum with specific attention to phase transitions. I will also show the operational regimes of all the topological solutions found from this model.

In the remainder of this chapter, I will introduce some general notions that serve as the background to these investigations.

1.3 Topological States and Symmetries

One of the most remarkable results in condensed matter physics over the last decade is the concept and realisation of topological states of matter and the promise of finding long-lived states immune to decoherence, a key criterion for quantum computation [47]. Topological states are protected states provided that the corresponding Hamiltonian cannot be smoothly deformed (adiabatically) to remove the bulk band gap between the highest occupied band and the lowest empty band. Open and closing a gap therefore represents a phase transition. Since the study of topological spaces concerns global properties that cannot be removed or destroyed by smooth deformations, the same idea can be expressed with respect to band theory.

Topological spaces can be explained using the classic example of the torus (T^2) and sphere (S^2). Smooth deformations cannot destroy or create the hole (the global property) which appears in the center of the torus. Hence these two objects are topologically distinct, each has it's own *genus*, an index corresponding to the number of holes, which is also called the topological invariant.

The first topologically non-trivial electronic state was discovered in 1980 [48], in the context of the Integer Quantum Hall Effect (IQHE). Electrons confined to two dimensions are placed in a strong magnetic field, where in the insulating bulk of the material they perform quantised circular orbits. At the surface of the material metallic surface states carry a quantised Hall conductance along the surface. A mapping of the crystal momentum $\mathbf{k}$, which is defined on a torus, to the Bloch Hamiltonian $H(\mathbf{k})$ demonstrates an equivalence between the topological spaces and the 2D band structure of the Bloch Hamiltonian. The topological invariant for such systems is the geometric phase known as the Berry phase, a phase which is accumulated when Bloch states $|u_m(\mathbf{k})\rangle$ of the bulk Hamiltonian are taken in closed loops around the Brillouin zone which enclose the special degeneracy points where the gap would close. In the case of the Bloch Hamiltonian for the IQHE, the topological invariant is a Chern invariant $Q \in \mathbb{Z}$.

The Chern invariant occurs in integer multiples of 2π. This integer gives the net number of times a surface state may cross the Fermi Energy (where counting the crossings, $+1$ indicates a crossing with positive group velocity ($\frac{dE}{dK}$) and -1 indicates a crossing with negative group velocity). This net integer therefore counts the number of edge states at each edge. Hence the invariant of the bulk corresponds to the properties at the edge.

Since 1980 the IQHE has become just one of many examples where emergent protected phenomena exists. In the realm of single-particle physics, the IQHE is accompanied by other examples such as the spin-IQHE, topological insulators, Chern insulators and topological superconductors, whilst many-body physics hosts the fractional quantum Hall effect.

A powerful notion which connects all of these cases is the principle of bulk-boundary correspondence. If the gap in the bulk of the material remains open, smooth deformations which prohibit the closing of the gap also protect the presence of the states at the edge, provided that the topological invariant of the material under considerations differs from that which lies beyond the edge. Whilst all Hermitian topological materials obey this principle of bulk-boundary correspondence, they do not all have the same types of invariant or have the same types of topological surface states. By invoking different combinations of the three fundamental Hermitian symmetries discussed in the next section, Altland and Zirnbauer [49] proposed a table of 10 classes which exhaust the combinations of the three symmetries in 0d.

This classification is called the 'Ten-fold way' and has its roots in random matrix theory. The full classification also considers the number of spatial dimensions, leading to the so-called periodic table of topological insulators and superconductors [50, 51]. The classification also includes trivial combinations where there are no topological states and hence no invariant is present. The non-trivial classifications have invariants which come in three forms, they can be integers ($\mathbb{Z}$), even integers ($2\mathbb{Z}$) or binary ($\mathbb{Z}_2$). In the next section we will see some brief examples of how each of these come about.

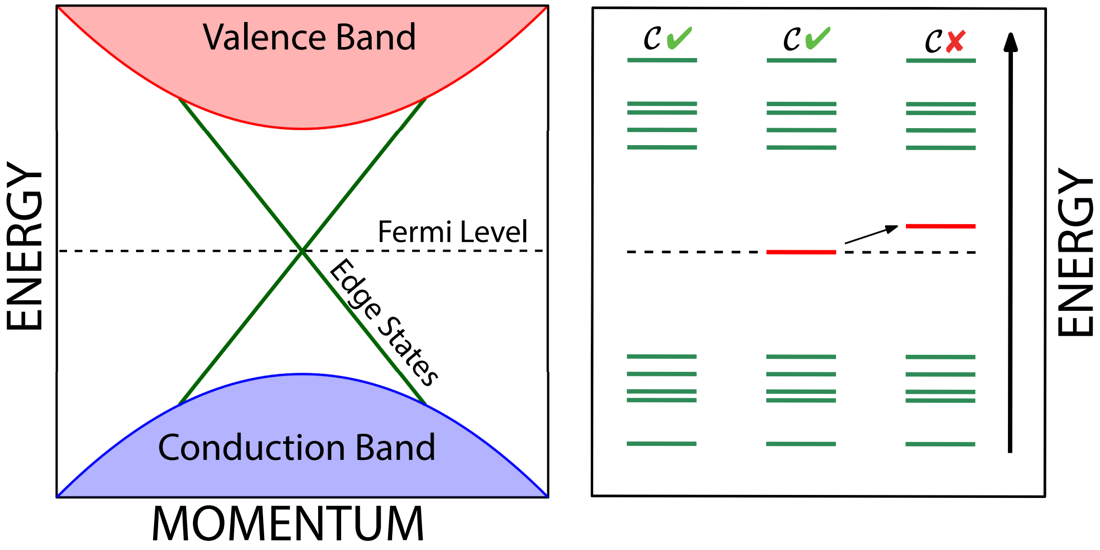

Figure 1.1: Sketches of typical topological band structures for a gapped insulator, with edge states crossing the Fermi level in the gap (left panel) and energy level diagram of a gapped 1D superconductor with charge-conjugation symmetry. The left set of energy levels demonstrates the symmetric pairing of energy states around $E = 0$, the middle set shows a Majorana zero-mode pinned to the Fermi level whilst the right set shows that single energy states cannot be created without breaking charge-conjugation symmetry (as it is its own antiparticle, perturbing it away from $E = E_F$, it would not appear as a pair of symmetric levels like all other states).

1.3.1 Hermitian Symmetries

The three symmetries which determine the 10 Altand-Zirnbauer classes are made up of two anti-unitary operators, time reversal ($\mathcal{T}$) and charge conjugation ($\mathcal{C}$), which can both either square to 1 or -1 and one unitary operator belonging to chiral (χ) symmetry which always squares to 1. These three symmetries impose conditions on the spectra of each class. Since chapter 4 of this thesis is concerned with zero-modes I will end this section by focusing on the simplest $1D$ with topological states as an example.

The 10 classes are presented in table 1.1 and are listed as follows: Firstly counting classes where only a single symmetry is present, since both time reversal symmetry and charge-conjugation symmetry can square to either ± 1, this constitutes four distinct classes. These classes are labelled AI and AII when time-reversal symmetry only is present, with $\mathcal{T}^2 = 1, -1$ respectively. Classes D and C appear when

	Cartan Class									
Symmetry	A	AIII	AI	BDI	D	DIII	AII	CII	C	CI
$\mathcal{T}$	0	0	1	1	0	-1	-1	-1	0	1
$\mathcal{C}$	0	0	0	1	1	1	0	-1	-1	-1
χ	0	1	0	1	0	1	0	1	0	1
Dimensions	Invariants ($\mathcal{Q}$)									
1	0	$\mathbb{Z}$	0	$\mathbb{Z}$	$\mathbb{Z}_2$	$\mathbb{Z}_2$	0	$\mathbb{Z}$	0	0
2	$\mathbb{Z}$	0	0	0	$\mathbb{Z}$	$\mathbb{Z}_2$	$\mathbb{Z}_2$	0	$\mathbb{Z}$	0
3	0	$\mathbb{Z}$	0	0	0	$\mathbb{Z}$	$\mathbb{Z}_2$	$\mathbb{Z}_2$	0	$\mathbb{Z}$

Table 1.1: Periodic table of the ten symmetry classes given according to their Cartan labels. Each class is composed of the presence of absence of time-reversal symmetry $\mathcal{T}$, charge-conjugation symmetry $\mathcal{C}$ or chiral symmetry $\chi = \mathcal{T}\mathcal{C}$. If a symmetry is absent the entry for the corresponding class is denoted by a 0, if it is present it is denoted by ±1, where ±1 corresponds to the value of the relevant symmetry operator squared. The invariants $\mathcal{Q}$ are given as a function of both class and number of dimension(s) for the first 3 dimensions.

charge-conjugation symmetry only is present, again with $\mathcal{C}^2 = 1, -1$ respectively. The final single symmetry class is given by class AIII, where only chiral symmetry is present. Since χ squares to 1, chiral symmetry on its own only forms one class. A further four classes denoted as class BDI, DIII, CII and CI occur when both time-reversal and charge-conjugation symmetry are present covering all of the possible combinations of $\mathcal{T}^2, \mathcal{C}^2 = \pm 1$ as presented in 1.1. Additionally when both time-reversal and charge-conjugation symmetries are present, chiral symmetry is also by default present as $\chi = \mathcal{C}\mathcal{T}$. Chiral symmetry then still satisfies $\chi^2 = 1$. Finally the last remaining class, class A, contains no symmetries.

If time-reversal symmetry is present it commutes with the Hamiltonian, $\mathcal{T}H\mathcal{T}^{-1} = H$. If $\mathcal{T}^2 = 1$, then there is a basis where time reversal symmetry can be given by complex conjugation ($\mathcal{T} = K$). This occurs for the case of spin-less particles and combined with Hermicity this imposes that H contains only real elements as $H_{lm} = H^*_{ml}$. Without any other symmetries being present this is referred to as class AI. This symmetry occurs in the models in chapters 2 and 3.

If $T^2 = -1$ then there is a basis where T can be written as $T = \Omega K$, where $\Omega = i\sigma_y \otimes \mathbb{1}_m$, σ_i is the 2×2 i'th Pauli matrix and $\mathbb{1}_m$ is the m dimensional identity matrix, where m corresponds to the number of channels in a system. This structure can arise for the case of spin-1/2 particles where σ_y represents a spin-degree of freedom. The spin degree of freedom means that T has even dimensions of $2m$, where the basis can be arranged in the identical time-reversed pairs of the same energy, i.e. $|\psi\rangle = T|\bar{\psi}\rangle$. This results in a doubly degenerate spectrum, which is known as Kramer's degeneracy. If no other symmetries are present this corresponds to class AII.

Charge-conjugation (also know as particle-hole symmetry) is the other anti-unitary symmetry in the classification. It anti-commutes with the Hamiltonian, $\mathcal{C}H\mathcal{C}^{-1} = -H$, which causes states at positive energy to be paired with states at negative energy. This symmetry means that energy levels must therefore approach and cross the Fermi level in pairs. The most prominent group of systems this symmetry appears in is the group of superconductors described by the Bologliubov-de Gennes (BdG) Hamiltonian, a mean-field description of the quasiparticle excitations.

The BdG Hamiltonian can be expressed as

$$H_{BdG} = \begin{pmatrix} H_0 - E_F & \Delta_0 \\ \Delta_0^* & E_F - H_0^* \end{pmatrix}, \tag{1.1}$$

where E_F is the Fermi energy and H_0 is the Hamiltonian when the s-wave superconductivity pairing term Δ is set to zero. Here I have suppressed the spin degree of freedom to highlight the charge conjugation symmetry. $H_0 - E_F$ represents particle-like excitations above the Fermi energy, where as $E_F - H_0^*$ represents hole-like excitations below the Fermi energy. In this case $\mathcal{C}^2 = 1$ and $C = \tau_x K$, where τ is the Pauli matrix operating on the particle-hole degree of freedom.

A single fermionic state in this description is associated with a pair of energy level

E_+ and E_-, where $E_+ = -E_-$. The corresponding quasiparticle operators at these two energies are joined by the relation $\xi_{E_+} = \xi^\dagger_{E_-}$ and hence a special case exists when $E_+ = E_- = 0$, as these operators now define a charge neutral particle which is its own antiparticle, called the Majorana zero-mode. This is an example of class DIII [52].

Spin degeneracy needs to be broken in order to realise an unpaired Majorana mode. This can be achieved in two ways, either by considering a superconducting coupling associated with a topological superconductor which is of ‘p-wave’ type, for a single spin-band this corresponds to the spin-triplet coupling term $\Delta = \Delta_0(p_x - ip_y)$. Or by considering a conventional ‘s-wave’ ($\Delta = \Delta_0$) superconductor in conjunction with the strong spin-orbit coupling of a topological insulator.

In the latter case this results in Majorana zero-modes appearing in the band gap at the interface between the superconductor and a topologically insulating wire. In 3D this corresponds to states bound to the core of Abrikosov vortices and in 2D they are pinned to the edge between the topological insulator and the superconductor, much like a superconducting counter-part of a Shockley state [53, 54]. This superconducting counter-part however is a special case, protected by charge conjugation symmetry as demonstrated by the energy schematic in the right panel of figure 1.1. The associated topological invariant with these states is $Q = \mathbb{Z}_2$ as the zero-modes can either be present or not [55].

If $C^2 = -1$, and we consider $C = i\tau_y$ to be spinful, the BdG Hamiltonian can be expressed in terms of the two separate spin components and will then take the form

$$H^{BDG}_\pm = \begin{pmatrix} H_\pm - E_F & \mp\Delta_\pm \\ \mp\Delta^*_\pm & E_F - H^*_\pm \end{pmatrix}, \tag{1.2}$$

where H_0 and Δ_0 are direct sums of H_+, H_- and Δ_+, Δ_- respectively [56].

Chiral symmetry anticommutes with Hamiltonian, hence $\chi H \chi = -H$ and $\chi^2 = 1$. It is often associated with the presence of two sublattices in finite systems (often labelled A,B) where the Hamiltonian can be written in the block diagonal form

$$H_{\mathcal{C}} = \begin{pmatrix} 0 & H_{AB} \\ H_{AB}^{\dagger} & 0 \end{pmatrix}. \tag{1.3}$$

The blocks H_{AB} are of dimensions $m1 \times m2$ (where $m1$ and $m2$ count the size of each sublattice), while the chiral operator takes the form $\chi = diag(\mathbb{1}_{m1}, -\mathbb{1}_{m2}) = \tau_z$. Anti-commutation of the chiral symmetry with the Hamiltonian indicates that energy levels appear in pairs around the Fermi energy, hence giving rise to a symmetric spectrum. If the dimensions of H_{AB} are such that $m1 = m2$ all states are paired up, but when $m1 \neq m2$ there are $\nu = |m1 - m2|$ states pinned at the Fermi energy, which are localised onto one sublattice [57]. If $\nu > 0$ the eigenstates of the eigenvalues pinned at the Fermi energy take the form $\psi = (0, \psi_B)^T$ with $H_{AB}\psi_B = 0$, whilst if $\nu < 0$ the eigenstates take the form $\psi = (\psi_A, 0)^T$ with $H_{AB}^{\dagger}\psi_A = 0$ [56].

1.3.2 Example: SSH Model

The simplest topological one dimensional model is the Su-Schrieffer-Heeger (SSH) model. This provides a tight binding description of the charge fractionalisation which was first discovered in Polyacetylene molecules [19]. These molecules are long polymers containing alternating single and double bonds between carbon atoms on the backbone. In the tight binding approximation each unit cell consists of two different atoms, denoted as A and B. Consider a configuration as shown in upper panel of figure 1.2. A sites are denoted in red, B sites denoted in blue. The unit cell for such a structure contains a single bond, t_1, which connects the A and B site together. All adjacent unit cells are connected by a double bond, t_2, where only nearest neighbours are taken into account. This is called the α phase.

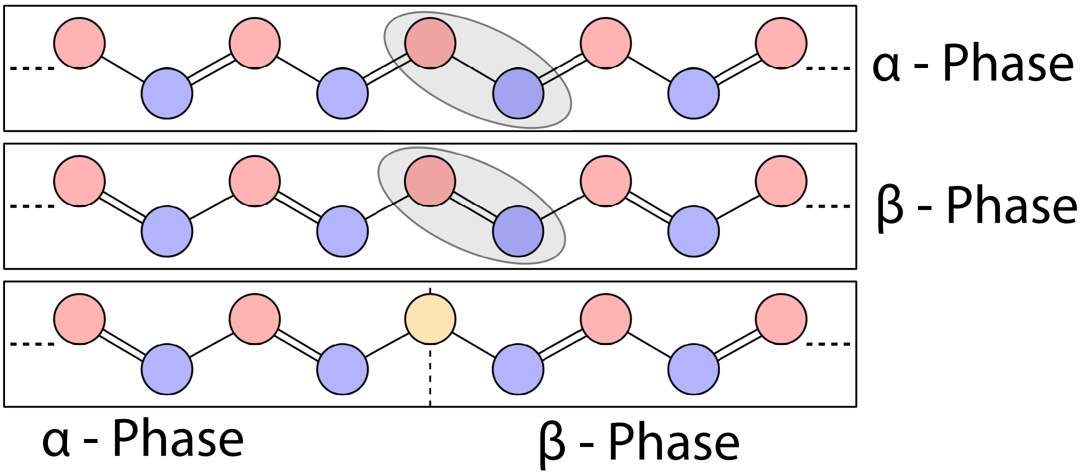

Figure 1.2: Su-Schrieffer-Heeger model showing the different bulk phases of the chain. Red lattice sites are A sites, blue lattice sites are B sites and the orange lattice site indicates a defect. The unit cells for the bulk phases are given by the grey dimer. The upper panel contains the α phase, where the bulk is topologically trivial, the middle panel contains the β phases, where the bulk is topologically non-trivial. The bottom panel shows both phases brought together by a dimerisation defect, which is connected to either side by single bonds.

The tight binding equations for such a structure are

$$\epsilon\psi_n^{(A)} = t_1\psi_n^{(B)} + t_2\psi_{n-1}^{(B)} \tag{1.4a}$$

$$\epsilon\psi_n^{(B)} = t_1\psi_n^{(A)} + t_2\psi_{n+1}^{(A)}. \tag{1.4b}$$

The associated Bloch equation is $H_{SSH}\psi_{SSH} = \epsilon\psi_{SSH}$, where H_{SSH}

$$H_{SSH}(k) = \begin{pmatrix} 0 & t_1 + t_2e^{-ika} \\ t_1 + t_2e^{ika} & 0 \end{pmatrix}, \tag{1.5}$$

and a is the real-space distance between neighbouring carbon atoms (from here on $a = 1$) and $\psi_{SSH} = (\psi_A, \psi_B)^T$. The corresponding dispersion and eigenvectors are

$$\epsilon_{\pm} = \pm\sqrt{t_1^2 + t_2^2 + 2t_1 t_2 \cos k} \tag{1.6}$$

and

$$u_{\pm} = \begin{pmatrix} \frac{\epsilon_{\pm}}{t_1 + t_2 e^{ik}} \\ 1 \end{pmatrix}. \tag{1.7}$$

The two bands of the dispersion meet when $t_1 = t_2$. Earlier I stipulated that in the α phase the bond connecting the two lattice sites within the unit cell was a weaker single bond, so $t_1 < t_2$. If however for the same unit cell, $t_1 > t_2$, the two lattice sites will be connected by a stronger double bond as pictured in the middle panel of figure 1.2. These two phases are therefore separated by the band gap closing ($t_1 = t_2$).

The SSH-Hamiltonian is of the same form as the chiral Hamiltonian in equation 1.3. The chiral symmetry can be made explicit by re-writing the SSH-Hamiltonian in terms of the Pauli matrices (σ_i)

$$H_{SSH}(k) = \mathbf{d}(k) \cdot \boldsymbol{\sigma} = (t_1 + t_2 \cos k)\sigma_x + (t_2 \sin k)\sigma_y. \tag{1.8}$$

The chiral symmetry, given by σ_z, then anticommutes with the Hamiltonian as no terms are proportional to σ_z or the identity. In parameter space $H_{SSH}(k)$ is therefore confined to a plane, $\mathbf{d}(k) = (d_x, d_y, 0)$. The topological characteristics can be measured by the Berry phase, which in general for 1D systems is given by the Zak phase, defined as

$$\nu_j = i \oint_{BZ} \langle u_j(k) | \partial_k u_j(k) \rangle, \tag{1.9}$$

where $|u_j(k)\rangle$ is the j'th eigenvector of Bloch Hamiltonian.

For the SSH model I calculate the winding number for the Bloch state of the upper band corresponding to the + index of equation 1.6, which is given by the integral of the pseudo-spin vector around the Brillouin zone

$$\nu_{+} = \int dk(\langle \sigma_x \rangle, \langle \sigma_y \rangle, \langle \sigma_z \rangle), \tag{1.10}$$

where $\langle \sigma_i \rangle = \langle u_{+}(k)|\sigma_i|u_{+}(k)\rangle$ is the expectation value of Bloch wave-vector u_{+} given in equation 1.7.

In 2002 Ryu and Hatsugai [58] showed that by using the pseudo-spin vector, where the σ_z component is always 0, the contour is confined to a circle of radius t_2 in the complex plane. The winding number then counts how many times the Bloch eigenvectors encircle the origin when a contour is performed around the Brillouin zone. This number also counts the number of topological modes that are present. The origin corresponds to the point where the band gap closes and hence separates out the two topologically distinct phases. If $t_1 > t_2$ the origin is not enclosed by the contour and can be smoothly deformed away, categorised by no winding ($\nu_{+} = 0$), but if $t_2 > t_1$ then the origin is encircled ($\nu_{+} = 1$) and is topologically distinct. Figure 1.3 shows this for a few example parameters in both phases.

Since in this discussion I have mentioned nothing about edges or finite systems, this bulk description gives us a concept of topology but not of a physical phenomena or observable to measure.

However, in a finite system the difference between the two phases can be easily detected. In particular, for a finite system with an odd number of sites there is one more A site than B site as in the case of equation 1.3 for $m_1 \neq m_2$, $\nu = |m_1 - m_2| = 1$. In both the α and β phases the spectrum must be symmetric as demanded by the chiral symmetry. The additional eigenvalue must be located at $E = 0$. By examining the fully dimerized limit, in the α phase $t_1 = 1, t_2 = 0$ and the eigenstate is located on the edge where the t_1 bond is present. In the β phase where $t_1 = 0, t_2 = 1$, the eigenstate is located on the opposite edge where

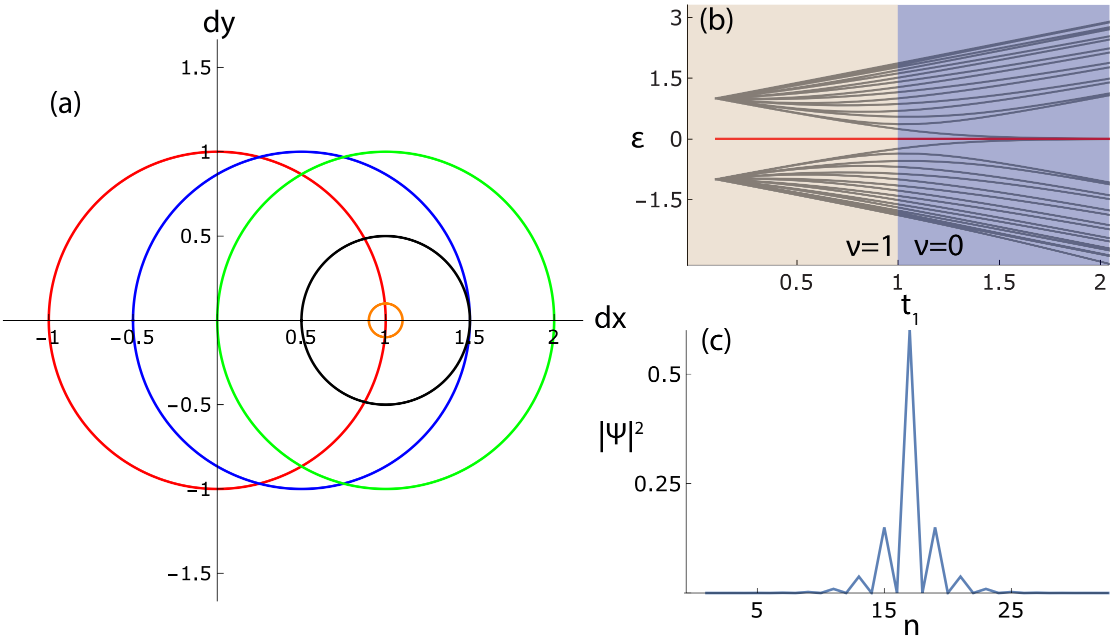

Figure 1.3: (a) Winding numbers for the SSH chain without a defect. Red and blue trajectories encompass the origin and hence are topologically non-trivial, whilst all other trajectories do not and are therefore trivial. Plotted for couplings $t_1 = 0, t_2 = 1.0$ (red), $t_1 = 0.5, t_2 = 1.0$ (blue), $t_1 = 1.0, t_2 = 1.0$ (green), $t_1 = 1.0, t_2 = 0.5$ (black) and $t_1 = 1.0, t_2 = 0.1$ (orange). (b) Numerical spectrum of the SSH chain with a defect for 16 dimers, plotted as a function of t_1, where $t_2 = 1.0$. The red line indicates a zero mode, which is topologically protected and an example of the wavefunction is given by that shown in figure (c) where $t_1 = 0.5, t_2 = 1$. For $t_1 > t_2$, the wavefunction is an extended state.

the t_2 bond is present. The eigenvalue pinned to zero energy has an eigenstate which is located on one sublattice ($H^{\dagger}_{AB}(k)\psi_A = 0$, with $\psi_B = 0$) [57]. Moving away from the fully dimerized limit, spatially this eigenstate exponentially decays away from the edge of the system. This edge now acts as an interface with the vacuum which is topologically trivial.

Moving the zero-mode to a different location requires a different type of interface. Since we have a trivial phase and a non-trivial phase, we can simply connect them together via a defect. This has been show in the lower panel of figure 1.2, where the defect coloured in orange is connected to both the α and β phases by weak t_1 couplings. This topological defect has the same properties as the edge state, i.e. if we look at the spectrum given in panel (b) of figure 1.3, there is clearly one edge mode which persists. Inspection of the wavefunction shows that it is entirely localised onto one sublattice, but now decays exponentially in both directions (see panel (c), shown for the topologically non-trivial region).

1.4 Consequences of non-Hermicity

Beyond the examples of Hermitian symmetries, in 1998 Bender and Boettcher [59–61] showed that a Hamiltonian need not be Hermitian to have a completely real spectrum. This broke the traditional view of quantum mechanics, that Hermicity was a requirement to describe quantum systems. In relaxing this constraint, they noticed that some non-Hermitian Hamiltonians were capable of displaying partially or entirely real spectra if there was an additional symmetry, a space-time reflection symmetry known as Parity-Time ($\mathcal{PT}$) symmetry. Whilst genuine non-Hermitian quantum systems have not been discovered, this concept has found many important applications in analogous settings, such as photonic systems.

This section introduces a two-level model which describes how we can understand a few of the physical consequences of non-Hermitian physics, in particular special spectral degeneracy points and the role of $\mathcal{PT}$ symmetry and $\mathcal{PT}$ symmetry breaking.

1.4.1 Two-level model and avoided crossings

Suppose we have the following two-level Hamiltonian $H = H_0 + \lambda H_1$, broken up into an unperturbed system H_0 containing two modes and a corresponding off-diagonal perturbation H_1, where H_0 and H_1 are given by

$$H_0 = \begin{pmatrix} E_1 & 0 \\ 0 & E_2 \end{pmatrix}, \qquad H_1 = \begin{pmatrix} 0 & \alpha \\ \beta & 0 \end{pmatrix}. \tag{1.11}$$

Here E_1 and E_2 are the natural energies of the two modes, λ is the perturbation strength, which we demand to be a positive scalar and α, β are coupling parameters. Considering only H_0, the two corresponding modes of H_0 are completely independent, even if they become degenerate, i.e. $E_1 = E_2$. By introducing the difference between the natural energies $\Delta = E_1 - E_2$ and varying Δ, the consequences of non-Hermicity on degenerate points and avoided crossings can be explored as the coupling parameters are turned on.

Firstly, considering the hermitian case, hermicity of H (that is $H = H^\dagger$) is satisfied if $\alpha = \beta^*$ (I will consider $\alpha = \beta$ and $\alpha, \beta \in \mathbb{R}$ for simplicity). The eigenvalues of H are given by

$$E_\pm = \frac{1}{2}(E_1 + E_2) \pm \frac{1}{2}\sqrt{(E_1 - E_2)^2 + 4\lambda^2\alpha^2}, \tag{1.12}$$

with corresponding eigenvectors

$$\psi_+ = \frac{1}{\sqrt{N}} \begin{pmatrix} 1 \\ \frac{E_+ - E_1}{\lambda\alpha} \end{pmatrix}, \qquad \psi_- = \frac{1}{\sqrt{N}} \begin{pmatrix} 1 \\ \frac{E_2 - E_-}{\lambda\alpha} \end{pmatrix}, \tag{1.13}$$

where $1/\sqrt{N}$ is the appropriate normalisation. For these two modes plotting $E_\pm$ in the interval $-x \leq \Delta \leq x$ for $\alpha = 0$, as sketched in the left panel of figure 1.4, demonstrates that there is no gap between E_+ and E_- at $\Delta = 0$. This degenerate touching point of the bands is referred to as a diabolic point. Furthermore it is very quickly apparent by inspecting ψ_+ and ψ_- that at this point the modes are indeed distinct. This degeneracy where the eigenvectors are distinct is called a diabolic point. For any finite α, $4\lambda^2\alpha^2$ is positive and hence a gap opens for all values of Δ, with a gap corresponding to $4\lambda\alpha$ at $\Delta = 0$, as shown in the middle panel of figure 1.4.

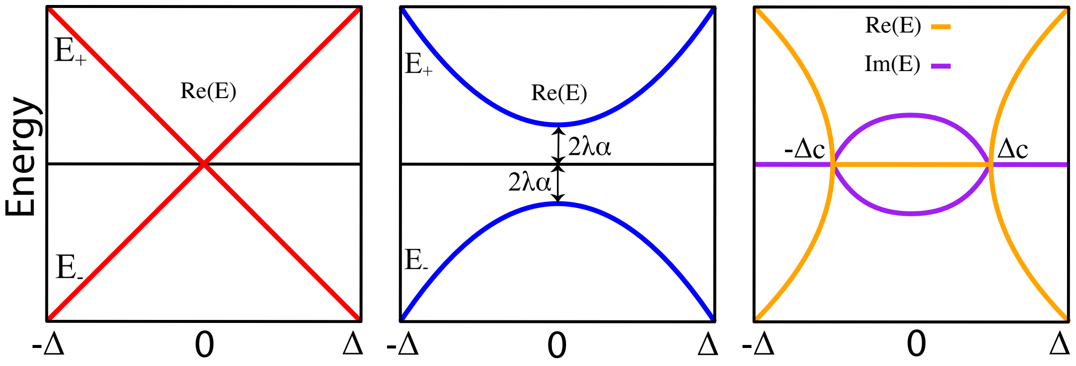

Figure 1.4: Sketches of different types of band touching points for two-level systems for no interaction $\alpha = \beta = 0$ (left), Hermitian interactions $\alpha = \beta \neq 0$, $\alpha, \beta \in \mathbb{R}$, resulting in an avoided crossing with gap of size $4\lambda|\alpha|$ (middle) and non-Hermitian interactions where $\alpha = -\beta$, displaying the square root branch points at $\pm\Delta_c$ (right), which join real eigenvalues (orange) to imaginary eigenvalues (purple).

1.4.2 Exceptional Points and $\mathcal{PT}$-symmetry

If the condition for Hermicity is broken, $|\alpha|^2$ is replaced with $\alpha\beta$ in equation 1.12, where now $\alpha \neq \beta^*$. This does not strictly need to be a positive definite, hence in general the square root in equation 1.12 can be imaginary and as a function of Δ the eigenvalues $E_\pm$ can therefore be complex.

Avoided crossings can then be pushed into the complex plane, and from the square root branch points eigenvalues can form a different type of spectral singularity/coalescence known as exceptional points. To highlight this, consider the special case where $E_1 = -E_2$. The bare energy difference Δ now takes the form $\Delta = 2E_1$ and $E_\pm = \pm\sqrt{\Delta^2 + 4\lambda\alpha\beta}$. Consider $\alpha = -\beta$, and $\alpha, \beta \in \mathbb{R}$. By varying Δ figure 1.4 shows that regions of real eigenvalues are connected to regions of imaginary eigenvalues via points where $E_+ = E_- = 0$. These points, called exceptional points are referred to as coalescences. This will be discussed more explicitly later on.

The position of these exceptional points can be pushed around in the complex plane by varying the strength parameter λ and the values of α, β. In fact critical values Δ_c occur when $E_\pm = 0$, which happens when $\Delta^2 = -4\lambda\alpha\beta$ and hence

$\Delta_c = \pm 2\sqrt{\lambda\alpha\beta}$.

The special case discussed here, depicted when $\alpha = -\beta$, results in eigenvalues that are forced to either be imaginary or real; this is sometimes referred to as pseudo-Hermitian. If the perturbation H_1 contained diagonal terms or relaxation of the constraint $E_1 = -E_2$ then the expression for the critical values for the exceptional points would in general be shifted into the complex plane, and fine tuning of the diagonal terms of H_0 and H_1 would be required to recover this special case.

This example belongs to the class of Hamiltonians which are parity-time ($\mathcal{PT}$) symmetric in the regions where the eigenvalues are real. $\mathcal{PT}$-symmetric Hamiltonians were first investigated by Bender and Boettcher [59] in the context of complex cubic Hamiltonians and later on for a range of complex Hamiltonians of different degree polynomials of momentum and position operators, which display either entirely real spectra or partly real and partly complex spectra depending on the degree [62]. More in-depth reviews beyond the scope of this discussion exist in this review [61].

$\mathcal{PT}$-symmetry is a combination of parity $\mathcal{P}$ (given in this representation by $\mathcal{P} = i\sigma_x$.) and time reversal symmetry $\mathcal{T}$ (given in this representation by complex conjugation $\mathcal{T} = K$), which commute with the Hamiltonian and form $\mathcal{PT}$ symmetry. In this example, the exceptional point represents a spectral transition into a region where parity and hence $\mathcal{PT}$-symmetry is broken and eigenvalues are no longer real but come in complex conjugate pairs. Hence we can use these spectral transitions to identify when $\mathcal{PT}$-symmetry is broken, a feature I will rely on in chapters 2 and 3. Examining the modes of $E_\pm$ highlights an important additional consequence which occurs at the exceptional point. Away from the exceptional point, the corresponding linearly independent eigenvectors are again given by

$$\psi_+ = \frac{1}{\sqrt{N}}\begin{pmatrix} 1 \\ \frac{E_+ - E_1}{\lambda\alpha} \end{pmatrix}, \qquad \psi_- = \frac{1}{\sqrt{N}}\begin{pmatrix} 1 \\ \frac{E_2 - E_-}{\lambda\alpha} \end{pmatrix}. \tag{1.14}$$

Using the conditions that I previously stipulated, $E_1 = -E_2$ and at the exceptional point Δ_c is such that $E_\pm = 0$, these two eigenvectors become identical resulting in only one linearly independent eigenvector $\psi_+ = \psi_- = \frac{1}{\sqrt{N}} \begin{pmatrix} 1 & \frac{E_2}{\lambda\alpha} \end{pmatrix}^T$. This behaviour of the eigenvectors is referred to as a coalescence and not a degeneracy because the two degenerate eigenvalues belong to one linearly independent eigenvector and not two.

The presence of exceptional points can also be identified by making use of the concept of left and right eigenstates instead of simply inspecting the eigenstates. Non-Hermitian Hamiltonians have left and right eigenstates which satisfy the following eigenvalue equations

$$\langle L_n|H = \langle L_n|\epsilon_n \quad \text{and} \quad H|R_n\rangle = \epsilon_n|R_n\rangle \tag{1.15}$$

respectively, but generally are distinct, i.e. $\langle L_n| \neq |R_n\rangle^\dagger$. They form a biorthogonal basis, $\langle L_n|R_m\rangle = \delta_{nm}$, and completeness is satisfied if

$$\Sigma_n|R_n\rangle\langle L_n| = 1. \tag{1.16}$$

At the exceptional point, $\langle L_n|R_n\rangle$ vanishes [63], hence biorthogonality cannot be fulfilled. During this thesis I will make use of this property in order to identify phase transitions in parameter space where exceptional points emerge. This is signified by a divergence in the Petermann factor [64]

$$K = \frac{\langle L|L\rangle\langle R|R\rangle}{|\langle L|R\rangle|^2}, \tag{1.17}$$

which measures non-orthogonality in vicinity of exceptional points [65].

1.4.3 Time evolution, geometric phases and interchange of eigenstates

The states of a physical system described by H evolve over time according to the operator $\hat{U}(t) = e^{-iHt}$. Acting on eigenstates of H this evolution gives the familiar phase factors $e^{-iE_n t}$. Since E_n will not always be real for non-Hermitian Hamiltonians, these phase factors will decay or grow with rate Γ. This rate Γ is defined by splitting the eigenvalues of H into their real and imaginary components, $E_n = E_{re} + iE_{im}$, and considering the consequences on the phase factors given by time evolution: $e^{-i(E_{re}+iE_{im})t} = e^{-iE_{re}t}e^{-E_{im}t}$, where $\Gamma = -2E_{im}$.

In addition to the phase factors which come from the time evolution alone, Berry [66] discovered a second type of phase factor, $\beta(C)$, which is accumulated when a diabolic point is encircled adiabatically in parameter space, where adiabatic traversal is necessary, such that the evolution at any instance corresponds to stationary eigenstates of the Hamiltonian. When a complete loop is performed, the eigenstate returns to its original state up to a phase, which besides the dynamical component from the instantaneous energies include an additional, geometric contribution. These phase factors are also known as geometric phases as they measure the curvature of the parameterised space of the Hamiltonian. The winding numbers of the 1D SSH model in the previous chapter are an example of such phases.

The geometric phase $\beta(C)$ accumulated over such a closed loop (C), for a Hermitian system prepared in eigenstate $|\Psi(\kappa)\rangle$, is given by

$$\beta(C) = i \oint_C \langle\Psi(\kappa)|\nabla\Psi(\kappa)\rangle d\kappa, \tag{1.18}$$

where κ is an appropriate parametrisation of H. If H is non-Hermitian however, and one tries to traverse an exceptional point, the expression for the geometric phase must take into account the left eigenstates $\langle\tilde{\Psi}(\kappa)|$ introduced in the previous section. The geometric phase becomes

$$\tilde{\beta}(C) = i \oint_C \langle\tilde{\Psi}(\kappa)|\nabla\Psi(\kappa)\rangle d\kappa. \tag{1.19}$$

Determining the geometric phase in the Hermitian case reveals that one full complete cycle around the diabolic point is sufficient to return the eigenstates to its initial state with the additional geometric phase of π. Thus two complete trips must be made to pick up a full phase of 2π. If the same process is completed by avoiding the diabolic point, no additional phase is achieved.

An interesting consequence is revealed in the non-Hermitian case, where encircling exceptional points shows that pairs of eigenstates are exchanged after a full loop and after repeated loops they obey the pattern

$$|\Psi_1\rangle \to -|\Psi_2\rangle \to -|\Psi_1\rangle \to |\Psi_2\rangle \to |\Psi_1\rangle, \tag{1.20}$$

indicating that four complete loops are required to return to the original state with a full geometric phase of 2π. As noted in reference [63] and experimentally verified using microwave cavities [67, 68], the directionality of the loop C determines the signs and hence implies a chirality associated with C. These examples were for static measurements of the spectra and eigenmodes and hence do not represent adiabatic, true-time dependant encircling of the exceptional point. Such measurements so far have remained elusive, as in the presence of gain and loss non-adiabatic mode switching occurs [69, 70], which is dependent on the parametric direction of the loop [71–73].

Chapter 2

Coupled resonators optical waveguides

Microcavities or microresonators, most commonly grown and etched in dielectric materials, confine light to very small volumes where the desired confinement is measured by quality factors $Q = \omega\tau$ which measure how long modes of a specific frequency remain confined ($\tau = 1/\Gamma$ for decay rate Γ) or equivalently how broad they are ($\Delta\omega = 1/\tau$). Limiting factors for this confinement include properties such as the resonator's geometry, surface roughness and material attenuation factors.

Various designs for different microcavities exist which change the degree of confinement of the light, resulting in different quality factors. Some examples of microcavities include the more traditional Fabry-Perot micropillar, photonic crystals, microdiscs, microtoroids and microspheres [74]. Quality factors in these types of designs can range from high (for pillars and crystals with $Q \sim 10^4 - 10^5$) to ultrahigh (microdiscs and spheres $Q \sim 10^8$) [75], whilst different designs confine light in different dimensions. Further control of the confinement in the case of micropillars can be achieved with the use of Bragg mirrors, where emission can be directed into a single direction or plane as in the case of lasers or single photon sources [76]. In microspheres the strong confinement of light can be used to detect when molecules bind to the surface. The resonances within the cavity experience a shift in wavelength, broadening of the resonance and even splitting [77], making the resonators ideal for highly sensitive sensing [78].

In this chapter I focus on devices where the operational regime results in whispering gallery modes. These are optical modes which propagate by total internal reflection around the insides of a structure. From the list of examples above these include microspheres, microtoroids and microdiscs, where this discussion will be confined to microdiscs. A wide range of applications for microresonators include low threshold lasing [79], nanoparticle sensing [80], unidirectional emission from deformed cavities [81] and non-linear optics [82].

I will describe how the counter propagating whispering gallery modes inside circular disc geometries can be asymmetrically backscattered by introducing defects to the surface of the discs, and how from the perspective of standing waves this gives rise to effective gain and loss to the respective modes and an asymmetry in the direction of propagation around the internal edge of the disc. Coupling these resonators evanescently together in $1D$ chains, I will demonstrate how the internal backscattering can lead to non-Hermitian phases which support topological defect states localised at an interface. Since an interface state is different from an edge state in the sense that it arises from locally breaking translational invariance, I will then show that further asymmetries and disorder can be introduced to the chain to break the translational invariance throughout the chain and hence show that these states are robust to large and non-local perturbations, signifying that they are of a topological nature.

The topological modes discussed in this chapter have no fermionic analogue as they belong to a non-Hermitian extension of the BDI symmetry class, the chiral symmetry class with time reversal symmetry. The topological modes are a direct result of the openness of the system in a physical setting which is achievable to experiments. The resonances themselves are spectrally isolated and have long lifetimes, making such phenomena more easily observable.

2.1 Coupled Resonators

In circular resonator geometries with sufficiently smooth edges, light travels in closed circular paths by total internal reflection. The travelling waves in such a cavity occur in spectrally degenerate orthogonal pairs which circulate in opposite directions, hence giving rise to the names clockwise (CW) and counter-clockwise (CCW) propagating modes. This description originates from the Helmholtz equation for dielectric cavities where solutions are travelling modes of the form $\phi_{TW}(\theta) \propto e^{im\theta}$. The quantum number m plays the role of orbital angular momentum which is positive for CCW modes and negative for CW modes such that they counter propagate [83]. The corresponding contributions to the frequency ($\propto m^2$) are two-fold degenerate if $|m| \neq 0$. In such a case the eigenstates can be superimposed in pairs of $+m$ and $-m$ to produce new eigenstates, standing waves of the form $\cos m\phi$ and $\sin m\phi$.

For now focusing on the travelling wave basis, the two travelling waves can be grouped into the two-component vector $\psi_n^{TW} = \begin{pmatrix} a_n & b_n \end{pmatrix}^T$, where a_n and b_n are the amplitudes of the CW and CCW modes respectively and n enumerates the resonator. Travelling modes can be expressed as the superposition of standing waves given by cosine ($|c\rangle$) and sine ($|s\rangle$) waves: $|CW\rangle = \sqrt{\frac{1}{2}}(|c\rangle + i|s\rangle)$, $|CCW\rangle = \sqrt{\frac{1}{2}}(i|c\rangle + |s\rangle)$. This transformation can be rewritten in matrix form, $\psi^{SW} = S\psi^{TW}$, where

$$S = \frac{1}{\sqrt{2}} \begin{pmatrix} 1 & i \\ i & 1 \end{pmatrix}. \tag{2.1}$$

For an isolated circular resonator both of the travelling modes propagate with resonance frequency Ω_0. Deforming the resonator geometry slightly leads to asymmetric internal scattering. Such effects can likewise be introduced by adding notches, scattering by nanoparticles or tunnelling into chromium tips placed in close proximity to the surface of the disc [74, 84]. The distance between the disc and the loss inducing rods or the angle between pairs of nanoparticles can then be tuned to create the required asymmetry in the backscattering coefficients.

Asymmetric internal scattering means that modes are converted from CW to CCW with amplitude A, whilst CCW modes are converted to CW modes with amplitude B. The single resonator Hamiltonian is therefore

$$H_{TW} = \begin{pmatrix} \Omega_0 & A \\ B & \Omega_0 \end{pmatrix}. \tag{2.2}$$

For $A \neq B^*$ the internal scattering is asymmetric and hence H_{TW} is non-Hermitian. Whilst Hermicity is broken ($H \neq H^\dagger$), reciprocity still remains present, a constraint which requires the Hamiltonian in the standing wave basis to be symmetric ($H_{SW} = H_{SW}^T$). In the standing wave basis reciprocity takes the form

$$H_{SW} = \begin{pmatrix} \alpha & \beta \\ \beta & \gamma \end{pmatrix}. \tag{2.3}$$

Using the transformation S, the reciprocal Hamiltonian in the travelling wave basis is given by

$$H_{TW} = S^\dagger H_{SW} S = \frac{1}{2} \begin{pmatrix} (\alpha+\gamma)/2 & i\beta + (\alpha-\gamma)/2 \\ -i\beta + (\alpha-\gamma)/2 & (\alpha+\gamma)/2 \end{pmatrix} \tag{2.4}$$

where the coefficients of H_{TW} correspond with equation 2.2, where $\Omega_0 = (\alpha+\gamma)/2$, $A = i\beta + (\alpha-\gamma)/2$ and $B = -i\beta + (\alpha-\gamma)/2$, demonstrating reciprocity.

The previously degenerate eigenfrequencies Ω_0 for $A = B = 0$ now split according to $\Omega_\pm = \Omega_0 \pm \sqrt{AB}$ as the travelling modes hybridise. The corresponding eigenvectors are given by $v_\pm = (|A| + |B|)^{-\frac{1}{2}} \begin{pmatrix} \sqrt{A} & \pm\sqrt{B} \end{pmatrix}^T$, where the imbalance in the components is measured by the chirality

$$\alpha = \frac{|A| - |B|}{|A| + |B|}, \tag{2.5}$$

which approaches 1 when $|A| \gg |B|$ and -1 when $|A| \ll |B|$.

When a resonator is brought within tunnelling distance of another resonator, evanescent coupling couples CW (CCW) modes of one resonator to CCW (CW) modes of the other resonator preserving the angular momentum of the modes. Inter-resonator backscatter from CW to CW and CCW to CCW modes is highly suppressed if the resonator surface is smooth on the scale of a wavelength [14, 85, 86]. The coupling matrix between individual resonators is therefore given by

$$T = \begin{pmatrix} 0 & W \\ W & 0 \end{pmatrix}, \tag{2.6}$$

where W is the inter-resonator coupling. The form of this coupling matrix is justified by considering the coupling operator between two resonators in the standing wave basis. Using the definitions associated with equation 2.3, the coupling operator takes the form

$$\begin{aligned} \hat{t} = & W_{cc}(|c\rangle\langle c'| + |c'\rangle\langle c|) + W_{ss}(|s\rangle\langle s'| + |s'\rangle\langle s|) \\ & + W_{cs}(|c\rangle\langle s'| + |s'\rangle\langle c|) + W_{sc}(|s\rangle\langle c'| + |c'\rangle\langle s|), \end{aligned} \tag{2.7}$$

where W_{ij} are the coupling coefficients between the resonators determined by the distances between the resonators and states denoted with a prime belong to the second resonator. Transforming this into the standing wave basis the coupling operator becomes

$$\begin{aligned}\hat{t} =&W_+(|\mathrm{CW}\rangle\langle\mathrm{CW}'| + |\mathrm{CCW}'\rangle\langle\mathrm{CCW}|)\\ &+W_-(|\mathrm{CCW}\rangle\langle\mathrm{CCW}'| + |\mathrm{CW}'\rangle\langle\mathrm{CW}|)\\ &+W'_+(|\mathrm{CW}\rangle\langle\mathrm{CCW}'| + |\mathrm{CW}'\rangle\langle\mathrm{CCW}|)\\ &+W'_-(|\mathrm{CCW}\rangle\langle\mathrm{CW}'| + |\mathrm{CCW}'\rangle\langle\mathrm{CW}|),\end{aligned} \tag{2.8}$$

where

$$\begin{aligned}W_\pm =&\frac{W_{cc} + W_{ss} \pm i(W_{sc} - W_{cs})}{2},\\ W'_\pm =&\frac{W_{cc} - W_{ss} \pm i(W_{sc} + W_{cs})}{2}.\end{aligned} \tag{2.9}$$

Since within the approximation of coupled-mode theory, adjacent resonators are coupled evanescently and hence backscattering is suppressed, this means $W_{cc} + W_{ss} \approx 0$ and $W_{sc} - W_{cs} \approx 0$. Additionally, since I assume that the surfaces of the resonators are both smooth and symmetric in the vicinity of the point of closest approach of the two resonators, $W_{cs}, W_{sc} \approx 0$. Hence the terms $W_\pm$ vanish and $W'_\pm = W_{cc} = W$. The coupling operator can then be written in matrix form

$$t = \begin{pmatrix} 0 & W \\ W & 0 \end{pmatrix}. \tag{2.10}$$

A chain of resonators can then be connected together using the coupled-mode approximation (analogous to the tight-binding model), as depicted in panel a) of figure 2.1. In the travelling wave basis (where the TW labels have been suppressed) this wave equation takes the form

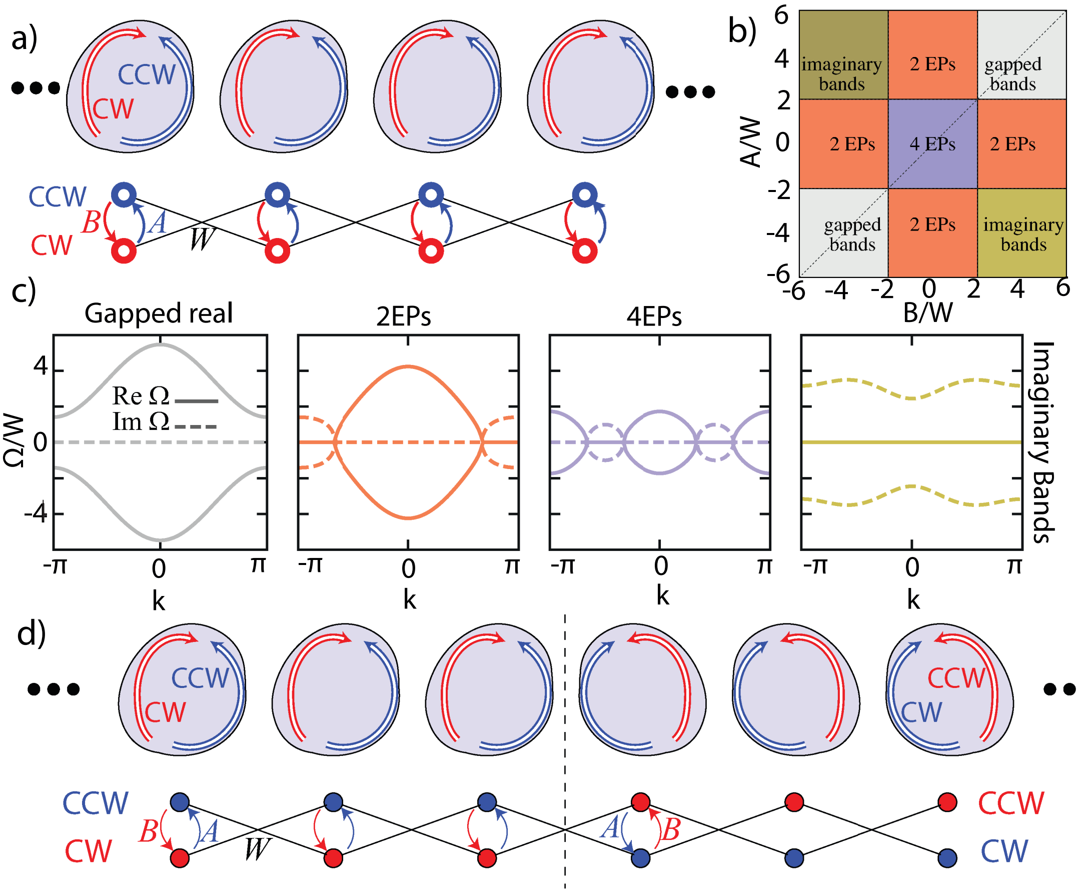
a)
CCW
CW
CCW
CW
B
A
W
b)
imaginary bands
2 EPs
gapped bands
2 EPs
4 EPs
2 EPs
gapped bands
2 EPs
imaginary bands
A/W
B/W
6
4
2
0
-2
-4
-6
c)
Gapped real
2EPs
4EPs
Imaginary Bands
Re Ω
Im Ω
Ω/W
4
0
-4
-π
0
π
k
d)
CCW
CW
CCW
CW
B
A
W
A
B
CCW
CW

Figure 2.1: a) Sketches of deformed coupled resonators and tight binding chain schematic with internal backscattering couplings (A and B) and inter-resonator coupling W which couples CW (CCW) modes of one resonator to CCW (CW) modes of adjacent resonators. b) Phase diagram of the bulk dispersion given by equation 2.13, where phase space is separated into regions of real gapped bands, imaginary gapped bands, 2 exceptional points and 4 exceptional points. c) corresponding dispersions of complementary coloured phase from b). d) Sketch of chain where the dotted line indicates where the defect occurs, resulting in the opposite resonator deformation and inversion of the backscattering couplings.

$$\omega_n \psi_n = H_n \psi_n + T(\psi_{n+1} + \psi_{n-1}). \tag{2.11}$$

Solutions to this equation are of the normal Bloch form $\psi_n = e^{ikn}\Psi$, which when substituted into the wave equation gives the Bloch Hamiltonian

$$H(k) = \begin{pmatrix} \Omega_0 & A + 2W\cos k \\ B + 2W\cos k & \Omega_0 \end{pmatrix}. \tag{2.12}$$

The corresponding dispersion is $\omega_\pm(k) = \Omega_0 \pm \Omega(k)$, where

$$\Omega(k) = \sqrt{(A + 2W\cos k)(B + 2W\cos k)}. \tag{2.13}$$

The two bands, labelled by ±, are chirally symmetric about Ω_0, where the chiral symmetry is given by $\sigma_z H(k)\sigma_z = -H(k)$. Exact numerical calculations have shown that parameters A, B and W are almost real and by fine tuning the shape parameters of the resonator can be made exactly real. The Hamiltonian is then $\mathcal{PT}$ symmetric, where in this basis $\mathcal{PT}$ symmetry is given by complex conjugation $\mathcal{K}$.

Panel b) and c) of figure 2.1 shows that $\Omega_\pm$ has entirely real and gapped bands if $|A/2W| > 1$, $|B/2W| > 1$ and $AB > 0$, while it displays imaginary and gapped bands if for the same conditions $AB < 0$. The rest of the phase space contains ranges of both imaginary and real bands in separate ranges of k, joined by exceptional points when $\Omega_\pm = 0$ and hence $-A/2W = \cos k$ or $-B/2W = \cos k$.

Transforming the Bloch Hamiltonian into the standing wave basis using the transformation $SH_{TW}(k)S^\dagger = H_{SW}(k)$,

$$H_{SW} = \begin{pmatrix} 2\Omega + i(A - B) & A + B + 4W\cos k \\ A + B + 4W\cos k & 2\Omega - i(A - B) \end{pmatrix}, \tag{2.14}$$

reveals the underlying $\mathcal{PT}$ symmetry when $A \neq B$, given by the passive gain and loss terms $i(A-B)$ and $-i(A-B)$ for $A > B$ respectively (the roles of these terms reverse if $A < B$). Time reversal symmetry is realised by the condition of reciprocity ($H = H^T$), which is indeed true as H_{SW} is a symmetric Hamiltonian, whilst parity symmetry takes the form $\mathcal{P} = \sigma_x$. In this basis chiral symmetry is transformed in $\mathcal{C} = \sigma_y$ and commutes with $\mathcal{PT}$ symmetry.

Returning to the travelling wave basis, as discussed in the previous chapter, $\mathcal{PT}$ symmetry $H(k) = H(k)^*$ makes the eigenvalues of $H(k)$ either real or appear in complex conjugate pairs. In combination with the chiral symmetry $\sigma_z H(k)\sigma_z = -H(k)$ this forms the charge conjugation symmetry $\sigma_z H(k)\sigma_z = -H(k)^*$. Eigenvalues then appear in the complex conjugate pairs $\Omega_\pm = -\Omega_\pm^*$.

In the Hermitian setting, I would expect that the eigenstates of this chain do not display any topological protection. Convention from Hermitian systems uses the interface with air/vacuum to demonstrate a change in topological index (air/vacuum being trivial) between material and air/vacuum. One such method of measuring the topological index for $A = B$, would be to consider the winding number given by the winding of the pseudo-spin vector $\vec{S}$ around the Brillouin zone. Since the pseudo-spin vector is not constrained to a single plane, encompassing the origin, the trajectory can be adiabatically deformed and ultimately completely removed. This renders the natural choice for the topological index trivial in the Hermitian limit of this system.

Interestingly however, in a departure from Hermitian convention, I will demonstrate in the next section that by introducing a mirror symmetry in the form of a defect in the orientation of the resonators with respect to the entire chain, a spectral phase transition accompanies the appearance of topologically protected defect states, despite each sub-system being topologically trivial.

2.1.1 Defect states and wave matching

I now consider the consequences of an interface in the chain of resonators. Placed at $n = 0$, this interface exchanges the roles of the backscattering amplitudes A and B in the second half the chain as depicted in panel d) of figure 2.1. For the wave equation given in equation 2.11 the following amendments are made: Firstly the wave equation is shifted with respect to the central frequency Ω_0 by setting $\Omega_n = \omega_n - \Omega_0$ and secondly the single-resonator Hamiltonian before and after the defect now takes the form

$$H_n = \begin{cases} \begin{pmatrix} 0 & A \\ B & 0 \end{pmatrix} (n < 0) \\ \begin{pmatrix} 0 & B \\ A & 0 \end{pmatrix} (n \geq 0). \end{cases} \tag{2.15}$$

Solutions to the wave equation, which belong to topological modes, will decay exponentially either side of the interface. In general, solutions can be written in terms of the propagating factors $\lambda = e^{ik}$ in each half of the chain,

$$\psi_n = \lambda^n \phi. \tag{2.16}$$

These propagating factors correspond to decaying solutions if k is complex.

The wave equation becomes

$$\Omega\phi = H_n\phi + 2W(\lambda + \lambda^{-1})\phi, \tag{2.17}$$

where

$$\phi^{(L)} \propto \begin{pmatrix} A + 2W\cos k_i \\ \Omega \end{pmatrix} \tag{2.18}$$

$$\phi^{(R)} = \sigma_x \phi^{(L)} \propto \begin{pmatrix} \Omega \\ A + 2W\cos k_i \end{pmatrix}, \tag{2.19}$$

noting that $\lambda + \lambda^{-1} = 2\cos k$. Non-trivial solutions Ω of the wave equation on the left side of the interface occur when

$$\left\| \begin{matrix} -\Omega & A + 2W\cos k \\ B + 2W\cos k & -\Omega \end{matrix} \right\| = 0 \tag{2.20}$$

is satisfied. The two corresponding solutions are

$$2W\cos k_1 = -\frac{A+B}{2} + \sqrt{\frac{(A+B)^2}{4} + \Omega^2} \tag{2.21}$$

$$2W\cos k_2 = -\frac{A+B}{2} - \sqrt{\frac{(A+B)^2}{4} + \Omega^2}, \tag{2.22}$$

and the four propagating factors are

$$\lambda_1^{\pm} = \cos k_1 \pm \sqrt{\cos {k_1}^2 - 1} \equiv \cos k_1 \pm \sin k_1 \tag{2.23}$$

$$\lambda_2^{\pm} = \cos k_2 \pm \sqrt{\cos {k_2}^2 - 1} \equiv \cos k_2 \pm \sin k_2. \tag{2.24}$$

All four propagating factors are associated with both sets of Bloch vectors on each side of the interface. Additionally for each pair of propagating factors $(\lambda_i^+, \lambda_i^-)$, $\lambda_i^+ \lambda_i^- = 1$.

Defect states are comprised of superpositions of decaying solutions, where propagating wave factors λ_i are chosen from each pair $(\lambda_i^+, \lambda_i^-)$ such that $|\lambda_i| > 1$. The resulting defect states are of the form

$$\psi_{n<0}^{(L)} = a_1^{(L)} \lambda_1^{n+1} \phi_1^{(L)} + a_2^{(L)} \lambda_2^{n+1} \phi_2^{(L)} \tag{2.25}$$

$$\psi_{n\geq 0}^{(R)} = a_1^{(R)} \lambda_1^{-n} \phi_1^{(R)} + a_2^{(R)} \lambda_2^{-n} \phi_2^{(R)}. \tag{2.26}$$

The solutions either side of the interface must match continuously. This means that evaluated at $n = 0$ and $n = -1$, the wave matching conditions given by $\psi^{(L)} = \psi^{(R)}$ are

$$a_1^{(L)} \lambda_1 \phi_1^{(L)} + a_2^{(L)} \lambda_2 \phi_2^{(L)} = a_1^{(R)} \phi_1^{(R)} + a_2^{(R)} \phi_2^{(R)}. \tag{2.27}$$

Defect states can either come in symmetric ($a_i^{(L)} = a_i^{(R)}$) or antisymmetric ($a_i^{(L)} = -a_i^{(R)}$) form. For now I contain the discussion to the symmetric case, as the antisymmetric case can be recovered by applying the chiral symmetry operator σ_z (transforming solutions $\Omega \to -\Omega$ and Bloch wavevectors according to $\sigma_z \phi_i^{(R)} = \sigma_z \sigma_x \phi_i^{(L)} = -\sigma_x \sigma_z \phi_i^{(L)}$).

Substituting into this expression the definitions of $\phi_i^{(L)}$ and $\phi_i^{(R)}$ from equations 2.18 and 2.19 and collecting the coefficients a_1, a_2 into a vector, the defect states correspond to non-trivial solutions to the matrix equation

$$\underbrace{\begin{pmatrix} A + 2W\cos k_1 - \lambda_1 \Omega & A + 2W\cos k_2 - \lambda_2 \Omega \\ \Omega - \lambda_1 (A + 2W\cos k_1) & \Omega - \lambda_2 (A + 2W\cos k_2) \end{pmatrix}}_{M} \begin{pmatrix} a_1 \\ a_2 \end{pmatrix} = \mathbb{0} \tag{2.28}$$

which occur if $\left\| M \right\| = 0$. Solutions are given by

$$\Big[(A+2W\cos k_1)(A+2W\cos k_2)-\Omega^2\Big](\lambda_1-\lambda_2)-2W(\cos k_1-\cos k_2)(-1+\lambda_1\lambda_2)\Omega=0. \tag{2.29}$$

Noting that $(A+2W\cos k_1)(A+2W\cos k_2)=-\Omega^2$, this reduces to

$$W(1-\lambda_1\lambda_2)(\cos k_1-\cos k_2)=\Omega(\lambda_1-\lambda_2), \tag{2.30}$$

and multiplying through by $1-1/\lambda_1\lambda_2$ isolates the propagating factors in terms of only the eigenvalue of the defect state

$$2-\lambda_1\lambda_2-\frac{1}{\lambda_2\lambda_2}=2\frac{\Omega}{W}, \tag{2.31}$$

which can be used as a consistency check for any pair of propagating factors. If a pair of propagating factors contains at least one propagating factor which has $|\lambda_i|=1$, the corresponding mode will not be a defect state but a scattering state. If either propagating factor has $|\lambda_i|>1$, the state will be unphysical.

This condition can be manipulated further to show the corresponding eigenfrequency at which the defect states occur in terms of the real physical parameters $(A, B$ and $W)$. Using the definitions of λ_1, λ_2 given in equation (2.23) and (2.24) and inserting them into equation (2.31)

$$1-\cos k_1\cos k_2-\Omega/W=\pm\sin k_1\sin k_2, \tag{2.32}$$

then squaring the result

$$\cos^2_{k_1}\cos^2_{k_2} - 2\cos_{k_1}\cos k_2(1-\Omega/W) + (1-\Omega)^2 = \sin {k_1}^2 \sin {k_2}^2 \tag{2.33}$$

and using that

$$\cos k_1 \cos k_2 = [(\frac{A+B}{2})^2 - \Omega^2 - (\frac{A-B}{2})^2]/4W^2 \tag{2.34}$$

$$(\cos k_1 - \cos k_2)^2 = [\Omega^2 + \frac{A-B}{2}^2]/W \tag{2.35}$$

$$\sin {k_1}^2 \sin {k_2}^2 = (\cos {k_1}^2 - 1)(\cos {k_2}^2 - 1), \tag{2.36}$$

produces the condition

$$\Omega(\Omega - 2W)^2 - AB\Omega + (A-B)^2\frac{W}{2} = 0. \tag{2.37}$$

Solutions of Ω to this equation correspond to defect state that have a symmetric mode profile. Antisymmetric solutions can also be recovered by applying the chiral symmetry operator, where chiral symmetry maps $\Omega \to -\Omega$. The consistency condition becomes

$$2 - \lambda_1\lambda_2 - \frac{1}{\lambda_2\lambda_2} = -2\frac{\Omega}{W}, \tag{2.38}$$

and following the same procedure as for the symmetric solutions, the antisymmetric mode profiles occur for solutions to

$$-\Omega(\Omega + 2W)^2 + AB\Omega + (A-B)^2\frac{W}{2} = 0. \tag{2.39}$$

Both equations 2.37 and 2.39 are cubic equations. On inspection of the solutions, one root for each equation is always non-normalisable and hence there exist four unique solutions $(\Omega, -\Omega, \Omega^*, -\Omega^*)$. If these solutions do not fulfil the consistency conditions given by equation (2.31) and (2.38), they do not belong to defect states.

2.1.2 Phase Diagram

Recalling that the $\mathcal{PT}$ symmetry means that solutions Ω to equations 2.37 and 2.39 come in either real pairs or complex conjugate pairs indicates that solutions must become degenerate in the transition between these two spectral phases. The associated degeneracy between these two phases is an exceptional point. When the solutions are real pairs at least one of the two propagating factors will satisfy $|\lambda_i| = 1$, which corresponding to a scattering state and hence the phase contains no defect states. After the exceptional point the solutions are complex conjugate pairs which become defects states as both propagating factors satisfy $|\lambda_i| > 1$.

The phase boundary as a function of A, B and W can be derived analytically from looking at when the solutions to equations 2.37 and 2.39 become degenerate. This occurs when

$$27(A+B)^4 = 16A^2B^2(1 + AB/W^2) + 8(8W^2 + 9AB)(A+B)^2. \tag{2.40}$$

Again recalling that in the presence of charge-conjugation symmetry ($\mathcal{CPT}$) solutions appear in either imaginary or complex-conjugate pairs, a second spectral phase transition accompanied by an exceptional point creates the second phase boundary. This phase boundary joins pairs of imaginary eigenvalues, corresponding to at least one propagating factor being unphysical $|\lambda_i^{\pm}| < 1$, to the physical, complex conjugate pairs of solutions.

The analytical form, found by considering when imaginary solutions become degenerate, occur when

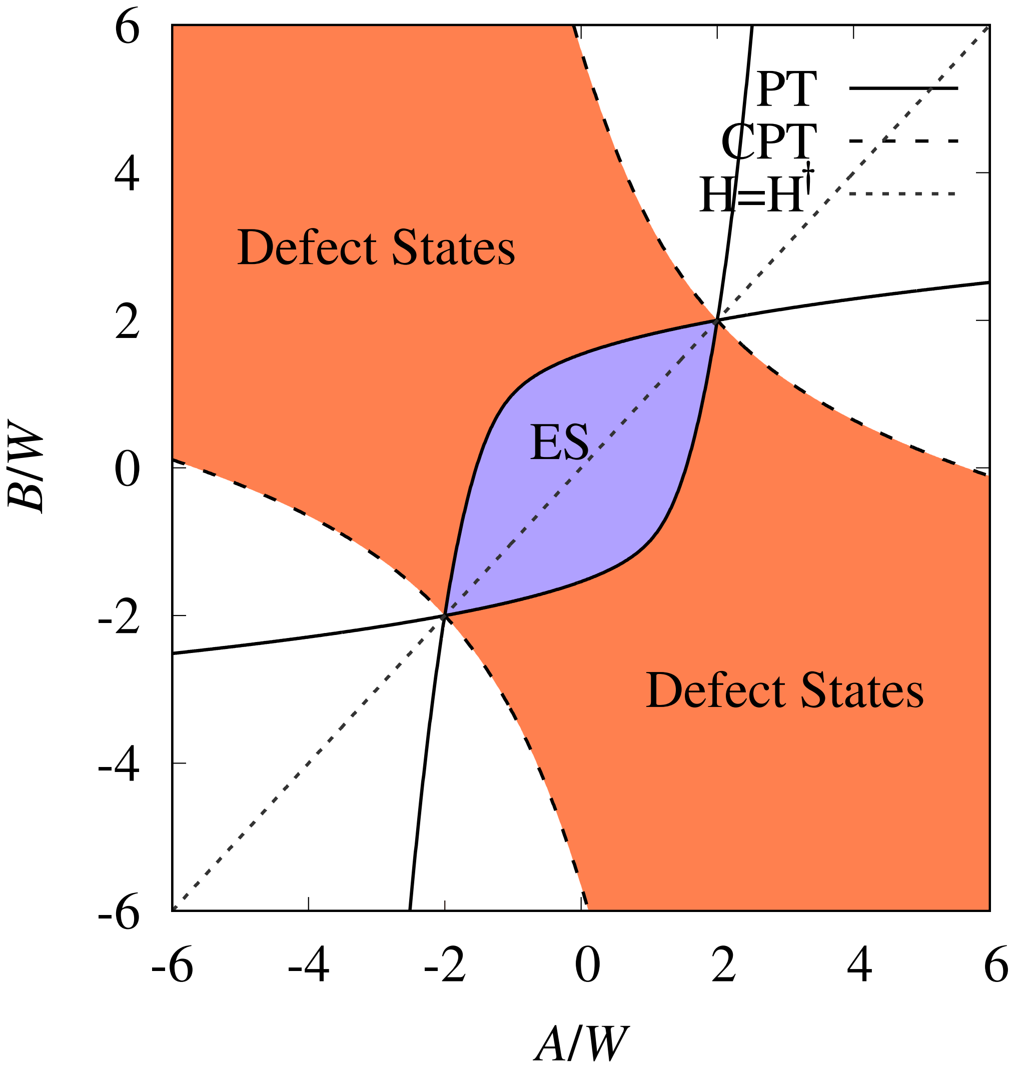

Figure 2.2: Phase diagram indicating the existence of defect states and their extended state (ES) precursors, bounded by the $\mathcal{PT}$ and $\mathcal{CPT}$-symmetry lines. The Hermitian line $H = H^\dagger$ is included to demonstrate that defect states only exist for open boundary conditions.

$$A^2 + B^2 + 6AB = 32W^2. \tag{2.41}$$

The defect states, bounded by these two phase transitions, has been mapped out in figure 2.2, where the backscattering amplitudes have been rescaled by the inter-resonator coupling.

2.1.3 Finite-size effects

To illustrate robustness of the defect states and the $\mathcal{PT}$ and $\mathcal{CPT}$ transitions, I extend the discussion into finite systems. Before I consider the robustness of the defect states I consider the effects of a finite chain to see what role finite-size effects have on the defect states and the transitions.

First I consider numerical simulations of a chain of 300 coupled resonators. Starting from the Hermitian line $A/W = B/W = 1$ in figure 2.2 and looking at the interval $1 < B < 4.5$, a cut is performed through all three phases. As discussed in the previous section solutions to the defect state equation must start in pairs on the real axis, bifurcate becoming complex after crossing the $\mathcal{PT}$ phase transition and finally meet again becoming imaginary after crossing the $\mathcal{CPT}$ phase transition. The remaining eigenvalues not corresponding to the defect states and not shown here remain either pinned to the real axis or to the imaginary axis and additionally a band gap is not required for the defect states to be present. The defect solutions are not pinned to a specific energy for example at zero energy as dictated by the charge-conjugation symmetry in the SSH model, presented in the introduction 1.3.2, but instead confined to the complex plane. Additionally since these states vanish in the presence of the defect and edge-modes cannot be found, this represents a deportation from the expected behaviour of topological states given by Hermitian systems.

The phase transitions of the defect states can be identified by divergences in the Petermann factor

$$K = \frac{\langle L|L\rangle\langle R|R\rangle}{|\langle L|R\rangle|^2} \tag{2.42}$$

which measures the non-orthogonality of the defect-state wavefunction given by the left $\langle L|$ and right $|R\rangle$ eigenvectors. This quantity diverges at exceptional points where the non-orthogonality is largest [87]. The Petermann factor also quantifies the sensitivity to general perturbations [88], including quantum noise [89, 90].

For the numerical simulation the defect state is selected according to the criteria that it is the most localised state. This can be determined by the inverse participation ratio (IPR)

$$\Gamma = \sum_n (|a_n^4| + |b_n|^4). \tag{2.43}$$

If the wavefunction is localised over a few resonators Γ is large, if it spreads out like for example an extended state, Γ will be comparatively small. Tracking the defect state over the interval, one of the four defect frequencies is shown in the central panel of figure 2.3. The black squares indicate 8 highlighted, distinct localisations which all occur within the defect region. Panel a) represents an extended state solution to the defect equations. As a precursor state this state weakly resembles a defect state. Since mode competition is high in this region the Petermann factor and IPR are erratic in this portion of the interval around the first black marker shown in figure 2.4. This first black markers corresponds to the upper most black marker of the middle panel of figure 2.3 and also panel a) of the same figure.

The clockwise pattern of black markers in central panel of figure 2.3 correspond to panels a)-h) and the same markers given in figure 2.4 form left to right. Cross referencing panels b) through to g) with figure 2.4 demonstrates how the defect initially has a rapid increase in the IPR due to narrowing of the defect state when B lies within the defect state region. The two largest peaks of the Petermann factor indicate the two phase transitions. The second marker corresponding to panel b) depicts the state just as the eigenvalues begin to depart from the real axis. The erratic behaviour of both the IPR and the Petermann factor before this transition occurs due to finite size effects and large mode competition from the extended states. Many shorter sharper peaks can be seen in the Petermann

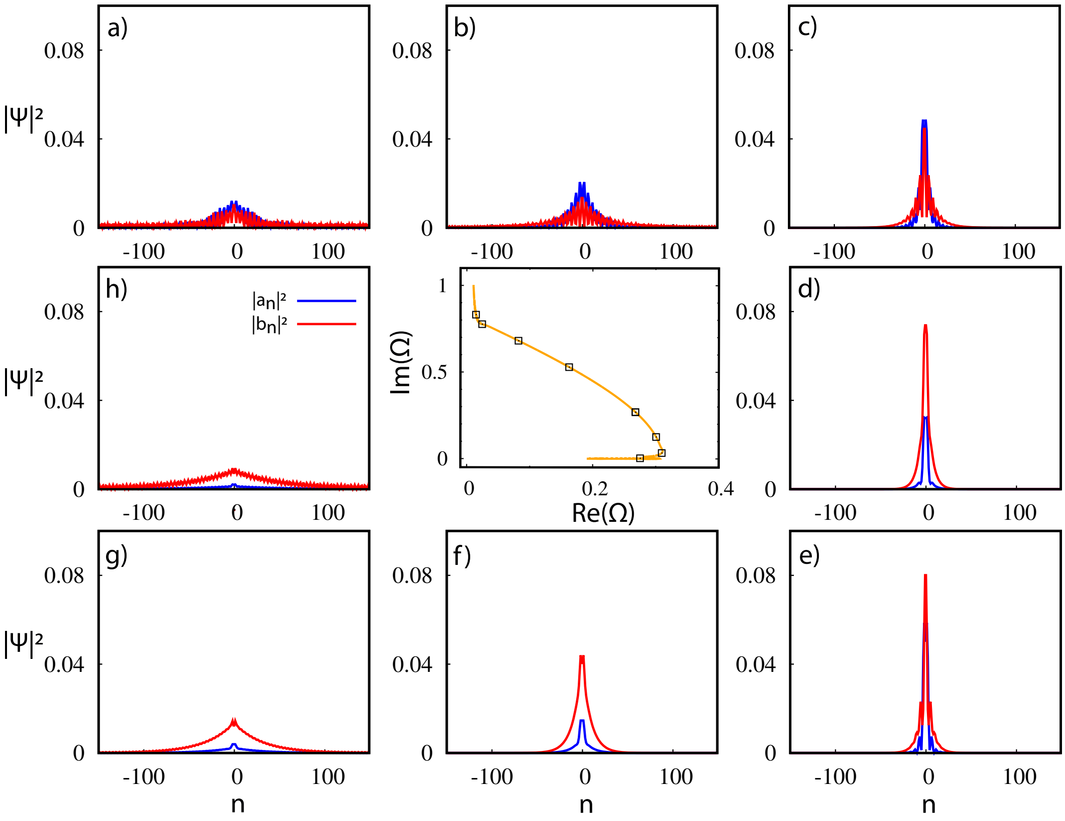

Figure 2.3: The central panel shows the trajectory of one of the four eigenvalues associated with the defect states from the upper right quadrant of the complex plane for the interval $1 < B < 4.5$, $A = W = 1$ (the other 3 quadrants are mirror images of the central panel). Panels labelled a)-h) give examples of the corresponding defect states and their precursors for eigenvalues marked by the black squares (following the trajectory anti-clockwise from the bottom) in the central panel. Each mode profile consists of two intensities $|a_n|^2$ of the CW component in the left half of the chain and the CCW component in the right half of the chain and $|b_n|^2$ of the CCW component in the left half of the chain and the CW component in the right half of the chain. Panels a)-h) contain parameters as follows: A=W=1, B= a) 1.5, b) 1.8, c) 1.85, d) 2.0, e) 2.5, f) 2.9, g) 3.2 and h) 3.5.

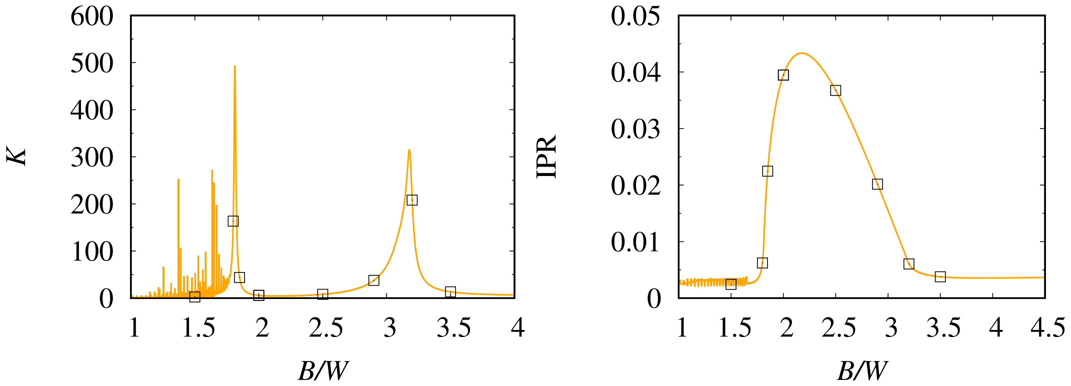

Figure 2.4: (Left panel) Divergences in the Petermann factor indicate spectral degeneracies in both the extended state phase and the two large broad peeks which indicate the $\mathcal{PT}$ and $\mathcal{CPT}$ phase transitions. (Right panel) Inverse participation ratio which grows large over the defect state phase. Both panels are produce for the same interval as that shown in figure 2.3, where the black markers are labelled in the same order as given in the caption.

factor before the broad phase transition peaks due to non-defects encountering spectral degeneracies. Again due to finite size effects the Petermann factor does not diverge. The clear smooth increase in IPR provides a reliable mechanism to track the defect state across the defect state region, until the IPR drops back to values comparable to extended states.

The wave-matching model indicates that after the $\mathcal{CPT}$ transition the defect state becomes non-normalisable and hence unphysical. However, in the fixed size finite system the exact degeneracy on the imaginary axis is avoided and defect solutions move parallel to the imaginary axis away from the origin. This avoidance is connected to the hybridisation of the defect state with an extended state, which occurs as soon as the decay length becomes comparable to the system size as shown in panel h).

2.1.4 Testing robustness

I test the robustness of the defect states using two approaches. I first consider a chain where the left-right symmetry is broken. This means parameterising each half of the chain differently without loss of the defect states. To illustrate this in

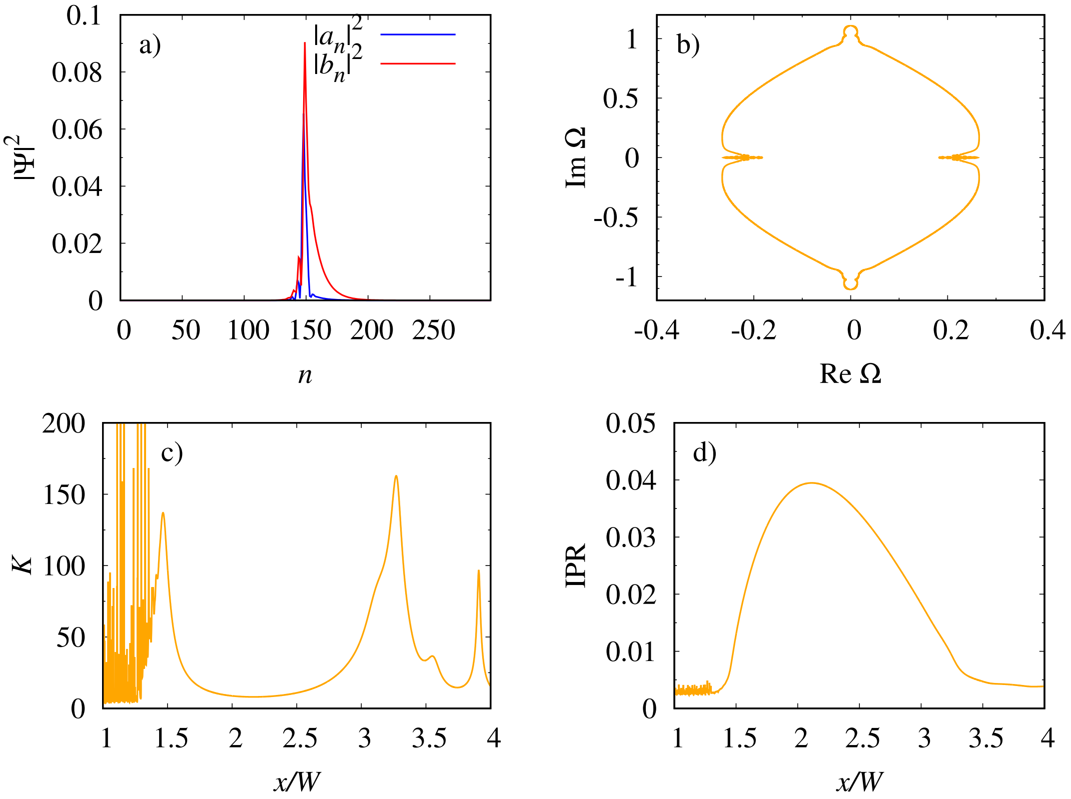

Figure 2.5: Asymmetric chain: a) Example of a defect state for couplings $A = W$, $B = 2W$ in the left half and $A = 0.5W$, $B = 2.5W$ in the right half of the chain. The remaining 3 panels are given by the parameters $A = W$, $B = x$ on the left half of the chain and $A = 0.5W$, $B = 0.5W + x$ on the right half: b) Trajectories of the eigenvalues associated with the defect states and their predecessors. c) Petermann factor of the defect states and predecessors. d) Inverse participation ratio of the defect states and predecessors.

the finite system over a wide range of parameters, consider the couplings $A = W$ and $B = x$ on the left side of the chain and $A = 0.5W$, $B = 0.5W + x$ on the right hand side of the chain, where x is given by the interval $1 < x < 4.5$.

A typical defect state within this interval is now highly asymmetric with two different decay rates on either side of the interface as shown in panel a) of figure 2.5. Following the trajectory of all 4 defect states, panel b) of the same figure shows the same departure of the pairs of solutions from the real axis into the complex plane and back towards the imaginary axis, where again hybridisation initially avoids the degeneracy until the IPR fails to track the defect state due to increased mode competition given by the weaker decay rate in one half of the chain. The transitions themselves are again reflected in the broad peaks of the

Petermann factor in panel c) and the largely increased IPR over the defect state region in panel d). Since both halves of the chain must have parameters that lie within the defect state region to exhibit defect states, broadening of the $\mathcal{PT}$ phase transition occurs. The asymmetric scenario also leads to a slight shift in the $\mathcal{PT}$ transition compared to the symmetric case given in figures 2.3 and 2.4 as on the left side of the chain A has been reduced.

Finally, in addition to asymmetry the topological nature of these defect states can be tested by introducing disorder and breaking translational invariance across the chain. This is calculated by drawing perturbations to A and B from the uniform distribution $y \in [-0.1W, 0.1W]$ on top of the parameters given in figure 2.5 for each individual resonator. Three different disorder realisations are presented in figure 2.6. Panel b) shows that the eigenvalues of the defect states still emerge from the real axis, their trajectories can be followed through the complex plane towards the imaginary axis. From panel c) it is difficult to directly infer from the peaks of the Petermann factor alone where the phase transitions are. This is because disorder induced Anderson localisation provides increased mode competition against the precursor states, which have a larger IPR than the extended states. However, the smooth increase of the IPR inside the defect state region shows both the presence of and the further shift to the $\mathcal{PT}$ and $\mathcal{CPT}$ phase transitions for all three disorder realisations. At this weak level of disorder the defect region is strikingly robust, demonstrating that these defects are indeed of a topological nature.

If disorder, induced by growth differences in the spacing between resonators, is of the same size as discussed in figure 2.6 is introduced to the inter-resonator couplings instead of the backscattering couplings, I would expect to see similar results. This is because the effects of disorder on topological states are usually most prominent when they force the bulk band gap to close and hence the topological phase is lost. Since this system does not rely on there being a bulk band gap it should remain relatively unaffected. Disorder typically creates many fractioned,

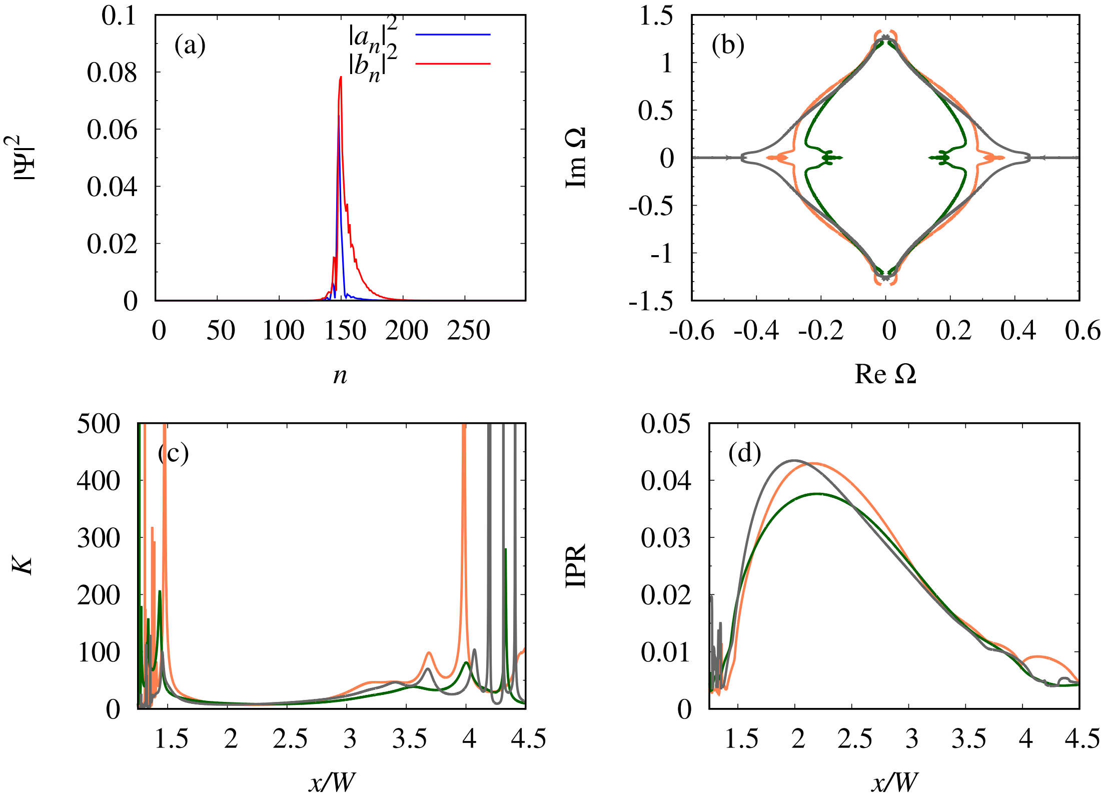

Figure 2.6: The same as given in figure 2.5, except now the backscattering amplitudes A and B have been perturbed by drawing from the uniform distribution $y \in [-0.1W, 0.1W]$ for three different disorder realisations. Panel a) shows an example of a defect state for one of the disorder realisations for the same parameters give in panel a) of figure 2.5 plus the additional perturbation.

weakly connected subsystems, where bulk modes are contained within small spatially isolated parts of the lattice. This may effect the width of the defect state only when it is not already localised. This will therefore slightly shrink the size of the defect region in the phase diagram. Most prominently disorder effects will be seen in the position of the divergences of the peterman factor and the increased competition of the IPR around the phase transitions.

2.2 Conclusion

In general optical systems are open due to radiative leakage or intrinsic gain and loss. The resulting non-Hermitian effects are often minimise for the purpose of experiments, where the principle goal was to find topological photonic analogues of electronic systems. With the more general case being non-Hermitian systems, in this chapter I have explored how open chains of coupled resonators can exhibit unique spectral features and host topological defect states pinned to an interface.

The key finding of this work is the generation of non-Hermitian topological states in a system which has a trivial Hermitian limit, where I demonstrated that the localised exponentially decaying states are insensitive to disorder. I showed that the localised states can be derived from the wave-matching conditions and identified the three phases of the associated solutions. Solutions may either come in real pairs where they correspond to scattering states, complex conjugate pairs where they represent defect states, or imaginary pairs which represent unphysical solutions. Each phase is separated by an exceptional point and the defect states emerge from the continuum of states to become spectrally isolated, an important feature for both the lifetime of the states and for experimentally exciting only these resonances. Furthermore, I have also showed that the exceptional point transitions of the defect states are symmetry driven by $\mathcal{PT}$ and $\mathcal{CPT}$ symmetries. I demonstrated insensitivity to asymmetry and disorder for both the spectral transitions and the defect states. In relation to the Hermitian classification this poses the important question of whether such states can be understood via a suitable extension of the conventional classification of Hermitian system.

The conventional methodology for categorising one-dimensional systems, such as that described in section 1.3.2, is to calculate winding numbers, the bulk property which determines the bulk-boundary correspondence. One such equivalent method is to calculate the pseudospin vector, $\sigma = (\langle\sigma_x\rangle, \langle\sigma_y\rangle, \langle\sigma_z\rangle)$, of the bulk Bloch modes as conducted in reference [22] for a non-Hermitian system. However similarly to the method discussed in 1.3.2 this requires the pseudospin vector to be confined to a plane due to $\sigma_z = 0$. In the resonator setting this is not the case.

These findings have motivated intense research into the bulk-boundary correspondence in non-Hermitian systems, seen as a critical linchpin in the Hermitian classification [91]. Calculations of winding numbers for non-Hermitian systems with well defined topological states in the Hermitian limit obey bulk-boundary correspondence holds [30]. The so-called anomalous protected edge and interface states such as those discussed here emerge from exceptional points. In the anomalous case it is still not clear whether bulk-boundary correspondence holds which has been further put to the test but more complex bulk phenomena in 2D systems, as I will discuss in the next chapter. It has also been suggest that these anomalous states are symmetry protected continuum bound states, following from the discussion of zero-energy bound states here [92].

It has been shown that for systems with chiral symmetry, bulk properties require two winding numbers to fully categorise them. One number belongs to the chirality of the mode and hence the sign of the Berry curvature and the other corresponds to the chirality of the exceptional point [30, 67, 93, 94]. The same authors also have recently suggested that the resonator chain discussed in this chapter, for the parameters $A = -B$, this belongs to a coupled ladder chain, made up from two complex SSH (cSSH) chains, where the SSH chain is given a staggered gain and loss on-site potential [95]. An interesting avenue of future work would be to see if the well defined winding numbers of the cSSH chains could be used to find a bulk invariant for this system.

Chapter 3

Bulk and Edge Fermi Arcs in Coupled Resonator Arrays

Spectral singularities behave like magnetic monopoles in that they are a source of topological charge in momentum space. Whilst the discussion in the introduction focused on these singularities as a signature of topological phase transitions, where the phases either side of the transition are gapped insulating phases, the discussion would not be complete without the inclusion of semimetals. In three-dimensions diabolic points occur in Weyl and Dirac semimetals [96, 97]. Weyl semimetals can be realised by either breaking time-reversal symmetry or parity-symmetry in Dirac semimetals where the degeneracy of two spin degenerate bands is lifted [98]. Pairs of Weyl points separated in momentum space then act as sources of Berry flux with opposite chirality and must be created and destroyed in pairs of opposite chirality. A particularly intriguing phenomenon observed in such systems is the formation of gapless surface-state Fermi arcs, corresponding to dispersive branches on the surface which connect topologically distinct parts of the bulk bands and are hinged to these spectral singularities [99, 100].

In optical systems, Hermitian Fermi arcs have been realised in metamaterials [101] and laser-written waveguides [102]. This provides again a springboard to explore non-Hermitian counterparts. Since optical systems don't intrinsically possess spin, other degrees of freedom can be used to engineer artificial gauge fields in acoustic structures to create Weyl points such as coupled waveguides [103] and stacking of dimerized chains in three dimensions [104]. In non-Hermitian systems exceptional points occur generically when only two parameters are varied [87], while a non-Hermitian perturbation of a diabolic point in three dimensions results in a one-dimensional exceptional curve [105]. Incorporating loss into a two-dimensional topological system with a diabolic point therefore results in the formation of two exceptional points connected by a bulk Fermi arc, a scenario that has been realised in a periodic photonic crystal [106]. Non-Hermiticity can also close the band gap in the bulk of a system, resulting in the formation of exceptional points and curves in momentum space that spawn complex branches in the bulk dispersion [107,108]. Furthermore, the $\mathcal{PT}$-symmetric edge states branching off conventional edge states [35] have been found to survive when the gap is closed.

These complex spectral bulk and edge effects in gapless topological systems are the focus of this chapter, where I show that analogous effects can also be achieved in 2D arrays of coupled resonators where the hermitian limit is topologically trivial. In the same vein as chapter 2, I again consider resonators that are slightly deformed from the circular geometry, which induce non-Hermitian losses in the form of leakage through the boundaries. Here I consider two symmetry classes, class AIII the chiral class where time reversal symmetry is broken, and class BDI the chiral class where time reversal symmetry is present. In two dimensions both of these classes are topologically trivial. I will demonstrate the existence of bulk Fermi arcs joining exceptional points in the Brillouin zone for class AIII and the formation of edge states in both classes.

3.1 2D array

The wave equation for a one-dimensional chain of coupled resonators was given in equation (2.11) of chapter 2. I now consider a two-dimensional array of coupled resonators as depicted in panel (a) of figure 3.1 with corresponding wave equation

$$\omega_{n,m}\psi_{n,m} = H_{n,m}\psi_{n,m} + T_x(\psi_{n+1,m} + \psi_{n-1,m}) + T_y(\psi_{n,m+1} + \psi_{n,m-1}), \qquad (3.1)$$

where

$$T_x = \begin{pmatrix} 0 & W_x \\ W_x & 0 \end{pmatrix}, \quad T_y = \begin{pmatrix} 0 & W_y \\ W_y & 0 \end{pmatrix}. \qquad (3.2)$$

Solutions to equation (3.1) are of the form $\psi_{n,m} = e^{ik_x n + ik_y m}(a_{n,m}, b_{n,m})^T$. Plugging this solution back into (3.1) generates the Bloch Hamiltonian

$$H(\mathbf{k}) = \begin{pmatrix} \Omega_0 & A + 2W_xC_x + 2W_yC_y \\ B + 2W_xC_x + 2W_yC_y & \Omega_0 \end{pmatrix}, \qquad (3.3)$$

where $\mathbf{k} = (k_x, k_y)^T$, $C_x = \cos k_x$ and $C_y = \cos k_y$. The dispersion of this Hamiltonian is $\omega_\pm(\mathbf{k}) = \omega_0 \pm \Omega_\pm(\mathbf{k})$ where

$$\Omega_\pm = \pm\sqrt{(A + 2W_xC_x + 2W_yC_y)(B + 2W_xC_x + 2W_yC_y)}. \qquad (3.4)$$

Since we have only added an extra dimension to the model studied in the previous chapter, the same symmetries are still present. Here, I also consider the case where the parameters A, B, W_x and W_y can be complex and hence break time-reversal symmetry. For the case of complex parameters, since the chiral symmetry mapping Ω_+ to Ω_- is still present, the model falls into the symmetry class AIII, which is trivial in two dimensions.

3.1.1 Bulk Arcs

As shown in the examples of figure 3.1(b-d), representative band structures in this class AIII combine regions with predominantly real and predominantly imaginary resonance frequencies. In all cases, one can clearly make out bulk Fermi arcs with $\mathrm{Re}\,\Omega_\pm = 0$. These arcs emanate from exceptional points, which arise when

$$A + 2W_xC_x + 2W_yC_y = 0 \quad \text{or} \tag{3.5a}$$

$$B + 2W_xC_x + 2W_yC_y = 0. \tag{3.5b}$$

Each of these conditions can be met by varying two real parameters (k_x and k_y), so that the EPs appear generically at isolated positions in the two-dimensional Brillouin zone. The arcs can occur on their own (panel b and e) or be complemented by closed Fermi lines (panel d and f). The topology of these lines and arcs can change at parameters for which they intersect (panel c), which occurs when an arc crosses a stationary point, i.e. when $\partial_{k_x+ik_y}\Omega_\pm|_{k_x-ik_y} = 0$ or $\partial_{k_x-ik_y}\Omega_\pm|_{k_x+ik_y} = 0$. Additional Fermi arcs occur when the inter-resonator couplings take on $\mathcal{PT}$-symmetric values, as shown in panels e and f.

Tuning the array further such that the parameters are all real returns us to the $\mathcal{PT}$ symmetric case, where real values of W_x and W_y are realised when the evanescent coupling is lossless [109]. To obtain real but distinct values of A and B, only a single parameter needs to be tuned [110]. In the symmetry classification of Hermitian topological systems, the case of real couplings represents the chiral class BDI with a conventional time-reversal symmetry where here the non-Hermitian

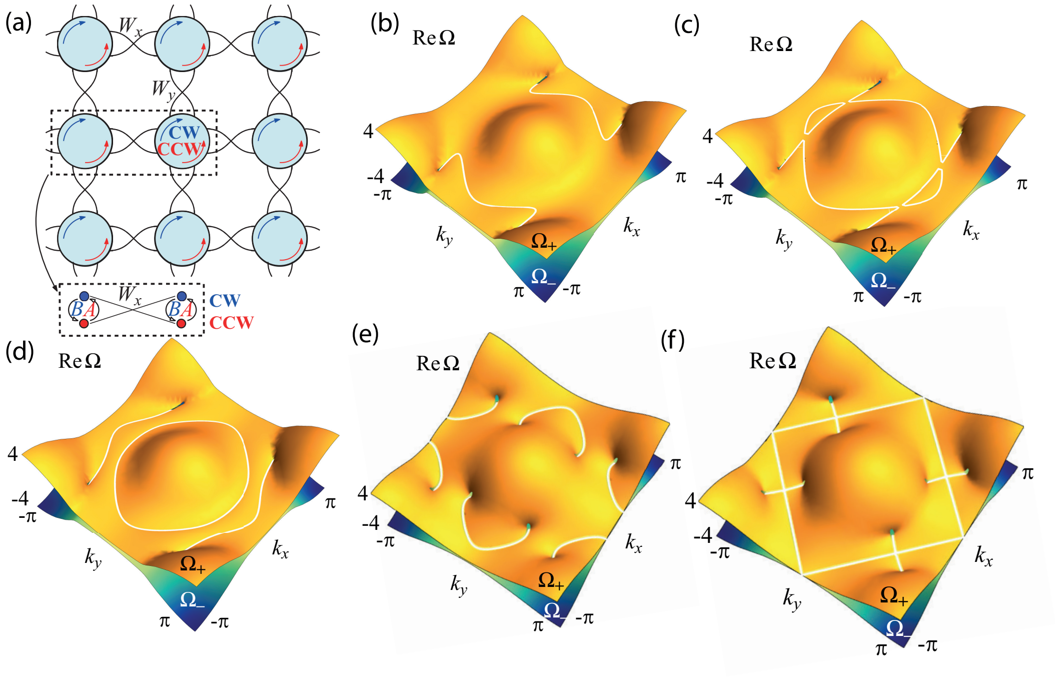

Figure 3.1: Bulk Fermi arcs in a two dimensional array of evanescently coupled non-hermitian resonators. (a) Each resonator supports a clockwise (CW) and a counter-clockwise (CCW) internal mode that are coupled by asymmetric backscattering amplitudes A and B, as obtained, e.g., from a small non-spherical deformation of open dielectric resonators. The resonators are placed on a square lattice and are coupled evanescently with coupling coefficients W_x and W_y that convert CW waves into CCW waves. This coupling configuration introduces a chiral symmetry into this non-hermitian system.(b-d) Real part $\mathrm{Re}\,\Omega$ of the bulk dispersion for $B = -2.5 + 0.2i$, $W_x = 1.0 + 0.1i$, $W_y = 1.0 + 0.5i$, and the three values $A = 1.5 + 0.1i$ (b), $A = 1.5 + 0.2i$ (c) and $A = 1.5 + 0.3i$ (d). In each case, the dispersion consists of two sheets Ω_+ (yellow surface) and $\Omega_- = -\Omega_+$ (blue surface) that are related by the chiral symmetry. The white lines indicate Fermi arcs and lines with $\mathrm{Re}\,\Omega = 0$, corresponding to intersections of the two sheets. The arcs terminate at exceptional points (EPs), which are the non-hermitian counterparts of Weyl points in topological insulators. In (b), four EPs are connected by two arcs. In (d), the EPs are reconnected by two arcs with a different topology, while a closed Fermi line is also present. Panel (c) shows the reconnection point between these two scenarios, which is mediated by two smaller closed Fermi lines. Bulk dispersions are also shown for $B = -1.5 - 0.2i, A = 1.5 + 0.2i, W_x = 1.0 - 0.5i$ and $W_y = 1.0 + 0.5i$ for panel e) and $B = -2.5 + 0.2i, A = 1.5 + 0.2i, W_x = 1.0 - 0.3i$ and $W_y = 1.0 + 0.3i$ for panel f). Balancing the gain and loss of W_x and W_y creates additional exceptional points for the Fermi-arcs to connect between.

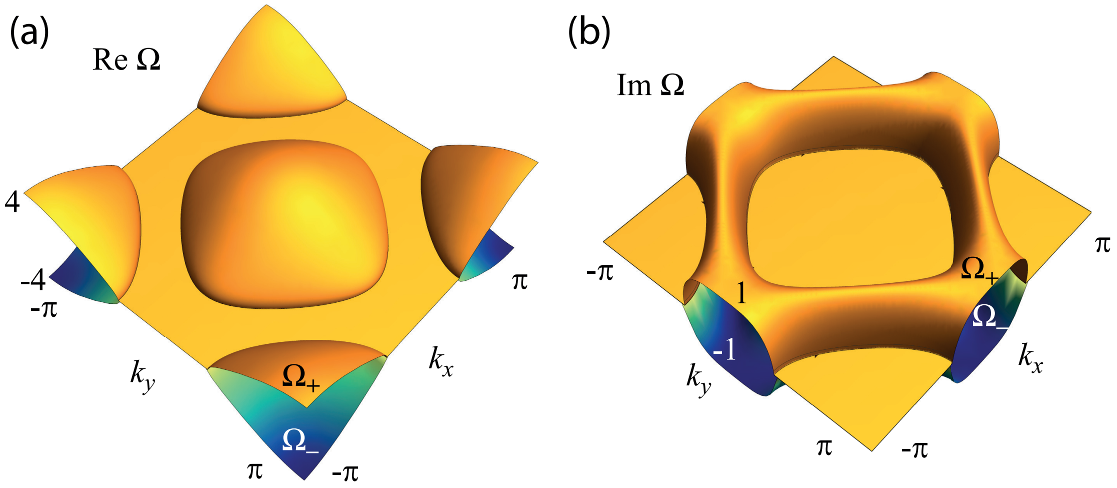

Figure 3.2: (a) Real and (b) imaginary parts of the bulk dispersion for $A = 1.0$, $B = -1.0$ and $W_x = W_y = 1$, representing the $\mathcal{PT}$-symmetric case (symmetry class BDI) where the band structure displays purely real and imaginary branches, and the exceptional points degenerate into lines.

time reversal symmetry is given by $(\mathcal{PT})^2 = 1$, which for two-dimensional systems is again topologically trivial.

In this subsection, unless specified, I consider A, B, W_x and W_y to be real. Under these conditions the band structure of equation (3.4) the resonator array is real and gapped if $|A|, |B| > 2(W_x + W_y)$ and $AB > 0$, or imaginary and gapped if for the same conditions $AB < 0$. In all other cases, the dispersion contains purely real and purely imaginary branches in ranges of k_x and k_y. These branches are joined at lines of EPs with $\Omega_\pm = 0$, which are again determined by the equation (3.5).

An example of a band structures in symmetry class BDI is shown in figure 3.2. The purely imaginary branches define flat patches with $\mathrm{Re}\,\Omega_\pm = 0$, which are bounded by lines of exceptional points. The Fermi arcs in symmetry class AIII can be interpreted as remnants of these regions when the $\mathcal{PT}$-symmetry is explicitly broken and values of the couplings become complex.

3.1.2 Interfaces and extending the wave matching

Following the same prescription laid out in the chapter 2, I extend the notion of a point interface into an edge interface, to induce edge states. Again the interface separates two regions of opposite deformations of the resonators as depicted in figure 3.3 panel (a). This time the interface is placed along the y-axis, where within the configuration for $n < 0$ (depicted in blue) resonators have backscattering A and B, whilst for $n \geq 0$ (depicted in green) resonators have the values of A and B swapped.

In figure 3.3, panel (b) shows an example of a numerically obtained edge state in an array of 40×40 resonators with parameters $A = -2$, $B = 2$, $W_x = W_y = 1$, demonstrating that such states can indeed be formed. The states are exponentially confined in the direction away from the interface, and display a standing-wave pattern along the interface as the y-direction is only dependent on the quantisation conditions.

This simple dependence in the y-direction allows for separation of the variables according to $\boldsymbol{\psi}_{n,m} = \boldsymbol{\varphi}_n e^{ik_y m}$, where the permitted values of k_y are determined by the width of the array.

The wave equation (3.1) then takes the form

$$\Omega\boldsymbol{\varphi}_n = h_n\boldsymbol{\varphi}_n + t_x(\boldsymbol{\varphi}_{n+1} + \boldsymbol{\varphi}_{n-1}), \tag{3.6}$$

where

$$h_n = \begin{cases} \begin{pmatrix} 0 & A' \\ B' & 0 \end{pmatrix} & (n < 0) \\ \begin{pmatrix} 0 & B' \\ A' & 0 \end{pmatrix} & (n \geq 0) \end{cases}, \tag{3.7}$$

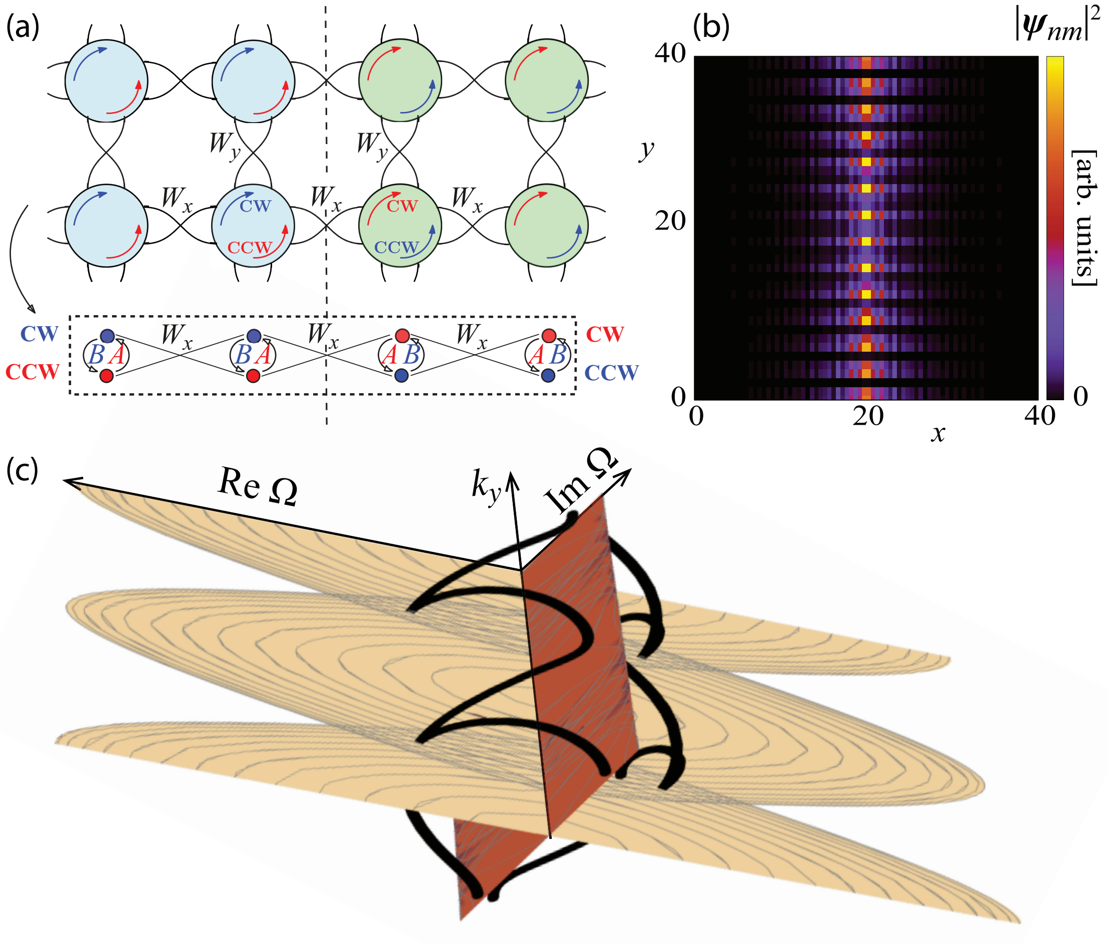

Figure 3.3: Edge-state arcs in an array with an interface joining resonator arrays with opposite backscattering. (a) Horizontal slice through the array, where the dotted line indicates the interface between resonators with backscattering amplitudes A and B as in figure 3.1 (blue resonators to the left), and resonators where the values of these backscattering amplitudes are interchanged (green resonators to the right). (b) Density plot of the intensity of a representative edge state in a finite square array of 40×40 resonators, with $A = -B = W_x = W_y$. (c) Quasi-one dimensional band structure in the infinite version of this array, where k_y is a good quantum number. In this representation, the bulk bands form sheets, which here lie in the real and imaginary plane as all parameters are real ($\mathcal{PT}$-symmetric symmetry class BDI, see figure 3.2). The black curves are the edge-state arcs, which connect the different sheets.

with the effective coupling coefficients

$$A' = A + 2W_y \cos k_y, \tag{3.8a}$$

$$B' = B + 2W_y \cos k_y. \tag{3.8b}$$

For fixed parameters A', B', equations (3.6) and (3.7) define a quasi-one-dimensional set of coupled-mode equations, which for $k_y = \pi/2$ recovers the case of defect states found in the previous chapter. Additionally, the wave matching calculation performed in the chapter 2 also holds for this quasi-1D parameterisation. The equations determining the symmetric and antisymmetric edge states are

$$\Omega(\Omega - 2W_x)^2 - A^{'}B^{'}\Omega + (A^{'} - B^{'})^2\frac{W_x}{2} = 0 \tag{3.9a}$$

$$-\Omega(\Omega + 2W_x)^2 - A^{'}B^{'}\Omega + (A^{'} - B^{'})^2\frac{W_x}{2} = 0. \tag{3.9b}$$

For convenience this can be re-parameterised as follow: using the scaled frequencies

$$\omega = \frac{\Omega}{W_x} \tag{3.10}$$

and the effective parameters

$$\mathcal{A} = \frac{A + B + 4W_y \cos k_y}{2W_x} \qquad \text{(arc parameter)}, \tag{3.11a}$$

$$\mathcal{B} = \frac{A - B}{2W_x} \qquad \text{(backscattering asymmetry)}, \tag{3.11b}$$

edge states with a symmetric or antisymmetric mode profile about the interface then obey the equations

$$-\omega\mathcal{A}^2 + (2+\omega)\mathcal{B}^2 + \omega(2-\omega)^2 = 0, \tag{3.12a}$$

$$\omega\mathcal{A}^2 + (2-\omega)\mathcal{B}^2 - \omega(2+\omega)^2 = 0., \tag{3.12b}$$

respectively.

The symmetric and antisymmetric solutions to these equation are connected by chiral symmetry, thus remain paired as ω and $-\omega$ even when all parameters are complex. In the $\mathcal{PT}$-symmetric case where the parameters A, B, W_x and W_y are real, the solutions of equations (3.12a) and (3.12b) are further constrained to be real or to occur in complex-conjugated pairs, leading to quadruplets $(\omega, -\omega, \omega^*, -\omega^*)$.

Again to ensure the solutions to these equations belong to physical, non-scattering defect states I rewrite the consistency conditions from equations 2.31 and 2.38 in the previous chapter as

$$2 - \lambda_1\lambda_2 - \frac{1}{\lambda_1\lambda_2} = 2\omega, \tag{3.13a}$$

$$2 - \lambda_1\lambda_2 - \frac{1}{\lambda_1\lambda_2} = -2\omega, \tag{3.13b}$$

where the propagating factors are given by

$$\lambda_1 = C_1 \pm \sqrt{C_1^2 - 1}, \quad C_1 = -\frac{\mathcal{A}}{2} + \frac{\sqrt{\mathcal{B}^2 + \omega^2}}{2}, \tag{3.14a}$$

$$\lambda_2 = C_2 \pm \sqrt{C_2^2 - 1}, \quad C_2 = -\frac{\mathcal{A}}{2} - \frac{\sqrt{\mathcal{B}^2 + \omega^2}}{2}. \tag{3.14b}$$

The signs of the square roots have to be chosen such that $|\lambda_1| > 1$ and $|\lambda_2| > 1$. Propagating factors follow the same rules as in the 1D case, that being if for a solution of equation (3.12a) or (3.12b) a propagation factor is $|\lambda_l| = 1$, the solution belongs to a scattering state. If the consistency equations (3.13a) or (3.13b) can only be fulfilled by combining a decaying and an increasing propagation factor λ_l, the state cannot be normalized and is unphysical. Therefore, in both cases edge states change from physical to unphysical at points at which one of the propagation factors attains $|\lambda_l| = 1$. This corresponds to propagating waves in the bulk system, and therefore occurs when an edge-state arc meets the bulk dispersion relation, where it then terminates. In the $\mathcal{PT}$-symmetric case, the termination points coincide with degeneracies in edge-state quadruplets at real or imaginary frequencies, thus constituting exceptional points.

3.1.3 Phase diagram and edge states

The position of these exceptional points follows from the same procedure up to equation (2.40) and (2.41), except now mapped to the effective parameter space of $(\mathcal{A}, \mathcal{B})$;

$$\mathcal{A}^6 - \mathcal{B}^6 + \mathcal{B}^4 + \mathcal{A}^4(46 - 3\mathcal{B}^2) + \mathcal{A}^2(16 - 20\mathcal{B}^2 + 3\mathcal{B}^4) = 0 \tag{3.15a}$$

$$2\mathcal{A}^2 - \mathcal{B}^2 - 8 = 0. \tag{3.15b}$$

Panel (a) in figure 4.13 illustrates the traces of the edge-state arcs in the real section of effective parameter space. The solid and dashed curves in the diagram denote the locations of the real and imaginary bulk energy bands in this space given by equations (3.15a) and 3.15b, which confine solutions ω of equations (3.12a) and (3.12b) to the regions which represent genuine edge states (green region), scattering states (red) or non-normalizable unphysical states (blue). The edge

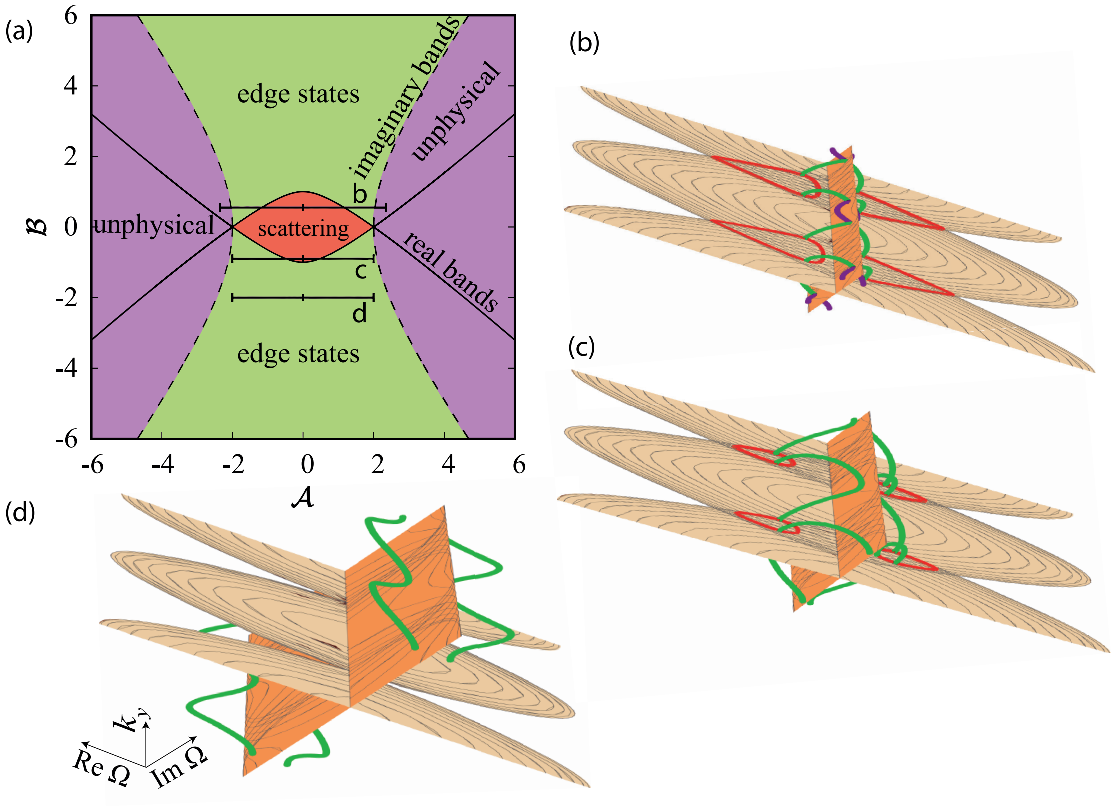

Figure 3.4: (a) Traces of the edge-state arcs in the real section of their effective parameter space $(\mathcal{A}, \mathcal{B})$ [defined in Eq. (3.11)]. The traces are horizontal lines of length $4W_y/W_x$, which are centred at $\mathcal{A} = (A + B)/2W_x$, $\mathcal{B} = (A - B)/2W_x$. The solid and dashed curves denote the termination conditions at the real and imaginary branches of the bulk bands, where the edge states (green region) turn into extended scattering states (red) or into non-normalizable, unphysical states (blue). The three representative traces correspond to the quasi-one-dimensional band structures shown in (b-d), where the edge-state arcs are indicated in green, while their scattering predecessors are given in red and unphysical states in blue. In (b), $A/W_x = 0.55$, $B/W_x = -0.55$, $W_y/W_x = 1.175$, for which the trace crosses both termination lines and the arcs connect the real and imaginary branches of the bulk bands. In (c), $A/W_x = -0.9$, $B/W_x = 0.9$, $W_y/W_x = 1$, for which the trace only reaches the real termination line so that the arcs loop back to the real branches. In (d), $A/W_x = -2.0$, $B/W_x = 2.0$, $W_y/W_x = 1$, for which the trace remains confined in the edge-state region so that the arc are free-standing.

states trace out a horizontal line $\mathcal{A}(k_y)$ in the arc parameter, which according to the definition in equation 3.11 has a length $4W_y/W_x$ determined by the coupling anisotropy, while its horizontal center is given by $\mathcal{A}(\pi/2) = (A+B)/2W_x$ and its vertical position given by the backscattering asymmetry parameter $\mathcal{B} = (A-B)/2W_x$.

The three labeled horizontal lines are the traces of edge states for representative systems with $A = -B$. In the complex energy dispersion these traces correspond to the arcs shown by the green curves in panels (b-d). These arcs can connect the real and imaginary branches of the bulk dispersion relation (b), can loop back to the real branch (c), or can be disconnected from the bulk bands (d). The blue arcs in panel (b) looping back to the imaginary branches represent unphysical states, arising in panel (a) from segments of the trace across the dashed line. The red arcs in panels (b,c) represent scattering states within the real branch of the bulk dispersion, which occur in panel (a) when the traces cross the corresponding solid line. The disconnected arcs as shown in panel (d) occur for traces that are confined to the interior of the edge-state region, so that they do not cross the phase boundaries defined by the bulk bands. Additionally, since the length of the horizontal lines in panel (a), given by the arc parameter, is $4W_y/W_x$, the amount of the branches which correspond to edge states can be controlled by the ratio of inter-resonator couplings W_x and W_y. The coupling strengths of these couplings are determined by the relative distances between the resonators in the x and y directions.

3.1.4 Breaking $\mathcal{PT}$-symmetry

Edge state arcs still persist when $\mathcal{PT}$-symmetry is broken by allowing the coupling parameters to become complex and the system has entered into the AIII symmetry class. To examine the qualitative behaviour of this symmetry breaking, panel (a) of figure 3.5 demonstrates that the edge states are still present for parameters

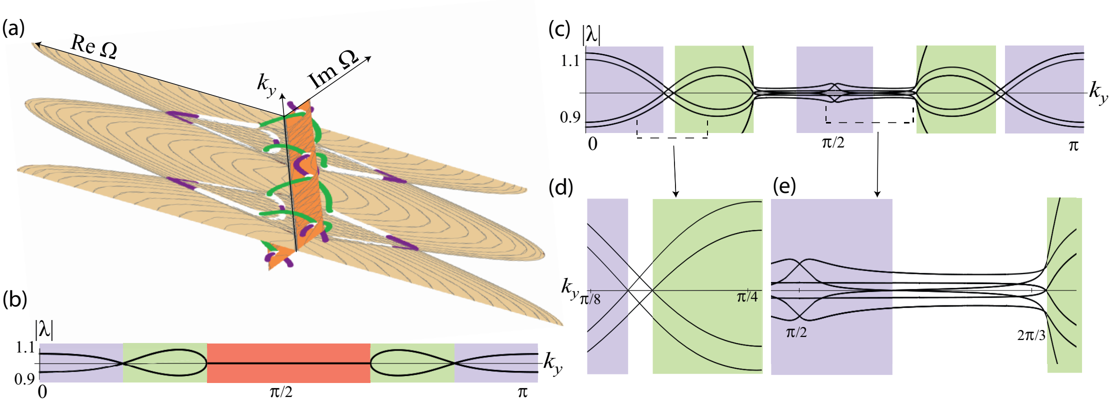

Figure 3.5: (a) Edge-state arcs for complex backscattering amplitudes $A/W_x = 0.55 + 0.02i$, $B/W_x = -0.55 + 0.02i$ and $W_y = 1.175$ [close to the real values in figure 4.13(b)]. All arcs still terminate on the bulk bands, which now no longer are real or imaginary. (b-d) Propagation factors $|\lambda_l|$, $1/|\lambda_l|$ of potential edge states as determined by equation 3.14. In (b), $A = -B = 0.55/W_x$, $W_y/W_x = 1.175$, corresponding to the real values of figure 4.13 panel (b). In (c,d), the parameters take the complex values given above. For complex parameters the region of scattering states is replaced by regions of physical and unphysical states. Furthermore, the termination points of different arcs now appear at separate values of k_y, as shown in detail in panels (d) and (e) which zoom into the termination region at the formerly purely imaginary and real branches of the bulk dispersion, respectively.

which are almost real and close to those used in panel (b) of figure 4.13. The arcs still emerge from the bulk dispersion, but the degeneracy of the termination points is lifted, which is particularly visible on the formerly real sheets. Panels (b) and (c) compare the propagation factors λ_l and $1/\lambda_1$ along the arc for real and complex couplings. This comparison reveals two distinct effects. The propagation factors of the former scattering states acquire moduli $|\lambda_1| \neq 1$ and hence turn into weakly confined edge states or non-normalizable, unphysical states. Furthermore, the formerly degenerate transitions at which edge states from previously symmetry-paired arcs become unphysical occur at independent values of k_y, as shown in panel (d) close to the formerly imaginary sheet and in panel (e) close to the formerly real sheet. All these features remain dictated by the general quantization conditions given in equations (3.12a) and (3.12b) subject to the consistency equations (3.13a) and (3.13b), which hold for general complex values of all coupling parameters.

3.2 Conclusion

In summary, in this chapter I have demonstrated an extension of one dimensional resonator chain to the the two-dimensional array of coupled resonators with non-Hermitian internal backscattering which is capable of displaying complex spectral phenomena in both the bulk and at interfaces. In doing so, I have shown that two of the universality classes in 2D display non-Hermitian topological phenomena, the chiral class AIII without time-reversal symmetry and the chiral class BDI with time-reversal symmetry, which are both trivial in the Hermitian limit.

In the bulk, for complex parameters which break $\mathcal{PT}$-symmetry (class AIII), I have shown that bulk arcs can be seen connecting pairs of exceptional points in different topologies, sometimes intersecting with Fermi surfaces. For real parameters when $\mathcal{PT}$-symmetry is restored (class BDI) these bulk arcs are replaced by flat sections of the band structure.

At an interface, by extending the wave matching into two dimensions, I showed that both symmetry classes contain edge arcs emanating from the bulk surfaces of the dispersion as a natural extension to the concept of edge states spanning across the bulk gap of a topological insulator. I also demonstrated that the range of these edge states over the full Brillouin zone can be achieved by adjusting the real space distances of the adjacent resonators.

From a practical perspective, these findings imply that nontrivial dispersion effects can be achieved without needing to resort to carefully engineered systems that replicate the intricate symmetries required for hermitian topological physics. Since reciprocity is preserved, the described effects can occur in conventional optical settings where the main requirement is chiral symmetry.

In such optical settings, bulk Fermi arcs are directly observable in momentum space [106]. Besides this characteristic spatial confinement, a key feature that distinguishes these states are their distinct life times. Therefore, an attractive approach to probe a system for edge-state arcs would be to excite a state locally near the interface, and observe the dynamical evolution of this state along the arc towards long life times. In this way, these resonator arrays provide promising mechanisms for state engineering.

Chapter 4

Nonlinear mode competition in topological laser arrays

Creating robust light transport when systems contain active optical elements is difficult to achieve. Considering passive systems alone, robust transport has been achieved in systems which display topological states such as the SSH model discussed in the introduction. Such topological interface states can often suffer from fabrication defects which accidentally close the gap or which easily mix and hybridise with Bloch states due to similar levels of density of states [111]. Since the topological states are localised onto only one of the sublattices one such method to spectrally isolate these states is to introduce a staggered complex potential to the dimerised lattice, where the sublattice which contains the topological state receives gain and the other sublattice receives loss [22]. The topological mode therefore makes optimum use of the gain provided. This model transforms the SSH model into a non-Hermitian $\mathcal{PT}$-symmetric lattice, where Bloch states spread between both sublattices and see both gain and loss. Non-Hermitian effects therefore play a vital role in affecting the comparative survival of topological interface states, making them less susceptible to fabrication errors and vital for topological mode selection.

Topological states also appear in active systems such as ultra-cold atomic gases [112], exciton-polaritons [113–115], acoustic waves [116] and lasers [41, 117]. Recently, experiments have realised topological zero-modes in polariton condensates [46, 118] and lasers [25, 26, 119]. As these systems are inherently non-linear, the question arises whether the notion of zero-modes and topological protection persists as non-linearities are indispensable to stabilise active systems at their working point. These non-linear systems share the commonality with fermionic systems, that their excitations come in the charge-conjugated pairs $\psi exp(-i\omega t), \chi\psi^* exp(i\omega t)$ at positive ω and negative $-\omega$ frequencies respectively, where χ represents the appropriate unitary transformation. Excitations of this form can be categorised by Bogoliubov theory. Topological protection persists when these spectral constraints are applied to the fermionic setting, for instance superconducting systems can feature Majorana zero-modes $\psi = \chi\psi^*$ at $\omega = 0$, and in weakly interacting bosonic systems with chiral edge states [120, 121], which sometimes acquire dynamic instabilities [122, 123].

In the first part of this chapter I demonstrate that topologically protected modes of the non-Hermitian SSH model naturally extend into the non-linear setting in the context of lasers. The first example uses the non-Hermitian SSH model to confirm the extension of zero-modes into the non-linear regime and the second example modifies the non-Hermitian SSH model to create zero-mode with a much larger mode volume. In exploring the operational regimes of the topologically protected laser modes I will show that the modes acquire topologically protected power oscillations at topological phase transitions, which have not yet been observed in the experiments outlined above. On first sight it would appear that nonlinearities should degrade the effectiveness of topological mode selection. Even when starting under ideal linear conditions, the nonlinearities induce spatially varying loss and gain, which depends on the intensity profile of the mode across the system. The resulting effective gain has the potential to disfavour the topological mode, in particular when its mode volume is small.

In the second part of this chapter I perform a stability analysis on the excitation spectrum by performing a linearisation around the working point, where the nonlinear modes reduce to those of the linear system in the linear limit. Topological states in linear systems are protected by symmetry, but their number can change discretely in phase transitions, which are generally linked to degeneracies (such as when a band gap closes). This notion is underpinned by the continuity of the spectrum under smooth parameter changes (deformations of the system), a feature of linear spectral analysis. I show that dynamical solutions to the time-dependent non linear wave equation are protected by symmetry and that the number of them can also change due to bifurcations with focus on the spectral modes which have no linear counterpart.

In the final part of this chapter I consider a series of different effects which effect both the mode volume of the topological states and test the robustness of the states to different kinds of disorder. I begin by introducing gain onto the sublattice without the defect states to show that by increasing the mode competition by exciting the other modes of the system large parts of parameter space behave like the ideal case. I also consider the increased mode competition in the second example, where the defect state region is extended to create a region of uniform coupling. Again I show that for a large part of parameter space the topological modes persist, but are now accompanied by additional solutions. Finally for both the first and second example, I subject the laser arrays to coupling disorders and onsite disorders and show that a degrading of the topological mode regimes requires strong disorder strengths, but now the modes are much less stable as signified by the linearised spectral analysis of the excitation spectra.

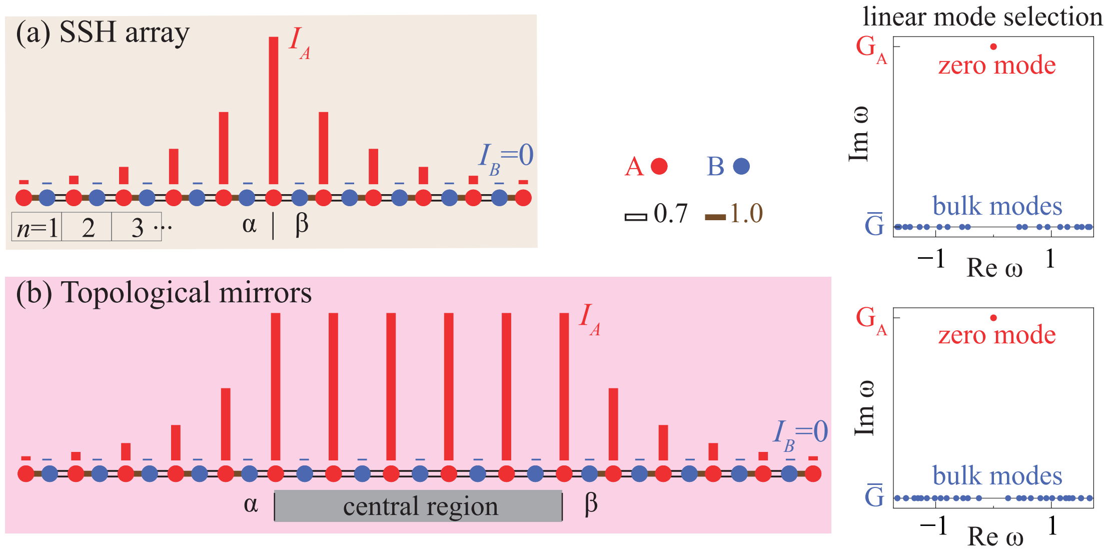

Figure 4.1: Topological mode selection in laser arrays consisting of single-mode resonators grouped in dimers (enumerated by n). The intra-dimer couplings κ and inter-dimer couplings κ' are chosen to produce interfaces between regions of topologically different band structures. (a) In the Su-Schrieffer-Heeger (SSH) model, the alternating couplings define a phase α ($\kappa > \kappa'$) and a phase β ($\kappa < \kappa'$). The displayed defect state arises from two consecutive weak couplings, forming an interface between the two phases. (b) The defect region can be extended, leading to a variant where the phases α and β function as selective mirrors that confine a defect state with a larger mode volume. In both cases, the resulting defect states have preferential weight on the A sublattice (red) and can be selected by distributed gain and loss. As illustrated in the right panels, in the linear regime the defect state acquires the effective gain G_A from the A sublattice, while the other modes acquire the average gain $\bar{G}$ in the system ($G_A = \bar{G} + 0.1$, $\kappa, \kappa' = 1, 0.7$). We demonstrate that this mode selection mechanism extends to the nonlinear conditions at the working point of a laser, where it stabilises robust zero modes and also enables alternative topological operation regimes with power oscillations.

4.1 Nonlinear topological laser arrays

4.1.1 Modelling laser arrays with saturable gain

The general design of the topological laser arrays studied in this work is shown in Fig. 4.1. The arrays can be interpreted as chains of identical single-mode resonators, denoted by dots, which are coupled evanescently to their nearest neighbours. Given this structure of the coupling it is convenient to divide the system into two alternating sublattices A and B, and group neighbouring pairs of A and B sites into dimers. Denoting the corresponding wave amplitudes on the nth dimer as A_n and B_n, their dynamical evolution is then governed by the coupled-mode equations

$$i\frac{dA_n}{dt} = [\omega_{A,n} + V_{A,n}(|A_n|^2)]A_n + \kappa_n B_n + \kappa'_n B_{n-1}, \tag{4.1a}$$

$$i\frac{dB_n}{dt} = [\omega_{B,n} + V_{B,n}(|B_n|^2)]B_n + \kappa_n A_n + \kappa'_{n+1} A_{n+1}, \tag{4.1b}$$

where $\omega_{s,n}$ $(s = A, B)$ are the bare resonance frequencies of the isolated resonators, κ_n is the intra-dimer coupling between the A and B site in the nth dimer, and κ'_n is the inter-dimer coupling between the B site in the $(n-1)$st dimer and the A site in the nth dimer. The effective complex potentials [124]

$$V_{A,n}(|A_n|^2) = (i + \alpha_A)\left(\frac{g_A}{1 + S_A|A_n|^2} - \gamma_A\right), \tag{4.2a}$$

$$V_{B,n}(|B_n|^2) = (i + \alpha_B)\left(\frac{g_B}{1 + S_B|B_n|^2} - \gamma_B\right) \tag{4.2b}$$

model nonlinear saturable gain of strength g_s and background loss γ_s, where the real constants S_s and α_s are the self-saturation coefficient and the linewidth-enhancement (or anti-guiding) factor, respectively. The linewidth-enhancement factor originates from the inherent uncertainty in the spectral energy levels of the gain medium, this leads to stimulated emission which is not perfectly monochromatic, relating changes in phase to changes in gain. The self-saturation coefficient describes the value at which the rate of population inversion is maximised with respect to the pump power.

The couplings κ_n and κ'_n follow the same sequence as given in the SSH model of section 1.3.2, where $\kappa = t_1$ and $\kappa' = t_2$. Recalling this model, it displays a symmetric band structure with a gap of size $\Delta = 2|\kappa - \kappa'|$ around the central frequency ω_{AB}, which induces two topological phases α (where $\kappa > \kappa'$) and β (where $\kappa < \kappa'$). A localised defect state is pinned at the interface between the two phases, which appears at $\Omega_0 = \omega_{AB}$ and is pinned to the centre of the gap. This constitutes the first model I will consider, given in figure 4.1(a). Due to its topological origin this mode persists for more complicated interface configurations, which I will exploit to change its mode volume as shown in Fig. 4.1(b). There, the terminating dimer chains operate as topological mirrors while the defect mode extends uniformly over the central part of the system.

Next, I introduce sublattice dependent gain and loss, where the sublattice with the defect state contains gain and both sublattices receive uniform losses. This selectively enhances the topological mode. Assuming that the gain and loss are linear ($S_s = 0$) and do not break the symmetry of the frequency spectrum ($\alpha_s = 0$), the topological mode then acquires the effective gain $G_A = g_A - \gamma_A$ on the A sublattice, while all bulk modes acquire the average effective gain $\bar{G} = (g_A + g_B - \gamma_A - \gamma_B)/2$ (see the right panels in figure 4.1). The topological protection persists because the effective non-hermitian Hamiltonian exhibits a non-hermitian charge-conjugation symmetry $(H - \omega_{AB})^* = -\sigma_z(H - \omega_{AB})\sigma_z$ (with the Pauli matrix σ_z operating in sublattice space), which stabilises any complex eigenvalues Ω_n positioned on the axis $\mathrm{Re}\,\Omega_n = \omega_{AB}$ [22,23,31,125–127].

This linear mechanism describes an initial competitive advantage to the defect mode if $G_A > \bar{G}$ and allows it to dynamically switch on if $G_A > 0$ and the intensity is still small. This however, does not describe the quasi-stationary operation regime where the gain medium saturates in response to a much larger intensity. The saturation is critical for the stabilisation of any laser at its working point, where the medium provides just as much energy as the lasing mode loses through radiative and absorptive processes.

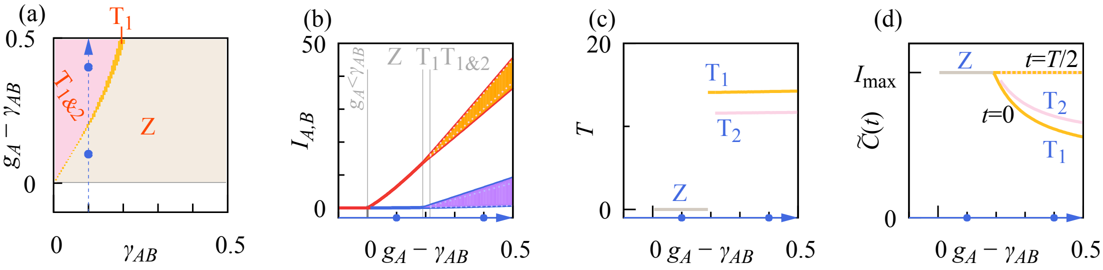

Figure 4.2: Topological lasing regimes for the SSH array of figure 4.1(a) pumped on the A sublattice (finite gain g_A at fixed $g_B = 0$, with amplitudes scaled such that $S_A = S_B = 1$) under conditions that preserve the symmetries in the linear case ($\omega_{s,n} = \omega_{AB}$, $\alpha_s = 0$), demonstrating operation in topological states over the whole parameter range. (a) Phase diagram of stable quasistationary operation regimes depending on the gain g_A and background losses $\gamma_A = \gamma_B \equiv \gamma_{AB}$, where lasing requires $g_A > \gamma_{AB}$. Over the whole grey region labelled Z, the system establishes stationary lasing in a topological zero mode. In the orange region, this is replaced by operation in a twisted topological mode T$_1$ displaying power oscillations. In the pink region an additional twisted state T$_2$ exists, whose selection then depends on the initial conditions. The remaining panels analyse the lasing characteristics for varying gain g_A along the line $\gamma_{AB} = 0.1$ (blue arrow in the phase diagram). (b) Sublattice-resolved intensities I_A (red) and I_B (blue), including shaded intensity ranges for the power oscillations of T$_1$ and dashed lines indicating the corresponding ranges for T$_2$. (c) Amplitude oscillation period T (equalling twice the period of power oscillations for twisted states, see Fig. 4.3). (d) Correlation function $\tilde{C}(t)$ at $t = 0, T/2$, where $\tilde{C}(T/2) = I_{\max}$ reveals the topological nature of the states (see text). As illustrated for the examples in Fig. 4.3, all states inherit the intensity profile of the linear defect mode from Fig. 4.1(a).

4.1.2 Symmetries and solutions

The nonlinear modification (4.2) of the model ($S_s \neq 0$) includes the saturation dynamics. This makes the effective gain or loss non-uniform across the whole system and favours modes with a large mode volume. Symmetry breaking is induced when the linewidth-enhancement factor α_s is non-zero. Also a non-Hermitian charge conjugation symmetry which is satisfied by the non-linear potential [128] can be realised. By inspection of equations (4.1) and (4.2), solutions of the form

$$\Psi(t) = \begin{pmatrix} \mathbf{A}(t) \\ \mathbf{B}(t) \end{pmatrix} \tag{4.3}$$

with parameters $(\omega_{s,n}, \kappa_n, \kappa'_n, g_s, \gamma_s, \alpha_s, S_s)$, have charge-conjugation symmetric partners of the form

$$\tilde{\Psi}(t) = \exp(-2i\omega_{AB}t)\begin{pmatrix}\mathbf{A}^*(t)\\ -\mathbf{B}^*(t)\end{pmatrix} \tag{4.4}$$

at the parameters $(\tilde{\omega}_{s,n} = 2\omega_{AB} - \omega_{s,n}, \kappa_n, \kappa'_n, g_s, \gamma_s, -\alpha_s, S_s)$. Time-dependent solutions which are charge-conjugation symmetric will then appear as natural extensions to the topological SSH linear modes if they are zero modes with respect to the background frequency $\omega_{s,n} = \omega_{AB}$ and there is no charge-conjugation symmetry breaking $\alpha_s = 0$. I tune out the background frequency $\omega_{AB} \equiv 0$ through the gauge transformation $\Psi(t) \to \Psi(t)\exp(-i\omega_{AB}t)$, for direct comparison with the linear model.

For the remainder of this section I will discuss solutions to the non-linear wave equation which appear in several types. They can be self-symmetric stationary states $\Psi(t) = \tilde{\Psi}(t) = \mathrm{const}(t)$, which I denote as the nonlinear topological zero modes [Z], they can also be time dependant version of these states [S], and also periodic 'twisted' modes $\Psi(t + T/2) = \tilde{\Psi}(t)$ [T] which display power oscillations with period $T/2$. These periodic modes are also self periodic $\Psi(t + T) = \Psi(t)$ with period T. Lastly, I will show stationary and time-dependent lasing modes that spontaneously break the dynamical symmetry, which automatically occur in pairs $\Psi(t)$, $\tilde{\Psi}(t)$ [P].

To distinguish between these types of modes I use the correlation functions

$$C(t) = |\langle\Psi(t_{\max})|\Psi(t_{\max} + t)\rangle|, \tag{4.5a}$$

$$\tilde{C}(t) = |\langle\tilde{\Psi}(t_{\max})|\Psi(t_{\max} + t)\rangle|. \tag{4.5b}$$

For periodic modes I choose $t_{\max}$ such that I begin with the intensity maximum over one period $C(0) = I_{\text{max}}$. For stationary modes t_{max} is arbitrary and I_{max} is to be interpreted as the stationary intensity. Self-symmetric modes are characterised correlation functions which coincide $\tilde{C}(t) = C(t)$. For twisted modes the correlation functions alternate with an offset $T/2$, hence $\tilde{C}(t) = C(t + T/2)$ and $\tilde{C}(T/2) = I_{\text{max}}$. For symmetry-breaking modes, the two correlation functions are not simply related but are constrained by $\tilde{C}(t) < I_{\text{max}}$ for all t.

I begin by considering lasing under ideal conditions, where charge-conjugation symmetry must be present $\alpha_s = 0$ and gain confined to the A sublattice (g_A finite and variable by the pumping, while $g_B = 0$) and the background losses are uniform $\gamma_A = \gamma_B \equiv \gamma_{AB}$. I scale the amplitudes $\mathbf{A}$ and $\mathbf{B}$ such that the self-saturation coefficients are unity $S_A = S_B = 1$, and randomise initial conditions such that the populated mode is not a consequence of the chose of those initial conditions.

The phase space of solution for this operational regime is given in panel a of figure 4.2. Over a large part of the parameter space, the laser operates in a stable zero mode, which is quickly approached over time. In the phase diagram (panel a), this region is indicated by the label Z. When the gain/loss ratio is increased the zero mode becomes unstable and is replaced by a twisted mode T_1, which results in lasing with power oscillations. This occurs due to a topological phase transition, I shall go into more detail about the mechanism behind this in the next section when I examine the stability spectrum. Upon a small further increase of the gain/loss ratio the mode T_1 starts to compete with a second twisted mode T_2. Both modes sustain stable lasing with power oscillations of different amplitude and period, where the choice of mode depends on the initial conditions.

Panels (b-c) in figure 4.2 shows the gain-dependence of the sublattice-resolved intensities $I_A = |\mathbf{A}|^2$ (orange) and $I_B = |\mathbf{B}|^2$ (blue). Panel b is the so-called light-light curve, which displays the characteristic kink as the laser threshold is crossed $g_A = \gamma_{AB}$. Initially the stationary solution given by the zero mode Z can be seen where the intensity on the sublattice without gain I_B initially remains negligible.

Upon increasing the gain, the stationary regime is replaced by lasing in the twisted mode T_1, where I_B becomes finite and from its onset displays a finite period T while the amplitude of its power oscillations (of period $T/2$) increase smoothly (given by the shaded intensity ranges). The second twisted mode sets in with a slightly smaller period, but covers very similar intensity ranges (indicated by the dashed white lines). Panel (d) in figure 4.2 verifies the symmetry-protected nature of these states throughout the whole range of gain. For the self-symmetric zero mode Z $\tilde{C}(0) = I_{\max}$. Both of the twisted modes are not self-symmetric, $\tilde{C}(0) < I_{\max}$, but display continuity of the maximum intensity $\tilde{C}(T/2) = I_{\max}$.

Plotting individual realisations, the modes maintain the exponentially localised trademark of the localised state at all times up to the beating effect of the twisted modes as demonstrated for the three solutions shown in panel (a) of figure 4.3. Panel (b) show that the intensities on both sublattices oscillate out of phase, and so do the correlation functions $C(t)$ and $\tilde{C}(t)$ given in panel (c). Furthermore, comparing panels (b) and (c) the period $T/2$ of the power oscillations in $I_{A,B}(t)$ is half of the amplitude oscillations exhibited by the amplitude correlation functions.

4.2 Stability analysis: Theory

In the previous section I showed that the topological states are surprisingly stable in the presence of the non-linear potential provided that the gain/loss ratio is is away from the phase transition between the different types of modes. In this section I perform a stability analysis to show that this modes are topologically protected, but first this requires reformulating the problem to make the linearisation around the working point clearer. I begin by reformulating the non-linear wave equations (4.1) as the matrix equation

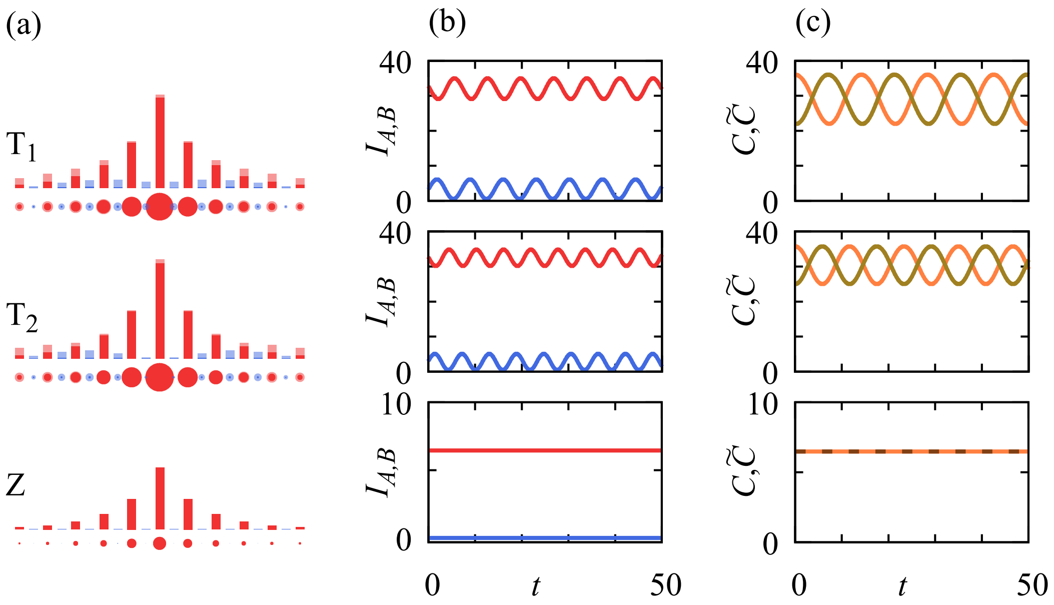

Figure 4.3: Topological wave features of representative lasing states at parameters indicated by blue dots in figure 4.2 ($g_A = 0.2$ for Z, $g_A = 0.5$ for T_1 and T_2). (a) Intensity distributions over the array, shown both as spikes and as disks with area proportional to intensity, substantiating the relation of these stabilised states to the linear defect state from figure 4.1(a). (b,c) Time-dependence of the sublattice-resolved intensities $I_A(t)$ and $I_B(t)$ (red and blue) and of the correlation functions $C(t)$, $\tilde{C}(t)$ (orange and brown). The alternating correlations $\tilde{C}(t + T/2) = C(t)$ verify the twisted nature of the states T_1 and T_2, while $C(t) = \tilde{C}(t) = \mathrm{const}$ verifies that the state Z is a topological zero mode.

$$i\frac{d}{dt}\Psi(t) = H\Psi(t) + V[\Psi(t)]\Psi(t), \quad \Psi(t) = \begin{pmatrix} \mathbf{A}(t) \\ \mathbf{B}(t) \end{pmatrix}, \tag{4.6}$$

$$H = \begin{pmatrix} \omega_A & K \\ K^T & \omega_B \end{pmatrix}, \quad V[\Psi] = \begin{pmatrix} V_A & 0 \\ 0 & V_B \end{pmatrix}, \tag{4.7}$$

where the matrix

$$K_{nm} = \delta_{nm}\kappa_n + \delta_{n,m+1}\kappa'_n \tag{4.8}$$

represents the couplings. The resonance frequencies and nonlinear potentials (corresponding to equation (4.2)) are the diagonal matrices,

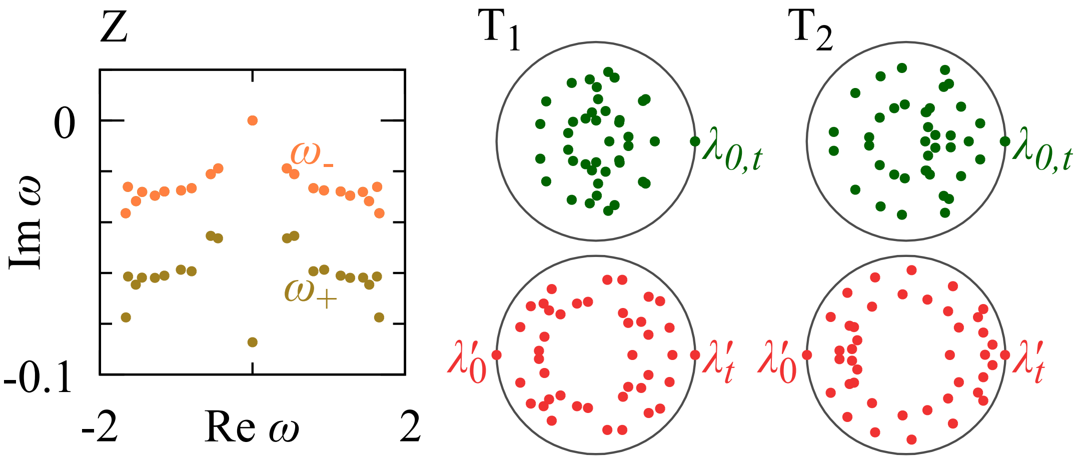

Figure 4.4: Stability excitation spectra of the representative states illustrated in figure 4.3. For the stationary state Z this represents the Bogoliubov spectrum ω, which separates into excitations $\omega_\pm$ that preserve or break the symmetry. This separation further verifies its zero-mode character (see text), while $\mathrm{Im}\,\omega < 0$ [apart from the U(1) Goldstone mode at $\omega = 0$] affirms that the state is stable. For the periodically oscillating states T$_1$ and T$_2$, this represents the Bogoliubov-Floquet stability spectrum λ (top, green) and the spectrum λ' of the half-step propagator (bottom, red). Both spectra are confined by the unit circle in the complex plane, demonstrating that these states are stable. The symmetry-protected excitations pinned to $\lambda' = \pm 1$ further verify the twisted nature of these states.

$$\omega_{A,nm} = \delta_{nm}\omega_{A,n}, \quad \omega_{B,nm} = \delta_{nm}\omega_{B,n}, \tag{4.9}$$

$$V_{A,nm} = \delta_{nm}V_{A,n}, \quad V_{B,nm} = \delta_{nm}V_{B,n}. \tag{4.10}$$

Stationary states $\Psi(t) = \exp(-i\Omega_n t)\Psi^{(n)}$ with real frequency Ω_n are determined as self-consistent solutions of the equation

$$\Omega_n\Psi^{(n)} = (H + V[\Psi^{(n)}])\Psi^{(n)}, \tag{4.11}$$

while general periodic states of period T fulfil

$$\Psi(T) = \exp(-i\varphi)\Psi(0) \tag{4.12}$$

with a real phase φ.

Again setting the reference frequency $\omega_{AB} = 0$, the matrices satisfy charge-conjugation symmetry

$$(H+V)^*|_{\omega_{s,n},\alpha_s} = -\sigma_z(H+V)\sigma_z|_{-\omega_{s,n},-\alpha_s} \tag{4.13}$$

where σ_z is the z Pauli matrix. The solutions must also be connected by charge-conjugation symmetry

$$\tilde{\Psi}(t)|_{-\omega_{s,n},-\alpha_s} = \sigma_z\Psi(t)|_{\omega_{s,n},\alpha_s}, \tag{4.14}$$

which in this system holds for $\alpha_s = 0$, $\omega_{s,n} = 0$. The coupling matrix K is the familiar $(N+1)\times N$-dimensional matrix (as there is one more A site than B sites) discussed in section 1.3.2. The zero-mode in the linear regime satisfies $K^T\mathbf{A}^{(Z)} = 0$, $\mathbf{B}^{(Z)} = 0$ [57] and obeys $H_0\Psi^{(Z)} = iG_A\Psi^{(Z)}$, which above threshold $(G_A > 0)$ is an exponentially increasing state and is therefore unphysical. The non-linearity provides the necessary feedback to make the state stable as evidenced by it's presence in the previous section.

In the nonlinear case, the relation between solutions at fixed parameters applies to stationary zero modes

$$\Psi^{(Z)} = \tilde{\Psi}^{(Z)}, \tag{4.15}$$

which now must be stabilised at an exactly vanishing frequency $\Omega_Z = 0$ [see Eq. (4.11)], and twisted modes

$$\Psi^{(T)}(T/2) = \tilde{\Psi}^{(T)}(0). \tag{4.16}$$

For both cases, these definitions exploit the U(1) gauge freedom to multiply any solution by an overall phase factor $\exp(i\chi)$. For exmaple, if a zero mode fulfils

$\Psi^{(Z)\prime} = \exp(-2i\chi)\tilde{\Psi}^{(Z)\prime}$ then $\Psi^{(Z)} = \pm\exp(i\chi)\Psi^{(Z)\prime}$ fulfils equation (4.15), and the same redefinition applies for a twisted mode $\Psi^{(T)\prime}(T/2) = \exp(-2i\chi)\tilde{\Psi}^{(T)\prime}(0)$. Irrespective of these redefinitions, zero modes always display a rigid phase difference of $\pm\pi/2$ between the amplitudes on the A and the B sublattice, while twisted modes always fulfil $\Psi(T) = \Psi(0)$, as they are periodic modes (4.12) with guaranteed $\varphi = 0$.

4.2.1 Stability analysis

Given a general solution $\Psi(t)$ of the nonlinear wave equation (4.6), the stability of the mode can be analysed by adding a small perturbation,

$$\delta\Psi(t) = u(t) + v^*(t), \quad u = \begin{pmatrix} u_A(t) \\ u_B(t) \end{pmatrix}, \quad v = \begin{pmatrix} v_A(t) \\ v_B(t) \end{pmatrix}, \tag{4.17}$$

and linearising in u and v. This form utilises the charge-conjugation symmetry of the system and yields the Bogoliubov equation

$$i\frac{d}{dt}\psi(t) = \mathcal{H}[\Psi(t)]\psi(t), \quad \psi(t) = \begin{pmatrix} u_A(t) \\ u_B(t) \\ v_A(t) \\ v_B(t) \end{pmatrix}. \tag{4.18}$$

The corresponding Bogoliubov Hamiltonian is given by

$$\mathcal{H}[\Psi] = \begin{pmatrix} H + \Gamma & \Delta \\ -\Delta^* & -H^* - \Gamma^* \end{pmatrix}, \tag{4.19}$$

$$\Gamma = \begin{pmatrix} \Gamma_A & 0 \\ 0 & \Gamma_B \end{pmatrix}, \quad \Delta = \begin{pmatrix} \Delta_A & 0 \\ 0 & \Delta_B \end{pmatrix}, \tag{4.20}$$

where

$$\Gamma_{A,nm} = \delta_{nm}(i + \alpha_A)\left(\frac{g_A}{(1 + S_A|A_n|^2)^2} - \gamma_A\right), \tag{4.21}$$

$$\Gamma_{B,nm} = \delta_{nm}(i + \alpha_B)\left(\frac{g_A}{(1 + S_B|B_n|^2)^2} - \gamma_B\right), \tag{4.22}$$

$$\Delta_{A,nm} = -\delta_{nm}(i + \alpha_A)\frac{S_A g_A A_n^2}{(1 + S_A|A_n|^2)^2}, \tag{4.23}$$

$$\Delta_{B,nm} = -\delta_{nm}(i + \alpha_B)\frac{S_B g_B B_n^2}{(1 + S_B|B_n|^2)^2}. \tag{4.24}$$

For a stationary state fulfilling the self consistency condition given in equation (4.11), solutions are of the form $u_s = \exp(-i\Omega_n t - \omega_m t)u_s^{(m)}$, $v_s = \exp(i\Omega_n t - \omega_m t)v_s^{(m)}$ $(s = A, B)$, which follow from the eigenvalue equation

$$\omega_m \psi^{(m)} = \left(\mathcal{H}[\Psi^{(n)}] - \Omega_n \Sigma_z\right)\psi^{(m)}, \tag{4.25}$$

where

$$\Sigma_z = \begin{pmatrix} 1 & 0 & 0 & 0 \\ 0 & 1 & 0 & 0 \\ 0 & 0 & -1 & 0 \\ 0 & 0 & 0 & -1 \end{pmatrix}. \tag{4.26}$$

The stability of stationary states can therefore be ascertained by inspecting the corresponding spectrum of this equation for a given solution $\Psi(t)$. There are twice as many eigenvalues representing excitations in this equation as there are states in the linear system. The excitations themselves are constrained by a second charge-conjugation symmetry which arises for free from the complex form of the excitations. This can be seen from the Bogoliubov equation

$$(\mathcal{H}[\Psi])^* = -\Sigma_x \mathcal{H}[\Psi] \Sigma_x, \tag{4.27}$$

where

$$\Sigma_x = \begin{pmatrix} 0 & 0 & 1 & 0 \\ 0 & 0 & 0 & 1 \\ 1 & 0 & 0 & 0 \\ 0 & 1 & 0 & 0 \end{pmatrix}. \tag{4.28}$$

Excitations are then either imaginary $\mathrm{Re}\,\omega_n = 0$ or occur in the pairs ω_n, $\tilde{\omega}_n = -\omega_n^*$.

This includes a U(1) Goldstone mode

$$\psi^{(0)} = \begin{pmatrix} \Psi^{(n)} \\ -\Psi^{(n)*} \end{pmatrix}, \quad \omega_0 = 0, \tag{4.29}$$

which accounts for the free choice of the overall phase factor of a stationary solution.

For a periodic state (4.12), the Bogoliubov equation is integrated over the period of oscillation, so that $\psi(T) = U(T)\psi(0)$, where $U(T)$ is a propagator. The Bogoliubov-Floquet operator can be written as follows

$$F = \exp(i\Sigma_z \varphi) U(T), \tag{4.30}$$

where the phase factor φ plays the same role as the shift to that of Ω_n in equation (4.25). The eigenvalues of the Bogoliubov-Floquet operator are denoted as $\lambda_m = \exp(-i\omega_m T)$. In both the stationary case and the time-dependant case, a solution is stable if all eigenvalues fulfil $\mathrm{Im}\,\omega_m \leq 0$, so that the associated perturbations do not grow over time.

The Bogoliubov-Floquet spectrum contains complex-conjugate pairs of eigenvalues λ_m, $\tilde{\lambda}_m = \lambda_m^*$ and individual real eigenvalues $\lambda_m = \lambda_m^*$. This again includes a U(1) Goldstone mode

$$\psi^{(0)} = \begin{pmatrix} \Psi(t) \\ -\Psi^*(t) \end{pmatrix}, \quad \lambda_0 = 1 \tag{4.31}$$

reflecting the free choice of the overall phase of any solution, and now also a time-translation Goldstone mode

$$\psi^{(t)} = \begin{pmatrix} d\Psi/dt \\ d\Psi^*/dt \end{pmatrix}, \quad \lambda_t = 1 \tag{4.32}$$

that reflects the freedom to displace any solution $\Psi(t)$ in time.

4.2.2 Topological modes

To make some more specific statements about the excitation spectra of the topological modes, I first recall from the previous section that on top of the charge-conjugation symmetry put forth by the Bogoliubov equation, the modes themselves have an additional charge-conjugation symmetry if $\alpha_s = 0$, $\omega_{s,n} = 0$. This means that the excitation spectrum satisfies

$$\chi(H[\Psi_n] - \Sigma_z\Omega_n)^*\chi = -(H[\tilde{\Psi}_n] + \Sigma_z\Omega_n), \tag{4.33}$$

where $\chi = \mathbb{1}_2 \otimes \sigma_z$. For stationary mode the perturbations in the presence of this additional charge-conjugation symmetry can be classified in terms of joint eigenstates of χ with eigenvalue $\epsilon = \pm 1$. The eigenstates are related according to $v_\epsilon = \epsilon \sigma_z u_\epsilon$, and fulfil the reduced eigenvalue equations

$$\omega_{+,n} u_{+,n} = (H + 2\Gamma - V) u_{+,n} \tag{4.34}$$

$$\omega_{-,n} u_{-,n} = (H + V) u_{-,n}, \tag{4.35}$$

for symmetry-preserving modes $v_{+,n} = u_{+,n}$ and symmetry-breaking modes for $v_{-,n} = u_{-,n}$ respectively. In the language of equation (4.17), symmetry-preserving corresponds to the relation $v_A = u_A$, $v_B = -u_B$, whilst for the symmetry-breaking this corresponds to $v_A = -u_A$ and $v_B = u_B$. The symmetry breaking modes also include the U(1) goldstone mode from equation (4.29), now expressed as $u^{(-,0)} = \Psi^{(n)}$, $\omega_{-,0} = 0$.

For twisted modes (4.16), the Bogoliubov-Floquet propagator can be factorised

$$\begin{aligned} F &= \mathcal{Z} U^*(T/2) \mathcal{Z} U(T/2) \\ &= \mathcal{Z} \Sigma_x U(T/2) \Sigma_x \mathcal{Z} U(T/2) \\ &= F'^2, \end{aligned} \tag{4.36}$$

$$F' = \mathcal{Z} \Sigma_x U(T/2), \tag{4.37}$$

which defines the twisted half-step propagator F'. Its eigenvalues λ'_m determine the stability spectrum as $\lambda_m = (\lambda'_m)^2$. The U(1) Goldstone mode (4.31) fulfills $\psi^{(0)}(T/2) = -\mathcal{Z}\Sigma_x \psi^{(0)}(0)$, so that the associated eigenvalue $\lambda'_0 = -1$, while the time-translation mode (4.32) fulfills $\psi^{(t)}(T/2) = \mathcal{Z}\Sigma_x \psi_T(0)$, so that $\lambda'_t = 1$.

Now that both the stationary and time-dependant solutions have appropriate formulations of perturbations in terms of their excitation spectra, which have been decomposed into symmetry-breaking and symmetry-preserving excitations, I will demonstrate in the next section how this spectral analysis can be used to show the transitions between topological phases.

4.3 Stability analysis: application

A state is stable if all physical excitations decay, $\mathrm{Im}\,\omega_n < 0$ (hence $|\lambda_n| < 0$). An exception is the U(1) Goldstone mode pinned at $\omega_0 = 0$ ($\lambda_0 = 1$), which arises from the arbitrary choice of the global phase of the wavefunction Ψ. This phase can diffuse due to quantum noise, which results in the finite linewidth of the emitted laser light. Furthermore, in the Floquet case an additional pinned eigenvalue $\lambda_t = 1$ arises from the arbitrary choice of the reference time t_0 for any solution $\Psi(t + t_0)$.

Consider again the three topological regimes identified in figure 4.3. For a given stationary zero-mode Z, the excitations spectrum can be understood through examining the Bogoliubov spectrum given in the left hand panel of figure 4.4. The excitations which preserve the self-symmetry of the topological mode are given by the eigenvalues $\omega_{+,n}$, and those that break the self-symmetry are given by $\omega_{-,n}$. Since the eigenvalues of $\omega_{-,n}$ all lie within the lower half of the complex plane, the stationary zero-mode is a stable solution. The eigenvalues $\omega_{-,n}$ also contain the Goldstone mode $\omega_{-,0} = 0$, and describes the more slowly decaying excitations.

The other panels of figure 4.4 contain the Floquet spectra belonging to the twisted half-step propagator of the T_1 and T_2 modes over half a period $T/2$. Here the eigenvalues $\lambda_n = {\lambda'_n}^2$ are confined to the unit circle. This reduced spectrum contains a mode pinned at $\lambda'_t = 1$, which arises from time-translation invariance, and a mode pinned to $\lambda'_0 = -1$, which originates from the U(1) Goldstone mode.

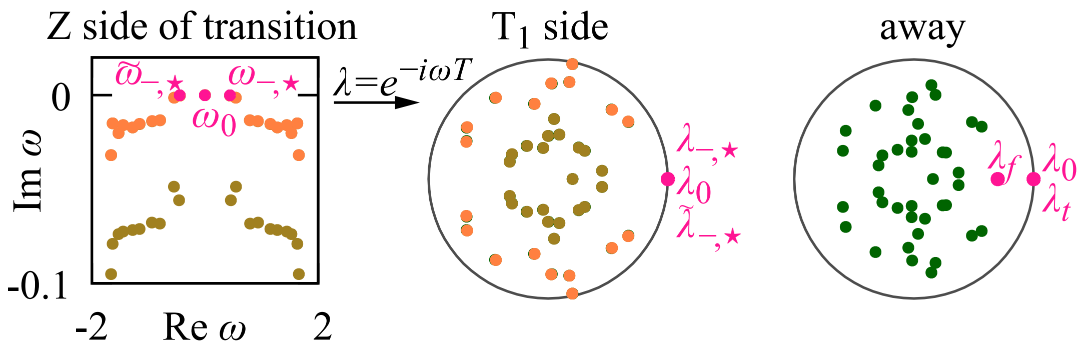

Figure 4.5: Topological phase transition between the zero-mode regime Z and the twisted mode T$_1$, at $g_A = 0.291$ along the line $\gamma_{AB} = 0.1$ (see figure 4.2). At the transition two Bogoliubov excitations $\omega_{-,\star} = 2\pi/T$ and $\tilde{\omega}_{-,\star} = -\omega_{-,\star}$ are marginally stable, where T is the period of the emerging twisted mode T$_1$. Along with the U(1) Goldstone mode, they all map onto Floquet-Bogoliubov excitations $\lambda = 1$ for this emerging mode. Away from the transition, these excitations split into two degenerate excitations $\lambda_0 = \lambda_t = 1$ associated with the U(1) and time translation freedoms, and a decaying excitation λ_f related to the amplitude stabilisation of the power oscillations. (Note that at the transition another pair of excitations is almost unstable, which will give rise to the twisted mode T$_2$.)

This configuration of excitations for propagation over half a period constitutes a distinctive topological signature of the twisted modes. This time if the eigenvalues $|\lambda_n| < 1$ the oscillating modes remain stable.

The described features are further illuminated when one inspects the phase transition between the zero-mode regime and the twisted state T$_1$. In the general setting of nonlinear optical systems [129, 130], this transition corresponds to a Hopf bifurcation, which here however occurs in a symmetry-constrained setting. Panel (a) of figure 4.5 shows the Bogoliubov spectrum at the transition, where a pair of symmetry-breaking excitations with $\tilde{\omega}_{-,\star} = -\omega_{-,\star}$ crosses the real axis and thereby destabilises the zero mode. This pair of excitations combine to display the oscillatory time dependence of the emerging twisted state T$_1$, whose initial oscillation frequency is given by $2\pi/T = |\omega_{-,\star}|$. Different combinations of these two excitations amount to a time translation of these resulting oscillations. Notably, at the transition the Bogoliubov-Floquet spectrum of this emergent state is given by $\lambda_n = \exp(-i\omega_n T)$, as is illustrated in panel (b) of figure 4.5.

Upon this mapping the destabilising excitations $\tilde{\omega}_{-,\star} = -\omega_{-,\star}$ map to $\lambda_{-,\star} = \tilde{\lambda}_{-,\star} = 1$. For the twisted mode, they therefore constitute two excitations that right at the transition are both degenerate with the U(1) Goldstone mode. Departing from the transition into the twisted-state regime, these excitations shown in panel (c) if figure 4.5 split into two separate real eigenvalues λ_t and λ_f. Of these, λ_t describes the time-translation freedom and therefore remains degenerate with the U(1) Goldstone mode. The eigenvalue λ_f, on the other hand, is associated with perturbations of the finite amplitude of the power oscillations. These perturbations decay due to the nonlinear feedback, so that $|\lambda_f| < 1$, guaranteeing that the oscillations are stable. This mechanism gives rise to the aforementioned topological excitations $\lambda'_0 = -1$, $\lambda'_t = 1$ in the half-step propagator, which remain a robust signature of the twisted state even when one moves far away from the transition, as already shown in the examples of figure 4.4.

4.3.1 Beyond ideal conditions

The previous sections were focused on understanding the operational regimes of topological modes in an idealised laser array. To verify the versatility and resilience of the topological modes, I consider two modifications to the mode competition between the different states in the system.

4.3.2 Modified gain distribution

Figure 4.6 examines the role of the gain distribution via the addition of finite gain $g_B = 0.1$ on the B sublattice, which amounts to a reduction of the gain imbalance. In the linear model, the additional gain does not affect the defect state, which sees the effective gain G_A, but increases the effective gain $\bar{G}$ of all the other states in the system (see figure 4.1). In the nonlinear model, the additional gain modifies the operation regimes in parts of the region $\gamma_{AB} < g_B$, where the

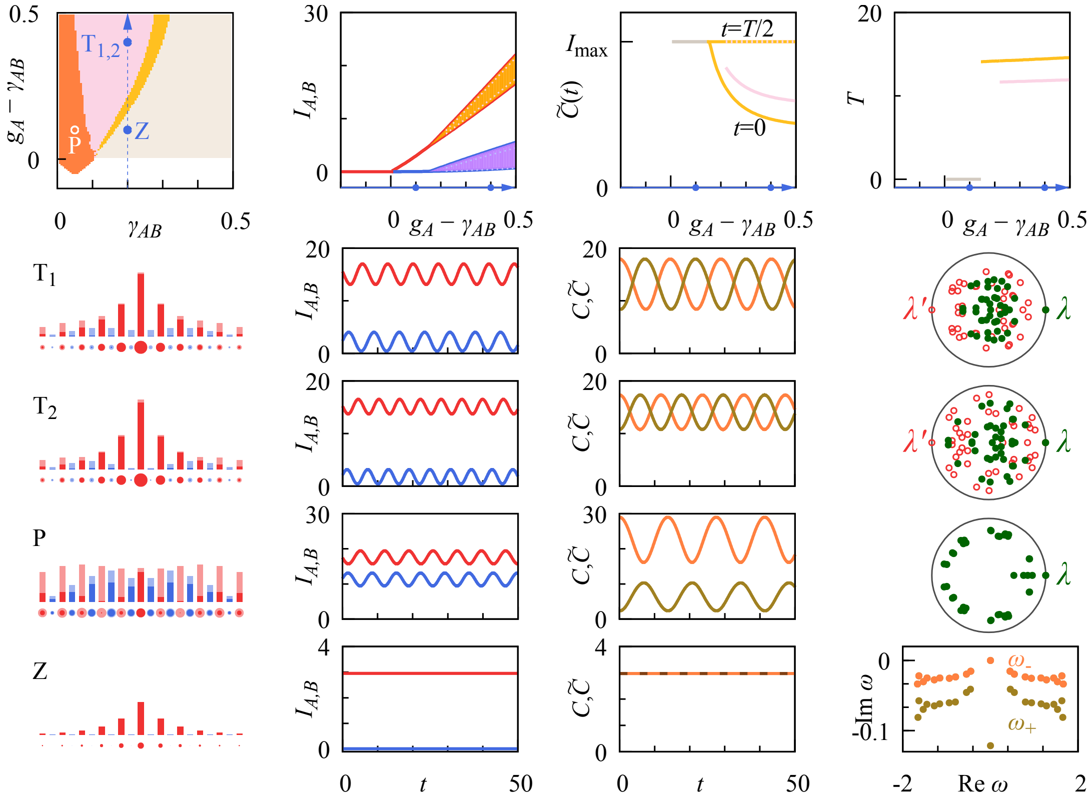

Figure 4.6: Role of reduced gain imbalance, obtained under the same conditions as in figures 4.2-4.4, but with finite gain $g_B = 0.1$ on the B sublattice. For $\gamma_{AB} < g_B$ the parameter space now also contains a region (dark orange) supporting additional pairs of symmetry-breaking modes P. As illustrated for the marked example, these modes have substantial weight on the B sublattice, while their independent correlation functions $C(t)$ and $\tilde{C}(t)$ show that they spontaneously break the symmetry. For such modes the Bogoliubov-Floquet spectrum contains many eigenvalues close to the unit circle, indicating their high sensitivity under parameter changes. As shown in the top panels for the cross-section now placed at $\gamma_{AB} = 0.2$, the remaining parameter space supports the same robust topological lasing modes as observed for $g_B = 0$ (twisted modes T_1 and T_2 and stationary topological modes Z, as illustrated by the marked examples).

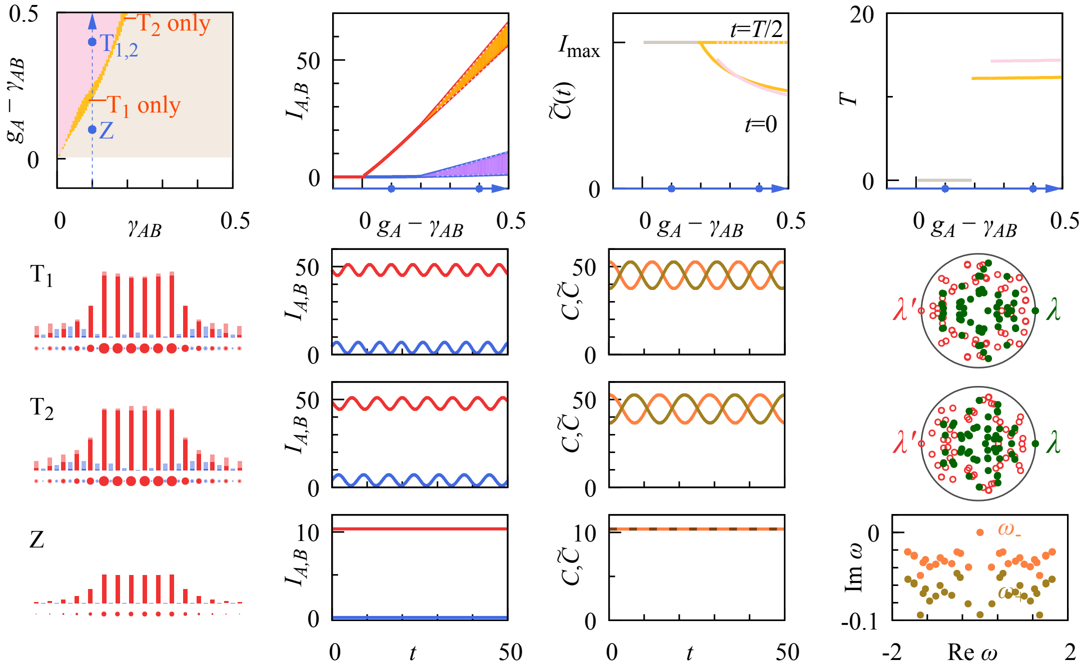

Figure 4.7: Role of increased mode volume, obtained for the laser array with topological mirrors illustrated in figure 4.1(b). Here I consider ideal lasing conditions with variable gain g_A and background loss $\gamma_A = \gamma_B \equiv \gamma_{AB}$, at vanishing gain $g_B = 0$ on the B sublattice. The representation of the data is the same as in figure 4.6. The resulting operation regimes closely resemble those of the SSH laser array under corresponding conditions (see figures 4.2-4.4), with a phase of stationary zero-mode lasing supplemented by phases with one or two twisted modes displaying power oscillations. The intensities of these modes have increased, which reflects their larger mode volume, as illustrated in more detail for the three examples marked Z, T_1 and T_2.

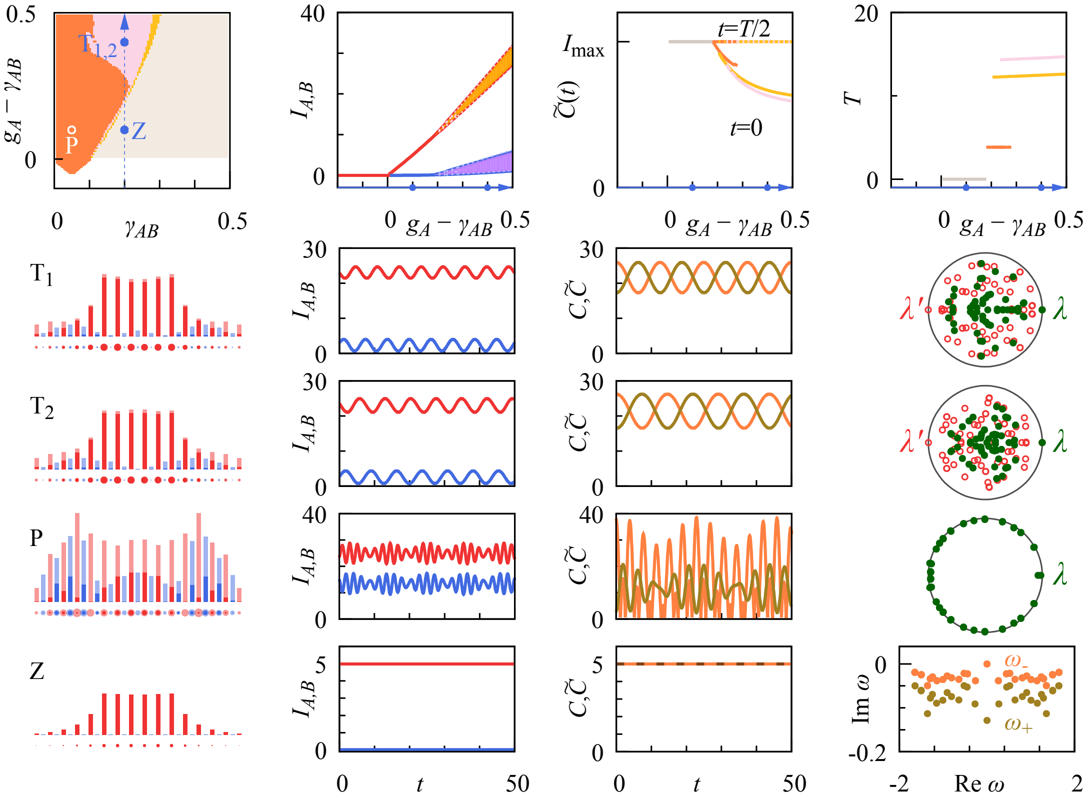

Figure 4.8: Interplay of mode volume and gain imbalance. Same as figure 4.7, but for finite gain $g_B = 0.1$ on the B sublattice, and the cross-section through parameter space shifted to $\gamma_{AB} = 0.2$. Compared to the corresponding conditions in the SSH laser array (figure 4.6), a larger range of parameters now supports a multitude of additional states. At the representative point marked P, this includes a pair of symmetry-breaking oscillating states, whose power oscillations are modulated. The features of these symmetry-breaking states are not very robust, as indicated by their Bogoliubov-Floquet stability spectra, which display many slowly decaying excitations. These modifications are restricted to the range of parameters that previously displayed the twisted states T_1 and T_2 (now only seen for large enough gain), but does not affect the operation in the zero-mode Z. Along the cross-section $\gamma_{AB} = 0.2$, we enter only briefly enter this modified regime, in a region where there is only one extra, twisted, state, which destabilises the zero mode.

losses are not strong enough to suppress modes with substantial weight on the B sublattice. Besides additional twisted modes, this region then becomes populated by oscillating pairs of symmetry-breaking modes P. As shown for an example in the figure, where these modes extend over the whole system and display substantial weight on both sublattices. The Bogoliubov-Floquet spectrum of any two partner modes are identical, but they cannot be further deconstructed. The position of the eigenvalues close to the unit circle reflects a reduced robustness of these symmetry-breaking modes against parameter variations.

In the remainder of parameter space the same topological operation regimes are encountered as in the ideal case, with the boundary between zero modes and twisted modes now shifted to larger losses. The modes themselves display the same features as before, as illustrated for variable gain g_A along the line $\gamma_{AB} = 0.2$. The threshold to stationary lasing again gives rise to a marked increase of intensity on the A sublattice, while the power oscillations of the twisted states at larger gain display very similar periods and relative amplitudes as before. The three marked examples verify that these topological modes still inherit their mode profile from the linear defect state, and display the required topological correlations and excitations that can only change in phase transitions.

4.3.3 Modified mode volume

A different strategy to consider the increased mode competition to the topological states is to consider a realisation where the defect state region is extended to include a region of uniform coupling. The schematic for this modified set up is shown in panel (b) of figure 4.1. Figures 4.7 and 4.8 examine this modified set-up. In the linear system, the terminating regions act as selective mirrors for a zero mode with an increased mode volume, which remains confined to the A sublattice. Furthermore, because of its increased length the system also supports a larger number of extended states that compete for the gain. In figure 4.7 the gain on the B sublattice is set to $g_B = 0$, while in figure 4.8 the gain on the B sublattice is again small but finite $g_B = 0.1$.

In the ideal case $g_B = 0$, the resulting operation regimes closely resemble those of ideal lasing in the SSH laser array (compare figure 4.7to that of figures 4.2-4.4). The parameter space is divided into a region with a topological zero mode Z and regions with one or two twisted modes T_1 and T_2. Each of these modes can now be involved in the topological phase transition with the stationary zero mode, with a crossover point $g_A \approx 0.59, \gamma_{AB} \approx 0.17$. The modes continue to show all the required topological signatures in their correlation functions and stability excitation spectra. However, they all now display a larger mode volume, which is inherited from the profile of the zero mode in the linear case. As a consequence, the output power of these modes (quantified by the intensities I_A and I_B) has increased.

Compared to the situation in the SSH laser array in figure 4.6, the modification of the gain imbalance examined in figure 4.8 now affects a much larger range of parameters, reaching up to $\gamma_{AB} \lesssim 2g_B$. This can be attributed not only to the larger number of competing states, but also to the larger propensity of the zero mode to hybridise with such states in the central region, which on its own would constitute a topologically trivial system. In this regime a very large number of additional solutions are encountered, which are all close to instability and therefore very sensitive to parameter changes, as demonstrated by the Bogoliubov-Floquet spectrum of the state marked P. Furthermore, an additional twisted mode appears close to the phase boundary of the zero mode, and indeed drives its instability along parts of this boundary (see the properties of the modes along the cross section at $\gamma_{AB} = 0.2$). In the remaining range of parameters, the system operates in analogous ways as before, with topological modes that display a larger output power when compared to the SSH laser array with analogously reduced gain imbalance (figure 4.6).

4.3.4 Robustness of operation conditions

Typical bosonic systems are subject to fabrication imperfections and residual internal and external dynamics, which may or may not break the assumed symmetries. For the laser arrays discussed in this chapter, these deviations manifest themselves as linear static perturbations in the bare resonator frequencies $\omega_{s,n}$ and the couplings κ_n, κ'_n, and the symmetry-breaking nonlinearities quantified by the linewidth-enhancement factors α_s. I therefore consider the case of coupling disorder (with perturbations $\kappa_n = \bar{\kappa}(1 + Wr_n)$, $\kappa'_n = \bar{\kappa}'(1 + Wr'_n)$) and onsite disorder (with perturbations $\omega_{A,n} = \omega_{AB} + Wr_n$, $\omega_{B,n} = \omega_{AB} + Wr'_n$), where r_n, r'_n are independent random numbers uniformly distributed in $[-1/2, 1/2]$, and compare the effects with the case of a finite linewidth-enhancement factor $\alpha_A = \alpha_B$.

4.3.5 Coupling disorder

As a notable feature, the spectral and nonlinear dynamical symmetries of the considered laser arrays remain preserved if all perturbations are restricted to the couplings. This type of disorder does not affect the symmetry-protected spectral position of the defect mode in the linear model, and also preserves the classification of topological states in the nonlinear extension with saturable gain.

At disorder levels of $W = 0.1$ the coupling disorder has a practically negligible effect on the phase diagram of the laser array. Such levels should be easily attainable in many applications, as they are well within the requirements to engineer any band structure effects in the first place. Only at much larger strengths the fundamental effects of disorder become discernible.

Figure 4.9 demonstrates that stronger disorder can result in disorder-strength-dependent phase transitions that modify the operation regimes in parts of parameter space, with the details generally depending on the disorder realisation. Four different disorder realisations are realised in the figure, where the operational

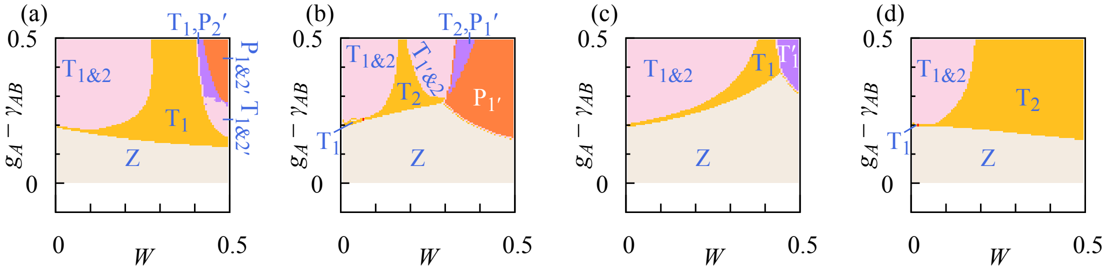

Figure 4.9: Disorder-driven phase transitions for the SSH laser array as in figures 4.2-4.4, but with fixed $\gamma_{AB} = 0.1$ and variable strength W of coupling disorder. Each panel corresponds to one randomly selected disorder configuration, with perturbed couplings $\kappa_n = \bar{\kappa}(1 + Wr_n)$, $\kappa_n' = \bar{\kappa}'(1 + Wr_n')$ obtained from a fixed realisations of uniformly distributed random numbers $r_n, r_n' \in [-1/2, 1/2]$. Zero-mode lasing persists at all disorder strengths. Twisted states remain robust for weak to moderate disorder, while phase transitions to other operating regimes can appear when the disorder is very strong.

regimes are plotted as a function of disorder strength. In each realisation the background losses have been fixed to $\gamma_{AB} = 0.1$. In all cases, new operation regimes emerge only for very strong disorder $W \gtrsim 0.3 - 0.5$, so that the parameter space remains dominated by the zero mode and the two twisted states.

For $W = 0.5$ a series of disorder realisations are illustrated in figure 4.11. At this level of disorder all of the states are visibly asymmetric. The phase space now looks drastically different, as the power-oscillating twisted state T_1 are pushed into regions that previously supported the stationary zero mode Z, which still dominates large parts of parameter space. Even though here this twisted state has a period similar to T_2 in the idealised case without disorder, it traces back to the state T_1 when the disorder strength is adiabatically reduced. The state labelled T_2', on the other hand, appears in a disorder-strength-dependent phase transition, and therefore cannot be traced back to any state in the clean system. Both twisted states become vulnerable to symmetry-breaking instabilities as one approaches conditions where the gain/loss ratio is large, $g_A \gg \gamma_{AB}$. In the given disorder realisation, the twisted mode T_1 undergoes a period-doubling bifurcation into a pair of symmetry-breaking modes P_1, which goes along with a noticeable increase of weight on the B sublattice. The second twisted mode T_2' also bifurcates into a pair of symmetry-breaking modes, but these turn out to be aperiodic.

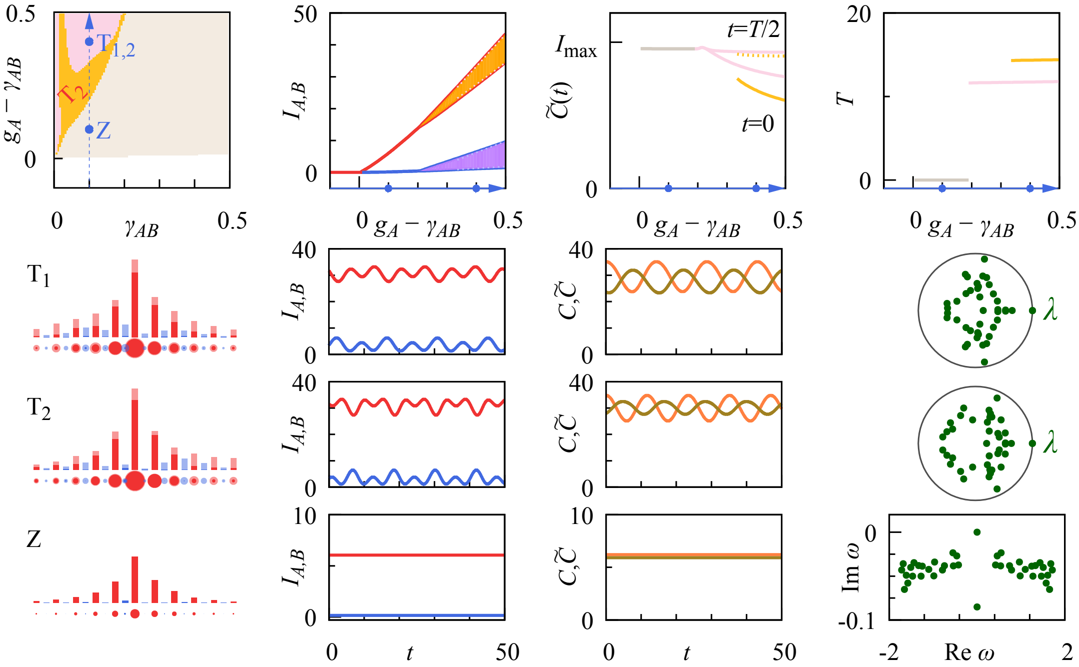

Figure 4.10: Effect of strong onsite disorder in analogy to figure 4.11, for the disorder realisation of figure 4.12(a) at $W = 0.5$. Even though the disorder breaks the symmetry, all states can be traced back to their disorder-free predecessors. The stationary lasing regime originating from the zero mode Z is barely affected. The mode originating from T_1 is pushed into a smaller part of parameter space, so that the instability phase transition now involves the modes originating from Z and T_2. The power-oscillations of the originally twisted states are modulated to clearly display the period T of underlying amplitude oscillations. The mode profiles of all states are only slightly distorted.

4.3.6 Onsite disorder

For onsite disorder, the strict classification of states by symmetry breaks down, and only the distinction between stationary states and power-oscillating states (as well as aperiodic and chaotic states) persists in a precise sense. Again for low levels of disorder such as $W = 0.1$ the effects of small to moderate levels of onsite disorder are again barely noticeable, just as in the case for coupling disorder. However, again for stronger disorder as shown in figure 4.12, the states can typically be traced back to their symmetry-respecting predecessors, where I retain the previous labelling. The disorder tends to expand the regime of stationary lasing originating from mode Z at the expense of the power-oscillating modes, while only occasionally leading to transitions into new operation regimes. Figure 4.10 illustrates this resilience against strong disorder for the disorder configuration of figure 4.12(a) with $W = 0.5$. For this disorder configuration the stationary lasing regime originating from mode Z is barely affected. Amongst the power oscillating states, the mode originating from T_1 is pushed into a smaller part of parameter space, so that the instability phase transition now involves the modes originating from Z and T_2. The main visible consequence of broken symmetry is a modulation of the power-oscillations, which now acquire the same period T as the complex-amplitude oscillations, while the two correlation functions C and $\tilde{C}$ exhibit different oscillation amplitudes. Notably, the spatial intensity profiles of the states are still only slightly modified, as they are affected more weakly than in the case of coupling disorder.

4.3.7 Symmetry-breaking nonlinearities

Similarly to the case of weak coupling and onsite disorder the lasing regimes are also highly resilient against realistic symmetry-breaking nonlinearities, giving rise to practically negligible effects for $\alpha_A = \alpha_B = 0.1$. Figure 4.13 shows that

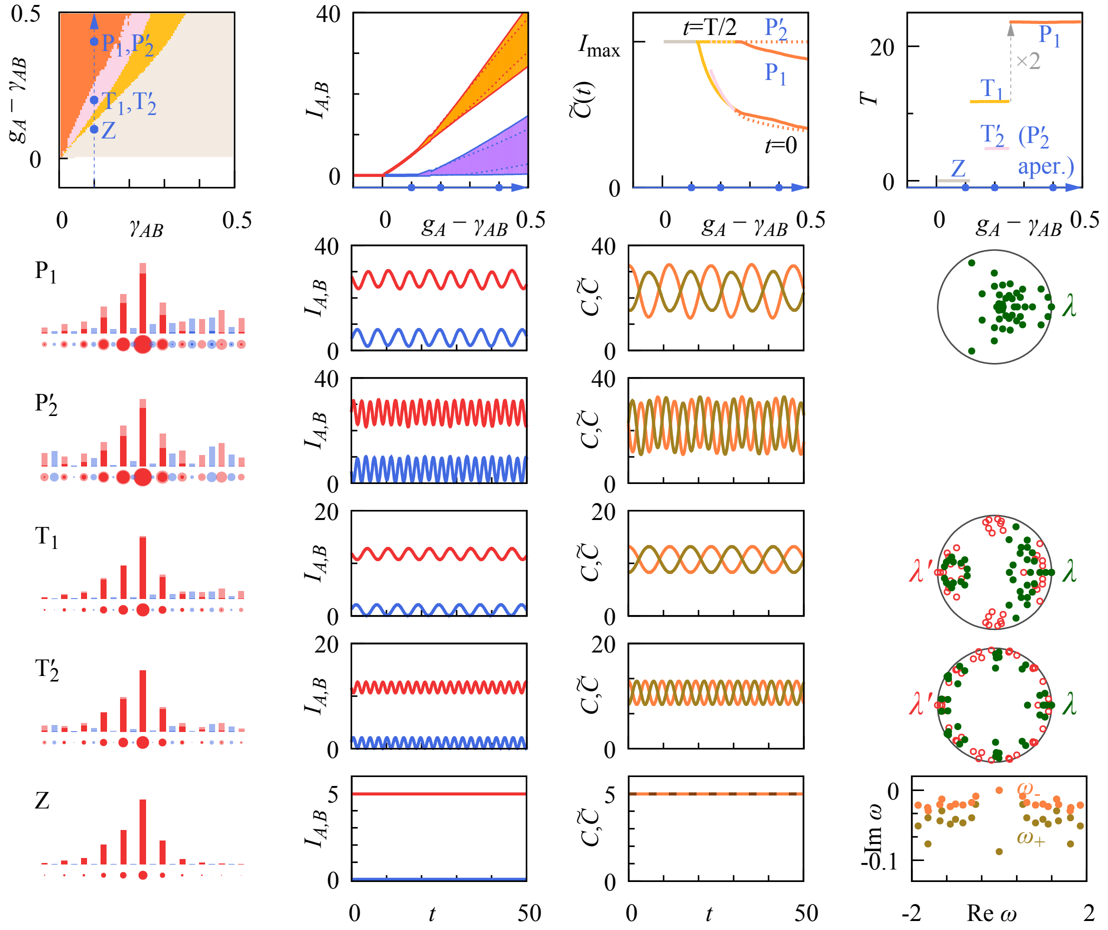

Figure 4.11: Effect of strong coupling disorder for the SSH laser array as in figures. 4.2-4.4, with the disorder configuration of figure 4.9(a) at $W = 0.5$. For this realisation the regime of zero-mode lasing is slightly reduced in favour of the power-oscillating twisted mode T_1, while the twisted state T_2 has been replaced by another twisted mode T'_2, which appears in a disorder-strength-dependent phase transition. As gain is further increased, T_1 undergoes a period-doubling bifurcation to a symmetry-breaking pair of states P_1, while T'_2 is replaced by an aperiodic pair P'_2 (for which the Floquet-Bogoliubov stability spectrum is not defined). All modes display visible distortions of their mode profile, and the symmetry-breaking pairs display noticeable amplitude on the B sublattice.

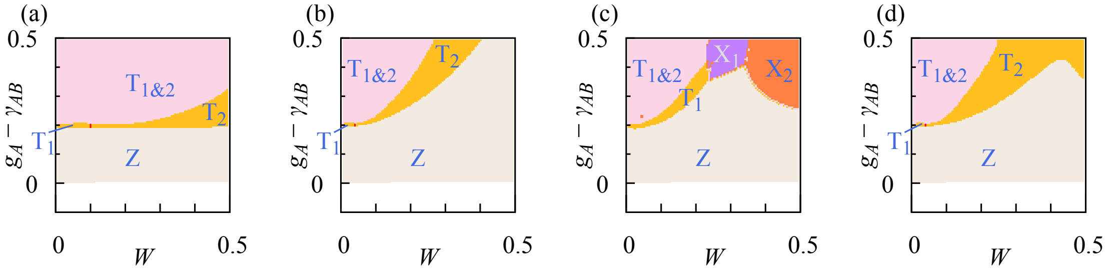

Figure 4.12: Robustness against onsite disorder in analogy to figure 4.9, but for randomly selected disorder configurations with perturbed bare frequencies $\omega_{A,n}=\omega_{AB}+Wr_n$, $\omega_{B,n}=\omega_{AB}+Wr'_n$, $r_n,r'_n\in[-1/2,1/2]$. While this type of disorder breaks the symmetries, the states can typically be tracked to large values of disorder. The mode originating from the zero mode Z persists at all disorder strengths, and at weak to moderate disorder extends into regions of larger gain. This happens at the expense of the originally twisted modes, which in panel the configuration of (c) are replaced by new power-oscillating modes X_1, X_2 when the disorder becomes strong.

even at much larger symmetry-breaking nonlinearities $\alpha_A=\alpha_B=0.5$ only small modifications are observed. The effects of the nonlinearities are still small enough to preserve the division into stationary and power-oscillating states, even though the broken symmetry once more prevents the precise topological characterisation of these states. The symmetry-breaking terms again modulate the power oscillations, which is displayed more clearly for the mode originating from T_2. The Bogoliubov spectra show that the states remain highly stable as long as one stays away from the clearly defined phase transitions.

The staggered arrangement $\alpha_A=-\alpha_B=0.2$ can also be considered. This breaks the non-hermitian charge-conjugation symmetry already in the linear regime. Figure 4.14 demonstrates that this robustness persists both for symmetry-breaking onsite disorder and nonlinearities can be attributed to the spectral isolation of the defect mode in the linear model. This isolation suppresses any matrix elements of hybridisation with extended modes in a perturbative treatment. It is also important to note that in the linear case, this spectral isolation is increased by the favourable gain imbalance, as seen from the position of the complex resonance frequencies in figure 4.1. Furthermore, disorder can turn the extended modes into localised ones, thereby decreasing their mode volume.

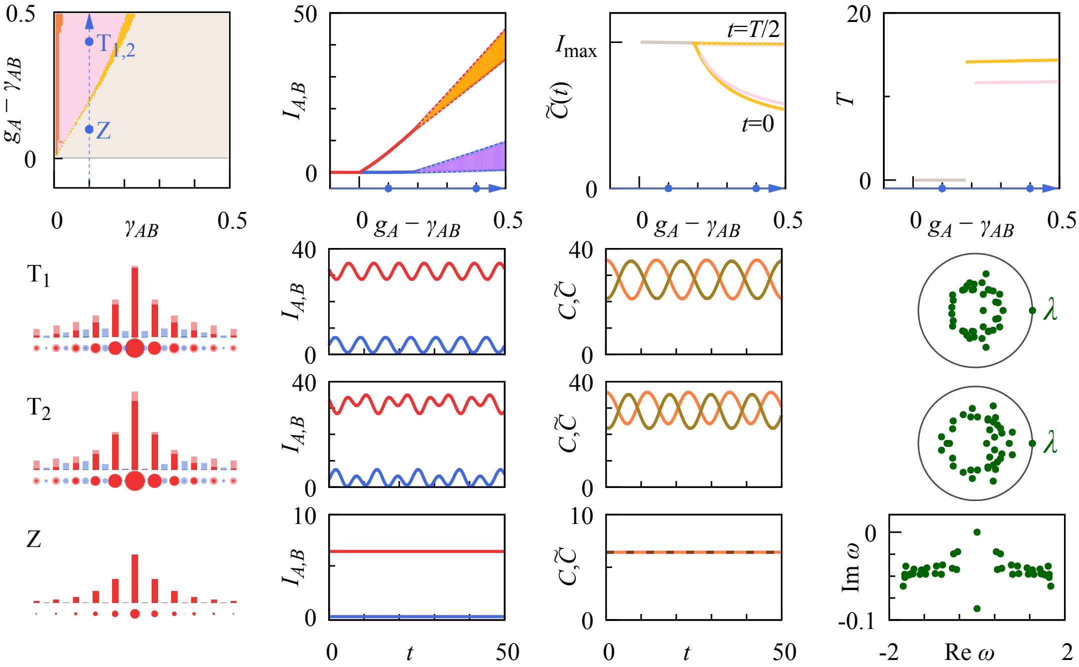

Figure 4.13: Effect of nonlinear symmetry breaking on the modes of the SSH laser array shown in figures 4.2-4.4, obtained by setting the linewidth-enhancement factor to $\alpha_A = \alpha_B = 0.5$. Most properties of the states are only slightly modified. The twisted correlation function $\tilde{C}(T/2)$ are slightly smaller than I_{max}, while small independent modulations appear in the time-dependence of $C(t)$, $\tilde{C}(t)$. For the state originating from T_2, this results in noticeable modulations of the power oscillations, whose period is doubled. There are also noticeable changes in the stability spectra (green), which can no longer be deconstructed as in the case of exact symmetry.

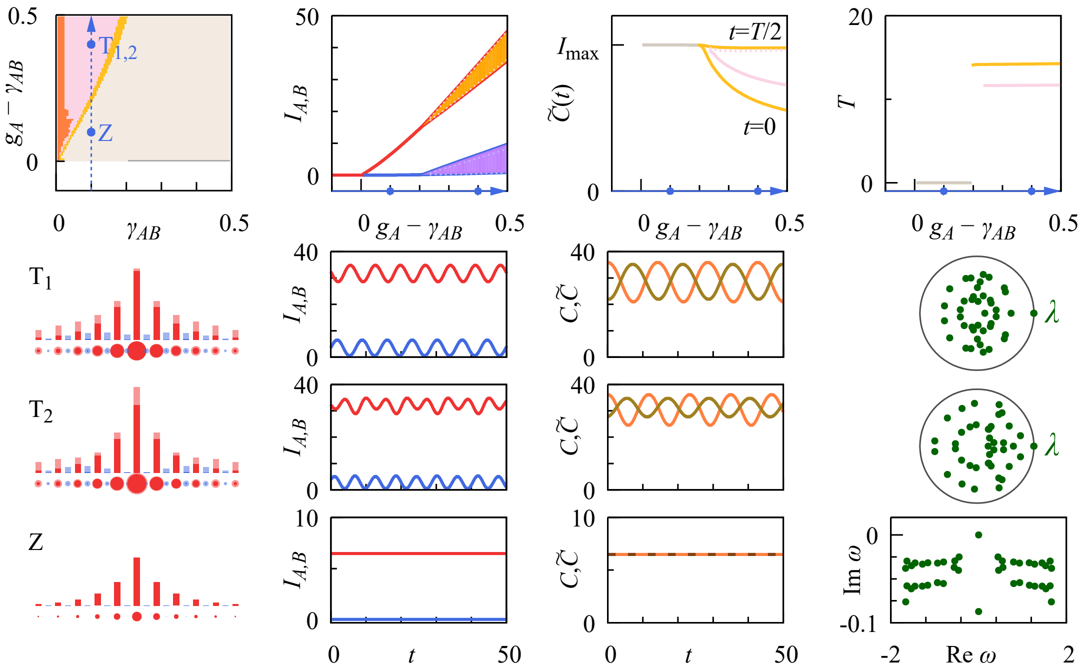

Figure 4.14: Effect of staggered nonlinear symmetry breaking on the modes of the SSH laser array shown in figures 4.2-4.4, obtained by setting the linewidth-enhancement factor to $\alpha_A = -\alpha_B = 0.2$ so that the non-hermitian charge-conjugation symmetry is already broken in the linear regime. As in figure 4.13, most properties of the states are only slightly modified.

4.4 Conclusions

The pursuit of topological effects in photonic systems is motivated by the desire to achieve robust features in analogy to fermionic systems, which in the bosonic setting requires a dedicated effort to evoke the required symmetries. The concept of a topological laser emerged from the realisation that anomalous expectation values facilitate the selection of topological states by linear gain and loss. This investigation of topological laser arrays shows that these concepts seamlessly extend to the nonlinear setting, which accounts for the effects that stabilise active systems in their quasi-stationary operation regimes.

I uncovered large ranges in parameter space that favour topological operation conditions, of which I encountered two types: stationary lasing in self-symmetric zero modes; and lasing in twisted states displaying symmetry-protected power oscillations. The topological nature of these states can be ascertained by their characteristic spatial mode structure, and on a deeper level by distinctive properties of their correlation functions and linear excitation spectra. These features also uncover topological phase transitions in which zero modes and twisted states interchange their stability. Encouragingly, the operation conditions can be tuned by changing the gain and loss distribution and the mode volume, while remaining remarkably robust under weak to moderate linear and nonlinear perturbations, even if these break the underlying symmetry.

These findings raise the prospect to explore the much simplified topological mode competition in a wide range of suitably patterned lasers with distributed gain and loss. The laser arrays considered here and in the experiments [25,26,46] realise the required dynamical version of non-hermitian charge-conjugation symmetry by providing two sublattices, a setting that directly extends to two and three-dimensional geometries, including polariton systems with flat bands [128, 131]. Alternatively, one may also exploit orbital and polarisation degrees of freedom in suitably coupled multi-mode cavities, or design photonic crystals with an equivalent coupled-mode representation to realise the required non-Hermitian charge-conjugation symmetry. By utilising additional components that induce an imaginary vector potential (hence, directionally biased coupling), the mode competition in chains as studied here can be modified towards favouring a single extended states [132], which further optimises the mode volume. All these systems promise to provide topological lasing modes with highly characteristic spatial and dynamical properties, which are stabilised at a working point that is spectrally well isolated from competing states in the system.

Looking beyond this symmetry class, it will be worthwhile to explore the role of nonlinear distributed gain and loss in topological-insulator lasers [41, 117], where topological edge states align continuously along an edge band. This is a scenario which has been predicted to be more fragile against the carrier dynamics in the medium [133], but is generally expected to benefit from non-hermitian effects, as has already been demonstrated for complex and directed couplings [134]. It would therefore be desirable to classify in general which nonlinearly extended dynamical symmetries can exist in these and other universality classes of topological systems, and whether this leads to novel operation regimes as described here for the case of non-hermitian charge-conjugation symmetry.

Chapter 5

Conclusions

In this thesis I have combined topological modes with non-Hermitian physics and explored the consequences in novel systems, prompting questions about whether the understanding of our current classifications for topological systems is complete, and providing examples of topological states which have no counterpart in the limit of the linear-Hermitian classification. I have probed this in several ways. Firstly in chapter 2 I exploited the open nature of optical systems to couple passively leaky resonators together. I showed that this passive leakage results in a non-Hermitian Hamiltonian with $\mathcal{PT}$-symmetry, obtained by deforming the geometry of the resonators such that backscattering of the resonant counter propagating whispering gallery modes is asymmetric. I then demonstrated that by adding an interface into a chain of these coupled resonators topological protected interface states can be created which vanish in the Hermitian limit. These topological states emerge from exceptional points in the continuum and become spectrally isolated, where they display long lifetimes. Furthermore, I identified the topological nature of these interface state in numerical simulations, where I subjected the backscattering amplitudes to increasing levels of disorder to show their robustness. This chapter raised the significant question of whether or not there is a way of reconciling this non-Hermitian topological state with the Hermitian classification in a setting which is easily accessible in experiments. It also poses the question of whether similar non-Hermitian topological states can be found in systems with which have no Hermitian analogue.

In chapter 3, I formulated an extension from a chain of coupled resonators into an array. I demonstrated that the modes in the bulk of such an array are capable of displaying bulk Fermi arcs between exceptional points if $\mathcal{PT}$-symmetry (broken through considering complex inter-resonator coupling and backscattering rates), where these bulk arcs do not feature in Weyl systems for example. In Weyl systems however, arcs projected from points in the bulk do appear on the surface of the structure which have an analogue to the edge-states that feature when an interface is placed in one direction splitting the array. I showed that these interface states vanish in the Hermitian-limit and exist for two different symmetry classes, the non-Hermitian extension of the class BDI with time-reversal and chiral symmetries and the class AIII where time-reversal symmetry is broken but chiral symmetry still remains. These interface states stretch between projected points of the bulk bands, where the bulk bands are fixed to real and imaginary energies. The complex frequency interface states which are physical then emerge from exceptional points connecting the real to imaginary bulk bands. I showed that the proportion of these states which are physical can be controlled by engineering anisotropy in the inter-resonator couplings and hence the patterned distance between resonators in the two directions. This work identifies two further non-Hermitian classes where topological states exist but are absent in the Hermitian limit. Complementary to chapter **??** this also showed that non-Hermitian topological states are not constrained to 1D systems but also appear in two dimensions.

Finally, In chapter 4, I discussed topological mode selection of topologically protected zero-modes in a non-linear laser model. The underlying model consists of a dimerised chain of alternating coupling strengths where a coupling defect separates out topological trivial and non-trivial phases. At this interface a topologically protected state forms. A complex alternating potential of gain and loss can selectively enhance this state. I considered a model in which this potential is non-linear, describing active optical systems which involve saturable gain-feedback processes. I demonstrated that beyond the linear regime stationary zero modes persists as well as finding a series of topologically protected time-dependant solutions. These time-dependant solutions display power oscillations and do not have a linear analogue. I showed the operational regimes of these topologically protected modes and perform a stability analysis to show that these states smoothly transition at Hopf bifurcations when the gain is increased. Furthermore I also considered increased mode competition by examining a system which has an extended interface, where a uniform coupling region is introduced. The results again show that despite the increased mode competition the topological states remain present.

In understanding the stability of these modes for both examples, the excitation spectra display surprisingly robust behaviour at weak levels of both coupling and onsite disorders. The analysis breaks down for some modes when strong disorders are used, but regions of the phase space are still occupied by the stationary modes, making them extremely robust. Finally I discussed the symmetry-breaking effects which appear for finite linewidth-enhancement factors, where again the topological modes remain surprisingly robust. This showcases a wide range of potential fabrication errors or effects which have little effect on the topologically protected modes. This model highlights the viability of topologically protected mode selection in non-linear lasers, where operational regimes have identified the stationary-solutions presented here. I hope for the future that the operational regimes where power-oscillations can be identified are achieved. This work also indicates that the topological classification can be extended to include non-linear symmetries, it would therefore be interesting to see if other symmetry classes display topologically protected non-linear modes which have no linear analogue.

Bibliography

[1] J. M. Dudley, “Editorial: Lighting up research,” *Phys. Rev. Lett.*, vol. 114, p. 120001, Mar 2015.

[2] S. John, “Strong localization of photons in certain disordered dielectric superlattices,” *Phys. Rev. Lett.*, vol. 58, pp. 2486–2489, Jun 1987.

[3] R. E. Slusher, L. W. Hollberg, B. Yurke, J. C. Mertz, and J. F. Valley, “Observation of squeezed states generated by four-wave mixing in an optical cavity,” *Phys. Rev. Lett.*, vol. 55, pp. 2409–2412, Nov 1985.

[4] D. F. Phillips, A. Fleischhauer, A. Mair, R. L. Walsworth, and M. D. Lukin, “Storage of light in atomic vapor,” *Phys. Rev. Lett.*, vol. 86, pp. 783–786, Jan 2001.

[5] W. E. Moerner and L. Kador, “Optical detection and spectroscopy of single molecules in a solid,” *Phys. Rev. Lett.*, vol. 62, pp. 2535–2538, May 1989.

[6] P. G. Kwiat, K. Mattle, H. Weinfurter, A. Zeilinger, A. V. Sergienko, and Y. Shih, “New high-intensity source of polarization-entangled photon pairs,” *Phys. Rev. Lett.*, vol. 75, pp. 4337–4341, Dec 1995.

[7] V. Kozii and L. Fu, “Non-Hermitian Topological Theory of Finite-Lifetime Quasiparticles: Prediction of Bulk Fermi Arc Due to Exceptional Point,” *ArXiv e-prints*, Aug. 2017.

[8] T. Yoshida, R. Peters, and N. Kawakami, "Non-hermitian perspective of the band structure in heavy-fermion systems," *Phys. Rev. B*, vol. 98, p. 035141, Jul 2018.

[9] S. Raghu and F. D. M. Haldane, "Analogs of quantum-hall-effect edge states in photonic crystals," *Phys. Rev. A*, vol. 78, p. 033834, Sep 2008.

[10] F. D. M. Haldane and S. Raghu, "Possible realization of directional optical waveguides in photonic crystals with broken time-reversal symmetry," *Phys. Rev. Lett.*, vol. 100, p. 013904, Jan 2008.

[11] Z. Wang, Y. Chong, J. D. Joannopoulos, and M. Soljačić, "Observation of unidirectional backscattering-immune topological electromagnetic states," *Nature*, vol. 461, pp. 772 EP –, 10 2009.

[12] T. Ochiai and M. Onoda, "Photonic analog of graphene model and its extension: Dirac cone, symmetry, and edge states," *Phys. Rev. B*, vol. 80, p. 155103, Oct 2009.

[13] K. Fang, Z. Yu, and S. Fan, "Microscopic theory of photonic one-way edge mode," *Phys. Rev. B*, vol. 84, p. 075477, Aug 2011.

[14] M. Hafezi, E. A. Demler, M. D. Lukin, and J. M. Taylor, "Robust optical delay lines with topological protection," *Nature Physics*, vol. 7, pp. 907 EP –, 08 2011.

[15] M. Hafezi, S. Mittal, J. Fan, A. Migdall, and J. M. Taylor, "Imaging topological edge states in silicon photonics," *Nature Photonics*, vol. 7, pp. 1001 EP –, 10 2013.

[16] K. Fang, Z. Yu, and S. Fan, "Realizing effective magnetic field for photons by controlling the phase of dynamic modulation," *Nature Photonics*, vol. 6, pp. 782 EP –, 10 2012.

[17] T. Kitagawa, E. Berg, M. Rudner, and E. Demler, "Topological characterization of periodically driven quantum systems," *Phys. Rev. B*, vol. 82, p. 235114, Dec 2010.

[18] M. C. Rechtsman, J. M. Zeuner, Y. Plotnik, Y. Lumer, D. Podolsky, F. Dreisow, S. Nolte, M. Segev, and A. Szameit, "Photonic floquet topological insulators," *Nature*, vol. 496, pp. 196 EP –, 04 2013.

[19] W. P. Su, J. R. Schrieffer, and A. J. Heeger, "Solitons in polyacetylene," *Phys. Rev. Lett.*, vol. 42, pp. 1698–1701, Jun 1979.

[20] M. S. Rudner and L. S. Levitov, "Topological transition in a non-hermitian quantum walk," *Phys. Rev. Lett.*, vol. 102, p. 065703, Feb 2009.

[21] M. S. Rudner, M. Levin, and L. S. Levitov, "Survival, decay, and topological protection in non-Hermitian quantum transport," *ArXiv e-prints*, May 2016.

[22] H. Schomerus, "Topologically protected midgap states in complex photonic lattices," *Opt. Lett.*, vol. 38, pp. 1912–1914, Jun 2013.

[23] C. Poli, M. Bellec, U. Kuhl, F. Mortessagne, and H. Schomerus, "Selective enhancement of topologically induced interface states in a dielectric resonator chain," *Nat. Commun.*, vol. 6, p. 6710, 04 2015.

[24] L. Ge, "Symmetry-protected zero-mode laser with a tunable spatial profile," *Phys. Rev. A*, vol. 95, p. 023812, Feb 2017.

[25] H. Zhao, P. Miao, M. H. Teimourpour, S. Malzard, R. El-Ganainy, H. Schomerus, and L. Feng, "Topological hybrid silicon microlasers," *Nat. Commun.*, vol. 9, p. 981, 2018.

[26] M. Parto, S. Wittek, H. Hodaei, G. Harari, M. A. Bandres, J. Ren, M. C. Rechtsman, M. Segev, D. N. Christodoulides, and M. Khajavikhan, "Edge-mode lasing in 1d topological active arrays," *Phys. Rev. Lett.*, vol. 120, p. 113901, Mar 2018.

[27] S. Weimann, M. Kremer, Y. Plotnik, Y. Lumer, S. Nolte, K. G. Makris, M. Segev, M. C. Rechtsman, and A. Szameit, "Topologically protected bound states in photonic parity–time-symmetric crystals," *Nat. Mater.*, vol. 16, p. 433, 12 2016.

[28] K. Esaki, M. Sato, K. Hasebe, and M. Kohmoto, "Edge states and topological phases in non-hermitian systems," *Phys. Rev. B*, vol. 84, p. 205128, Nov 2011.

[29] H. Zhao, S. Longhi, and L. Feng, "Robust light state by quantum phase transition in non-hermitian optical materials," *Scientific Reports*, vol. 5, p. 17022, Nov 2015.

[30] D. Leykam, K. Y. Bliokh, C. Huang, Y. D. Chong, and F. Nori, "Edge modes, degeneracies, and topological numbers in non-hermitian systems," *Phys. Rev. Lett.*, vol. 118, p. 040401, Jan 2017.

[31] S. Malzard, C. Poli, and H. Schomerus, "Topologically protected defect states in open photonic systems with non-hermitian charge-conjugation and parity-time symmetry," *Phys. Rev. Lett.*, vol. 115, p. 200402, Nov 2015.

[32] T. E. Lee, "Anomalous edge state in a non-hermitian lattice," *Phys. Rev. Lett.*, vol. 116, p. 133903, Apr 2016.

[33] S. Yao and Z. Wang, "Edge states and topological invariants of non-Hermitian systems," *ArXiv e-prints*, Mar. 2018.

[34] M. Pan, H. Zhao, P. Miao, S. Longhi, and L. Feng, "Photonic zero mode in a non-hermitian photonic lattice," *Nat. Commun.*, vol. 9, no. 1, p. 1308, 2018.

[35] X. Ni, D. Smirnova, A. Poddubny, D. Leykam, Y. Chong, and A. B. Khanikaev, "Exceptional points in topological edge spectrum of PT symmetric domain walls," *ArXiv e-prints*, 2018.

[36] H. Shen, B. Zhen, and L. Fu, “Topological band theory for non-hermitian hamiltonians,” *ArXiv e-prints*, 2017.

[37] Z. Gong, Y. Ashida, K. Kawabata, K. Takasan, S. Higashikawa, and M. Ueda, “Topological phases of non-Hermitian systems,” *ArXiv e-prints*, Feb. 2018.

[38] S. Knitter, S. F. Liew, W. Xiong, M. I. Guy, G. S. Solomon, and H. Cao, “Topological defect lasers,” *Journal of Optics*, vol. 18, no. 1, p. 014005, 2016.

[39] L. Pilozzi and C. Conti, “Topological lasing in resonant photonic structures,” *Phys. Rev. B*, vol. 93, p. 195317, May 2016.

[40] B. Bahari, A. Ndao, F. Vallini, A. El Amili, Y. Fainman, and B. Kanté, “Nonreciprocal lasing in topological cavities of arbitrary geometries,” *Science*, vol. 358, no. 6363, pp. 636–640, 2017.

[41] M. A. Bandres, S. Wittek, G. Harari, M. Parto, J. Ren, M. Segev, D. N. Christodoulides, and M. Khajavikhan, “Topological insulator laser: Experiments,” *Science*, 2018.

[42] H. Schomerus, “Quantum noise and self-sustained radiation of $\mathcal{PT}$-symmetric systems,” *Phys. Rev. Lett.*, vol. 104, p. 233601, Jun 2010.

[43] Y. D. Chong, L. Ge, and A. D. Stone, “$\mathcal{PT}$-symmetry breaking and laser-absorber modes in optical scattering systems,” *Phys. Rev. Lett.*, vol. 106, p. 093902, Mar 2011.

[44] H. Hodaei, M.-A. Miri, M. Heinrich, D. N. Christodoulides, and M. Khajavikhan, “Parity-time–symmetric microring lasers,” *Science*, vol. 346, no. 6212, pp. 975–978, 2014.

[45] L. Ge and R. El-Ganainy, “Nonlinear modal interactions in parity-time (pt) symmetric lasers,” *Scientific Reports*, vol. 6, pp. 24889 EP –, 05 2016.

[46] P. St-Jean, V. Goblot, E. Galopin, A. Lemaître, T. Ozawa, L. Le Gratiet, I. Sagnes, J. Bloch, and A. Amo, "Lasing in topological edge states of a one-dimensional lattice," *Nature Photonics*, vol. 11, no. 10, pp. 651–656, 2017.

[47] D. P. DiVincenzo, "The physical implementation of quantum computation," *Fortschritte der Physik*, vol. 48, no. 911, pp. 771–783.

[48] K. v. Klitzing, G. Dorda, and M. Pepper, "New method for high-accuracy determination of the fine-structure constant based on quantized hall resistance," *Phys. Rev. Lett.*, vol. 45, pp. 494–497, Aug 1980.

[49] A. Altland and M. R. Zirnbauer, "Nonstandard symmetry classes in mesoscopic normal-superconducting hybrid structures," *Phys. Rev. B*, vol. 55, pp. 1142–1161, Jan 1997.

[50] A. Kitaev, "Periodic table for topological insulators and superconductors," *AIP Conference Proceedings*, vol. 1134, no. 1, pp. 22–30, 2009.

[51] A. P. Schnyder, S. Ryu, A. Furusaki, and A. W. W. Ludwig, "Classification of topological insulators and superconductors in three spatial dimensions," *Phys. Rev. B*, vol. 78, p. 195125, Nov 2008.

[52] C. Reeg, C. Schrade, J. Klinovaja, and D. Loss, "Diii topological superconductivity with emergent time-reversal symmetry," *Phys. Rev. B*, vol. 96, p. 161407, Oct 2017.

[53] W. Shockley, "On the surface states associated with a periodic potential," *Phys. Rev.*, vol. 56, pp. 317–323, Aug 1939.

[54] M. Wimmer, A. R. Akhmerov, M. V. Medvedyeva, J. Tworzydło, and C. W. J. Beenakker, "Majorana bound states without vortices in topological superconductors with electrostatic defects," *Phys. Rev. Lett.*, vol. 105, p. 046803, Jul 2010.

[55] C. Beenakker, “Search for majorana fermions in superconductors,” *Annual Review of Condensed Matter Physics*, vol. 4, no. 1, pp. 113–136, 2013.

[56] H. Schomerus, “Random matrix approaches to open quantum systems,” *ArXiv e-prints*, Oct. 2016.

[57] B. Sutherland, “Localization of electronic wave functions due to local topology,” *Phys. Rev. B*, vol. 34, pp. 5208–5211, Oct 1986.

[58] S. Ryu and Y. Hatsugai, “Topological origin of zero-energy edge states in particle-hole symmetric systems,” *Phys. Rev. Lett.*, vol. 89, p. 077002, Jul 2002.

[59] C. M. Bender and S. Boettcher, “Real spectra in non-hermitian hamiltonians having $\mathcal{PT}$ symmetry,” *Phys. Rev. Lett.*, vol. 80, pp. 5243–5246, Jun 1998.

[60] C. M. Bender, S. Boettcher, and P. N. Meisinger, “Pt-symmetric quantum mechanics,” *Journal of Mathematical Physics*, vol. 40, no. 5, pp. 2201–2229, 1999.

[61] C. M. Bender, “Making sense of non-hermitian hamiltonians,” *Reports on Progress in Physics*, vol. 70, no. 6, p. 947, 2007.

[62] C. M. Bender, “Introduction to pt-symmetric quantum theory,” *Contemporary Physics*, vol. 46, no. 4, pp. 277–292, 2005.

[63] W. D. Heiss, “The physics of exceptional points,” *Journal of Physics A: Mathematical and Theoretical*, vol. 45, no. 44, p. 444016, 2012.

[64] K. Petermann, “Calculated spontaneous emission factor for double-heterostructure injection lasers with gain-induced waveguiding,” *IEEE Journal of Quantum Electronics*, vol. 15, pp. 566–570, July 1979.

[65] S.-Y. Lee, J.-W. Ryu, J.-B. Shim, S.-B. Lee, S. W. Kim, and K. An, “Divergent petermann factor of interacting resonances in a stadium-shaped microcavity,” *Phys. Rev. A*, vol. 78, p. 015805, Jul 2008.

[66] "Quantal phase factors accompanying adiabatic changes," *Proceedings of the Royal Society of London A: Mathematical, Physical and Engineering Sciences*, vol. 392, no. 1802, pp. 45–57, 1984.

[67] Heiss, W. D. and Harney, H. L., "The chirality of exceptional points," *Eur. Phys. J. D*, vol. 17, no. 2, pp. 149–151, 2001.

[68] C. Dembowski, B. Dietz, H.-D. Gräf, H. L. Harney, A. Heine, W. D. Heiss, and A. Richter, "Encircling an exceptional point," *Phys. Rev. E*, vol. 69, p. 056216, May 2004.

[69] J. Doppler, A. A. Mailybaev, J. Böhm, U. Kuhl, A. Girschik, F. Libisch, T. J. Milburn, P. Rabl, N. Moiseyev, and S. Rotter, "Dynamically encircling an exceptional point for asymmetric mode switching," *Nature*, vol. 537, pp. 76 EP –, 07 2016.

[70] T. J. Milburn, J. Doppler, C. A. Holmes, S. Portolan, S. Rotter, and P. Rabl, "General description of quasiadiabatic dynamical phenomena near exceptional points," *Phys. Rev. A*, vol. 92, p. 052124, Nov 2015.

[71] D. Heiss, "Circling exceptional points," *Nature Physics*, vol. 12, pp. 823 EP –, 08 2016.

[72] E.-M. Graefe, A. A. Mailybaev, and N. Moiseyev, "Breakdown of adiabatic transfer of light in waveguides in the presence of absorption," *Phys. Rev. A*, vol. 88, p. 033842, Sep 2013.

[73] I. Gilary, A. A. Mailybaev, and N. Moiseyev, "Time-asymmetric quantum-state-exchange mechanism," *Phys. Rev. A*, vol. 88, p. 010102, Jul 2013.

[74] H. Cao and J. Wiersig, "Dielectric microcavities: Model systems for wave chaos and non-hermitian physics," *Rev. Mod. Phys.*, vol. 87, pp. 61–111, Jan 2015.

[75] K. J. Vahala, “Optical microcavities,” *Nature*, vol. 424, pp. 839 EP –, 08 2003.

[76] M. Pelton, C. Santori, J. Vucˇković, B. Zhang, G. S. Solomon, J. Plant, and Y. Yamamoto, “Efficient source of single photons: A single quantum dot in a micropost microcavity,” *Phys. Rev. Lett.*, vol. 89, p. 233602, Nov 2002.

[77] J. Su, “Label-free biological and chemical sensing using whispering gallery mode optical resonators: Past, present, and future,” *Sensors*, vol. 17, no. 3, 2017.

[78] M.-Y. Ye, M.-X. Shen, and X.-M. Lin, “Ringing phenomenon based whispering-gallery-mode sensing,” *Scientific Reports*, vol. 6, pp. 19597 EP –, 01 2016.

[79] X.-F. Jiang, Y.-F. Xiao, C.-L. Zou, L. He, C.-H. Dong, B.-B. Li, Y. Li, F.-W. Sun, L. Yang, and Q. Gong, “Highly unidirectional emission and ultralow-threshold lasing from on-chip ultrahigh-q microcavities,” *Advanced Materials*, vol. 24, no. 35, pp. OP260–OP264.

[80] J. Zhu, S. K. Ozdemir, Y.-F. Xiao, L. Li, L. He, D.-R. Chen, and L. Yang, “On-chip single nanoparticle detection and sizing by mode splitting in an ultrahigh-q microresonator,” *Nature Photonics*, vol. 4, pp. 46 EP –, 12 2009.

[81] A. F. J. Levi, R. E. Slusher, S. L. McCall, J. L. Glass, S. J. Pearton, and R. A. Logan, “Directional light coupling from microdisk lasers,” *Applied Physics Letters*, vol. 62, no. 6, pp. 561–563, 1993.

[82] D. V. Strekalov, C. Marquardt, A. B. Matsko, H. G. L. Schwefel, and G. Leuchs, “Nonlinear and quantum optics with whispering gallery resonators,” *Journal of Optics*, vol. 18, no. 12, p. 123002, 2016.

[83] J. Wiersig, “Chiral and nonorthogonal eigenstate pairs in open quantum systems with weak backscattering between counterpropagating traveling waves,” *Phys. Rev. A*, vol. 89, p. 012119, Jan 2014.

[84] J. Wiersig, A. Eberspächer, J.-B. Shim, J.-W. Ryu, S. Shinohara, M. Hentschel, and H. Schomerus, "Nonorthogonal pairs of copropagating optical modes in deformed microdisk cavities," *Phys. Rev. A*, vol. 84, p. 023845, Aug 2011.

[85] G. Q. Liang and Y. D. Chong, "Optical resonator analog of a two-dimensional topological insulator," *Phys. Rev. Lett.*, vol. 110, p. 203904, May 2013.

[86] H. Schomerus and J. Wiersig, "Non-hermitian-transport effects in coupled-resonator optical waveguides," *Phys. Rev. A*, vol. 90, p. 053819, Nov 2014.

[87] M. V. Berry, "Physics of nonhermitian degeneracies," *Czechoslovak Journal of Physics*, vol. 54, no. 10, pp. 1039–1047, 2004.

[88] J. Wiersig, "Enhancing the sensitivity of frequency and energy splitting detection by using exceptional points: Application to microcavity sensors for single-particle detection," *Phys. Rev. Lett.*, vol. 112, p. 203901, May 2014.

[89] H. Schomerus, K. Frahm, M. Patra, and C. Beenakker, "Quantum limit of the laser line width in chaotic cavities and statistics of residues of scattering matrix poles," *Physica A: Statistical Mechanics and its Applications*, vol. 278, no. 3, pp. 469 – 496, 2000.

[90] H. Schomerus, "Excess quantum noise due to mode nonorthogonality in dielectric microresonators," *Phys. Rev. A*, vol. 79, p. 061801, Jun 2009.

[91] M. Z. Hasan and C. L. Kane, "Colloquium: Topological insulators," *Rev. Mod. Phys.*, vol. 82, pp. 3045–3067, Nov 2010.

[92] Y. Xiong, "Why does bulk boundary correspondence fail in some non-hermitian topological models," *Journal of Physics Communications*, vol. 2, no. 3, p. 035043, 2018.

[93] C. Dembowski, B. Dietz, H.-D. Gräf, H. L. Harney, A. Heine, W. D. Heiss, and A. Richter, "Observation of a chiral state in a microwave cavity," *Phys. Rev. Lett.*, vol. 90, p. 034101, Jan 2003.

[94] B. Peng, Ş. K. Özdemir, M. Liertzer, W. Chen, J. Kramer, H. Yılmaz, J. Wiersig, S. Rotter, and L. Yang, "Chiral modes and directional lasing at exceptional points," *Proceedings of the National Academy of Sciences*, vol. 113, no. 25, pp. 6845–6850, 2016.

[95] L.-J. Lang, Y. Wang, H. Wang, and Y. D. Chong, "Effects of Non-Hermiticity on Su-Schrieffer-Heeger Defect States," *ArXiv e-prints*, July 2018.

[96] H. Nielsen and M. Ninomiya, "The Adler-Bell-Jackiw anomaly and Weyl fermions in a crystal," *Phys. Lett. B*, vol. 130, no. 6, pp. 389 – 396, 1983.

[97] A. A. Burkov and L. Balents, "Weyl semimetal in a topological insulator multilayer," *Phys. Rev. Lett.*, vol. 107, p. 127205, Sep 2011.

[98] B. Yan and C. Felser, "Topological materials: Weyl semimetals," *Annual Review of Condensed Matter Physics*, vol. 8, no. 1, pp. 337–354, 2017.

[99] X. Wan, A. M. Turner, A. Vishwanath, and S. Y. Savrasov, "Topological semimetal and fermi-arc surface states in the electronic structure of pyrochlore iridates," *Phys. Rev. B*, vol. 83, p. 205101, May 2011.

[100] S.-Y. Xu, I. Belopolski, N. Alidoust, M. Neupane, G. Bian, C. Zhang, R. Sankar, G. Chang, Z. Yuan, C.-C. Lee, S.-M. Huang, H. Zheng, J. Ma, D. S. Sanchez, B. Wang, A. Bansil, F. Chou, P. P. Shibayev, H. Lin, S. Jia, and M. Z. Hasan, "Discovery of a weyl fermion semimetal and topological fermi arcs," *Science*, vol. 349, no. 6248, pp. 613–617, 2015.

[101] B. Yang, Q. Guo, B. Tremain, L. E. Barr, W. Gao, H. Liu, B. Béri, Y. Xiang, D. Fan, A. P. Hibbins, and S. Zhang, "Direct observation of topological

surface-state arcs in photonic metamaterials," *Nat. Commun.*, vol. 8, no. 1, p. 97, 2017.

[102] J. Noh, S. Huang, D. Leykam, Y. D. Chong, K. P. Chen, and M. C. Rechtsman, "Experimental observation of optical Weyl points and Fermi arc-like surface states," *Nat. Phys.*, vol. 13, p. 611, 03 2017.

[103] M. Xiao, W.-J. Chen, W.-Y. He, and C. T. Chan, "Synthetic gauge flux and weyl points in acoustic systems," *Nature Physics*, vol. 11, pp. 920 EP –, 09 2015.

[104] Z. Yang and B. Zhang, "Acoustic type-ii weyl nodes from stacking dimerized chains," *Phys. Rev. Lett.*, vol. 117, p. 224301, Nov 2016.

[105] A. Cerjan, M. Xiao, L. Yuan, and S. Fan, "Effects of non-hermitian perturbations on weyl hamiltonians with arbitrary topological charges," *Phys. Rev. B*, vol. 97, p. 075128, Feb 2018.

[106] H. Zhou, C. Peng, Y. Yoon, C. W. Hsu, K. A. Nelson, L. Fu, J. D. Joannopoulos, M. Soljačić, and B. Zhen, "Observation of bulk fermi arc and polarization half charge from paired exceptional points," *Science*, 2018.

[107] A. Szameit, M. C. Rechtsman, O. Bahat-Treidel, and M. Segev, "$\mathcal{PT}$-symmetry in honeycomb photonic lattices," *Phys. Rev. A*, vol. 84, p. 021806, Aug 2011.

[108] H. Ramezani, T. Kottos, V. Kovanis, and D. N. Christodoulides, "Exceptional-point dynamics in photonic honeycomb lattices with $\mathcal{PT}$ symmetry," *Phys. Rev. A*, vol. 85, p. 013818, Jan 2012.

[109] M. Golshani, S. Weimann, K. Jafari, M. K. Nezhad, A. Langari, A. R. Bahrampour, T. Eichelkraut, S. M. Mahdavi, and A. Szameit, "Impact of loss on the wave dynamics in photonic waveguide lattices," *Phys. Rev. Lett.*, vol. 113, p. 123903, Sep 2014.

[110] H. Schomerus and J. Wiersig, "Non-hermitian-transport effects in coupled-resonator optical waveguides," *Phys. Rev. A*, vol. 90, p. 053819, Nov 2014.

[111] H. Zhao and L. Feng, "Parity–time symmetric photonics," *National Science Review*, vol. 5, pp. 183–199, 03 2018.

[112] N. Goldman, J. C. Budich, and P. Zoller, "Topological quantum matter with ultracold gases in optical lattices," *Nature Physics*, vol. 12, pp. 639 EP –, 06 2016.

[113] V. G. Sala, D. D. Solnyshkov, I. Carusotto, T. Jacqmin, A. Lemaître, H. Terças, A. Nalitov, M. Abbarchi, E. Galopin, I. Sagnes, J. Bloch, G. Malpuech, and A. Amo, "Spin-orbit coupling for photons and polaritons in microstructures," *Phys. Rev. X*, vol. 5, p. 011034, Mar 2015.

[114] T. Karzig, C.-E. Bardyn, N. H. Lindner, and G. Refael, "Topological polaritons," *Phys. Rev. X*, vol. 5, p. 031001, Jul 2015.

[115] A. V. Nalitov, D. D. Solnyshkov, and G. Malpuech, "Polariton $\mathbb{Z}$ topological insulator," *Phys. Rev. Lett.*, vol. 114, p. 116401, Mar 2015.

[116] Z. Yang, F. Gao, X. Shi, X. Lin, Z. Gao, Y. Chong, and B. Zhang, "Topological acoustics," *Phys. Rev. Lett.*, vol. 114, p. 114301, Mar 2015.

[117] G. Harari, M. A. Bandres, Y. Lumer, M. C. Rechtsman, Y. D. Chong, M. Khajavikhan, D. N. Christodoulides, and M. Segev, "Topological insulator laser: Theory," *Science*, 2018.

[118] C. E. Whittaker, E. Cancellieri, P. M. Walker, D. R. Gulevich, H. Schomerus, D. Vaitiekus, B. Royall, D. M. Whittaker, E. Clarke, I. V. Iorsh, I. A. Shelykh, M. S. Skolnick, and D. N. Krizhanovskii, "Exciton polaritons in a two-dimensional lieb lattice with spin-orbit coupling," *Phys. Rev. Lett.*, vol. 120, p. 097401, Mar 2018.

[119] R. Yao, H. Li, B. Zheng, S. An, J. Ding, C.-S. Lee, H. Zhang, and W. Guo, "Electrically Tunable and Reconfigurable Topological Edge State Lasers," *ArXiv e-prints*, Apr. 2018.

[120] S. Furukawa and M. Ueda, "Excitation band topology and edge matter waves in boseeinstein condensates in optical lattices," *New Journal of Physics*, vol. 17, no. 11, p. 115014, 2015.

[121] C.-E. Bardyn, T. Karzig, G. Refael, and T. C. H. Liew, "Chiral bogoliubov excitations in nonlinear bosonic systems," *Phys. Rev. B*, vol. 93, p. 020502, Jan 2016.

[122] R. Barnett, "Edge-state instabilities of bosons in a topological band," *Phys. Rev. A*, vol. 88, p. 063631, Dec 2013.

[123] G. Engelhardt, M. Benito, G. Platero, and T. Brandes, "Topological instabilities in ac-driven bosonic systems," *Phys. Rev. Lett.*, vol. 117, p. 045302, Jul 2016.

[124] T. Harayama, S. Sunada, and K. S. Ikeda, "Theory of two-dimensional microcavity lasers," *Phys. Rev. A*, vol. 72, p. 013803, Jul 2005.

[125] D. I. Pikulin and Y. V. Nazarov, "Topological properties of superconducting junctions," *JETP Letters*, vol. 94, pp. 693–697, Jan 2012.

[126] D. I. Pikulin and Y. V. Nazarov, "Two types of topological transitions in finite majorana wires," *Phys. Rev. B*, vol. 87, p. 235421, Jun 2013.

[127] P. San-Jose, J. Cayao, E. Prada, and R. Aguado, "Majorana bound states from exceptional points in non-topological superconductors," *Scientific Reports*, vol. 6, pp. 21427 EP –, Feb 2016. Article.

[128] S. Malzard, E. Cancellieri, and H. Schomerus, "Topological dynamics and excitations in lasers and condensates with saturable gain or loss," *Opt. Express*, vol. 26, pp. 22506–22518, Aug 2018.

[129] M. Tlidi, P. Mandel, and M. Haelterman, "Spatiotemporal patterns and localized structures in nonlinear optics," *Phys. Rev. E*, vol. 56, pp. 6524–6530, Dec 1997.

[130] G. Wen, D. Xu, and X. Han, "On creation of hopf bifurcations in discrete-time nonlinear systems," *Chaos: An Interdisciplinary Journal of Nonlinear Science*, vol. 12, no. 2, pp. 350–355, 2002.

[131] H. Schomerus and N. Y. Halpern, "Parity anomaly and landau-level lasing in strained photonic honeycomb lattices," *Phys. Rev. Lett.*, vol. 110, p. 013903, Jan 2013.

[132] S. Longhi, "Non-hermitian gauged topological laser arrays," *Annalen der Physik*, vol. 530, no. 7, p. 1800023, 2018.

[133] S. Longhi, Y. Kominis, and V. Kovanis, "Presence of temporal dynamical instabilities in topological insulator lasers," *EPL (Europhysics Letters)*, vol. 122, no. 1, p. 14004, 2018.

[134] S. Longhi and L. Feng, "Invited article: Mitigation of dynamical instabilities in laser arrays via non-hermitian coupling," *APL Photonics*, vol. 3, no. 6, p. 060802, 2018.